Pro gradu -tutkielma
(geofysiikka)

Convection in the Greenland Sea – Model and Observations –

Aleksi Nummelin
2012

Ohjaaja: Bert Rudels
Tarkastajat: Bert Rudels
Jari Haapala

HELSINGIN YLIOPISTO
FYSIIKAN LAITOS

PL 64 (Gustaf Hällströmin katu 2)
00014 Helsingin yliopisto

HELSINGIN YLIOPISTO — HELSINGFORS UNIVERSITET — UNIVERSITY OF HELSINKI

Tiedekunta/Osasto — Fakultet/Sektion — Faculty	Laitos — Institution — Department
Faculty of Science	Department of Physics

Tekijä — Författare — Author
Aleksi Nummelin

Työn nimi — Arbetets titel — Title

Convection in the Greenland Sea: Model and Observations

Oppiaine — Läroämne — Subject		
Geophysics		
Työn laji — Arbetets art — Level	Aika — Datum — Month and year	Sivumäärä — Sidoantal — Number of pages
Master's thesis	April 2012	83 pp.

Tiivistelmä — Referat — Abstract

The Meridional overturning circulation (MOC) is one crucial component in Earth's climate system, redistributing heat round the globe. The abyssal limb of the MOC is fed by the deep water formation near the poles. A basic requirement for any successful climate model simulation is the ability to reproduce this circulation correctly. The deep water formation itself, convection, occurs on smaller scales than the climate model grid size. Therefore the convection process needs to be parameterized. It is, however, somewhat unclear how well the parameterizations which are developed for turbulence can reproduce the deep convection and associated water mass transformations.

The convection in the Greenland Sea was studied with 1-D turbulence model GOTM and with data from three Argo floats. The model was run over the winter 2010-2011 with ERA-Interim and NCEP/NCAR atmospheric forcings and with three different mixing parameterizations, $k-\epsilon$, $k-k$L (Mellor-Yamada) and KPP. Furthermore, the effects of mesoscale spatial variations in the atmospheric forcing data were tested by running the model with forcings taken along the floats' paths (Lagrangian approach) and from the floats' median locations (Eulerian approach).

The convection was found to happen by gradual mixed layer deepening. It caused salinity decrease in the Recirculating Atlantic Water (RAW) layer just below the surface while in the deeper layers salinity and density increase was clearly visible. A slight temperature decrease was observed in whole water column above the convection depth. Atmospheric forcing had the strongest effect on the model results. ERA-interim forcing produced model output closer to the observations, but the convection begun too early with both forcings and both generated too low temperatures in the end. The salinity increase at mid-depths was controlled mainly by the RAW layer, but also atmospheric freshwater flux was found to affect the end result. Furthermore, NCEP/NCAR freshwater flux was found to be large enough (negative) to become a clear secondary driving factor for the convection. The results show that mixing parameterization mainly alters the timing of convection. KPP parameterization produced clearly too fast convection while $k-\epsilon$ parameterization produced output which was closest to the observations. The results using Lagrangian and Eulerian approaches were ambiguous in the sense that neither of them was systematically closer to the observations. This could be explained by the errors in the reanalyzes arising from their grid size. More conclusive results could be produced with the aid of finer scale atmospheric data. The results, however, clearly indicate that atmospheric variability in scales of 100 km produces quantifiable differences in the results.

Avainsanat — Nyckelord — Keywords
Greenland Sea, convection, GOTM, 1-D turbulence model, $k-\epsilon$, $k-k$L, KPP, Argo float

Säilytyspaikka — Förvaringsställe — Where deposited

Muita tietoja — övriga uppgifter — Additional information

HELSINGIN YLIOPISTO — HELSINGFORS UNIVERSITET — UNIVERSITY OF HELSINKI

Tiedekunta/Osasto — Fakultet/Sektion — Faculty	Laitos — Institution — Department
Matemaattis-luonnontieteellinen	Fysiikan laitos

Tekijä — Författare — Author
Aleksi Nummelin

Työn nimi — Arbetets titel — Title

Convection in the Greenland Sea: model and observations

Oppiaine — Läroämne — Subject
Geofysiikka

Työn laji — Arbetets art — Level	Aika — Datum — Month and year	Sivumäärä — Sidoantal — Number of pages
Pro gradu -tutkielma	huhtikuu 2012	83 s.

Tiivistelmä — Referat — Abstract

Termohaliinikierto kierrättää lämpöä ympäri maapallon ja on yksi ilmastosysteemin tärkeimmistä komponenteista. Lähellä napoja tapahtuva syvän veden muodostus toimii termohallinkierron syvän komponentin pakotteena. Perusedellytys mille tahansa ilmastomallille on tämän kiertoliikkeen oikea mallintaminen. Syvän veden muodostuminen, konvektio, tapahtuu kuitenkin paljon ilmastomallien hilakokoa pienemmässä mittakaavassa ja siksi se tulee parametrisoida. Turbulenssin mallintamiseen kehitettyjen parametrisaatioiden toimivuus konvektiotilanteissa ei ole kuitenkaan itsestään selvää.

Grönlanninmeren konvektiota tutkittiin 1-D turbulenssimalli GOTM:n ja kolmesta Argo poijusta saatujen havaintojen avulla. Mallinnus on tehty talven 2010-2011 yli käyttäen kolmea eri turbulenssiparametrisaatiota, jotka olivat $k-\epsilon$, $k-k$L (Mellor-Yamada) ja KPP. Lisäksi ilmakehäpakotteina käytettyjen ERA-Interim ja NCEP/NCAR uusanalyysien alueellisten muutosten vaikutuksia tutkittiin ajamalla mallia pakotteilla jotka oli poimittu Argo poijujen reitiltä (Lagrangelainen lähestymistapa) sekä poijujen mediaanisijainnista (Eulerlainen lähestymistapa).

Konvektion havaittiin tapahtuvan sekoittumiskerroksen tasaisen syvenemisen kautta. Konvektio aiheutti suolaisuuden laskua Atlanttisen vesimassan kerroksessa pinnan lähellä. Syvemmällä havaittiin selvä suolaisuuden ja tiheyden kasvu. Koko vesipatsaassa havaittiin heikkoa lämpötilan laskua. Ilmakehäpakote vaikutti tuloksiin eniten. ERA-Interim pakotteen avulla saatiin lähimpänä havaintoja olevia tuloksia, mutta molempien pakotteiden tapauksessa konvektio alkoi selvästi liian aikaisin ja lämpötila laski selvästi liian paljon. Atlanttin vesimassa kontrolloi syvemmissä kerroksissa havaittua suolaisuuden kasvua, mutta myös ilmakehäpakotteella havaittiin olevan selvä vaikutus lopputulokseen. Etenkin NCEP/NCAR pakotteesta saadun makeanveden vuon havaittiin olevan niin suuri, että sillä oli selvä vaikutus konvektion etenemiseen. Saadut tulokset osoittavat, että turbulenssiparametrisaatio vaikuttaa lähinnä konvektion ajoitukseen. $k-\epsilon$ parametrisaation havaittiin tuottavan lähimpänä havaintoja olevia tuloksia kun taas KPP parametrisaatio tuotti selvästi liian nopean konvektion. Lagrangelaisella ja Eulerlaisella lähestymistavalla saadut tulokset olivat monitulkintaisia siinä mielessä, että kumpikaan lähestymistapa ei tuottanut systemaattisesti lähempänä havaintoja olevia tuloksia. Tämä voidaan selittää uusanalyysien hilakoosta johtuvista epätarkkuuksista, jotka ovat siis samaa suurusluokkaa Lagrangelaisesta ja Eulerlaisesta lähestymistavasta johtuvien erojen kanssa. Hienohilaisemman ilmakehäpakotteen avulla tulokset saattaisivat olla selkeämpiä, kun uusanalyysien epätarkkuudet pienenisivät. Tulokset osoittavat joka tapauksessa, että ilmakehässä 100 km skaalassa tapahtuvat muutokset aiheuttavat selkeitä eroja myös meressä.

Avainsanat — Nyckelord — Keywords
Greenland Sea, convection, 1-D model, GOTM, turbulence model, $k-\epsilon$, $k-k$L, KPP, Argo float

Säilytyspaikka — Förvaringsställe — Where deposited

Muita tietoja — övriga uppgifter — Additional information

Contents

Chapter 1

Introduction

Deep convection and associated dense water formation feeding the meridional overturning circulation is one of the crucial components in the Earth's climate system (Marshall and Schott, 1999). In areas where extensive buoyancy forcing (heat loss, evaporation and brine rejection) triggers convection events, surface water becomes denser than the abyssal water mass and sinks down to the depth of neutral buoyancy (Marshall and Schott, 1999). Dense water forms the abyssal limb of the oceanic heat transport carrying cold waters from higher to lower latitudes. Based on recent modelling study by Ferrari and Ferreira (2011) this lower part of the circulation accounts for 60 % of the total heat transport in the North-Atlantic and 40 % globally. It should be noted, however, that in the same study they also found that the heat transported by the deep circulation is as sensitive to wind stress as it is to high-latitude convection. Ferrari and Ferreira (2011) further noted that, unlike the number of past studies, the effect of weakening of the deep convection for ocean heat transport should not be considered unless the possible changes in winds (in both hemispheres) were also taken into account. Furthermore, it is known from paleoclimate records (Zachos et al., 2001; Hoffman et al., 1998) that the climate system is not stable on long time scales. In addition recent modelling studies with aqua-planet (Ferreira et al., 2010) and energy-balance model (Rose and Marshall, 2009) have revealed that three different equilibrium states; polar ice cap extending to midlatitudes, ice free state and fully ice covered 'snowball' state, can be supported and the changes between the equilibria can be abrupt. From previous studies it is known that the distribution of ocean heat transport convergence regulates the ice extent in the present climate (Bitz et al., 2005) and also Ferreira et al. (2010) concluded that the different equilibria are due

to differences in meridional structure of oceanic heat transport. A recent discussion about possible 'tipping events' which could change the eqilibrium state, including the shutdown of convection in North-Atlantic, can be found in Lenton et al. (2008).

Open Ocean deep convection is concentrated in four areas of the world oceans, Labrador, Greenland, Mediterranean and Weddell seas (Marshall and Schott, 1999). Although the areas where the convection takes place are relatively large, the convection itself is occurring in horizontal scales from few hundred meters to one kilometer (Marshall and Schott, 1999). This scale is still one order of magnitude smaller than the scale of the state-of-the-art ocean state prediction models, not to mention climate prediction models. This leads to the need for convection parameterizations, although recently Campin et al. (2011) discussed the possibility of super-parameterization in ocean modelling. With super-parameterization it is possible to embed high-resolution 2-D non-hydrostatic model in 3-D hydrostatic coarse resolution model and obtain results comparable to high-resolution non-hydrostatic 3-D runs, but with significantly reduced computational cost. Although Campin et al. (2011) used somewhat simplified setup this kind of an approach could lead to situation where parameterizations are no more needed sooner than full non-hydrostatic models become feasible to use in large scale.

Several parameterization of ocean mixing, from simple convective adjustment to second order turbulence models, have been introduced trough the years (Burchard, 2002). However, most of the present day parameterizations are based on turbulence theory, which is not developed for convection (Burchard, 2002; Marshall and Schott, 1999). The most critical limitations are that most of the parameterizations assume the turbulent fluxes to be proportional to the gradients of transported quantities and that they don't take rotational effects into account (for further details see Sections 1.2 and 2.1). Both of these limitations can be important for deep convection events (Burchard, 2002; Marshall and Schott, 1999). However, the mixing parameterization should be able to reproduce also shear-driven mixing since it is at least as important as convective mixing in the ocean. In this sense the second-order turbulence schemes are a better choice as they work well in shear-driven cases and can produce convection to some extent whereas schemes designed for convection like convective adjustment only work in convective cases.

1.1 Greenland Sea

The Greenland Sea is the northernmost part of the Nordic Seas (Blindheim and Østerhus, 2005), map of the area including two main surface currents is shown in Figure 1.1. In this study Nordic Seas refer to the three seas north of Greenland-Scotland ridge, Greenland Sea (which includes Boreas Basin and Greenland Basin), Norwegian Sea (which includes Lofoten Basin, Norwegian Basin and Vøring Plateau) and Iceland Sea (lying on Iceland Plateau). Greenland Sea is separated from the surrounding basins by underwater ridges which are mainly 1000-2000 meters deep with only some deeper inlets (Blindheim and Østerhus, 2005). To the north the Fram Strait connects Greenland Sea to the Arctic Ocean which presently ventilates the deep water of the Greenland Sea (Blindheim and Østerhus, 2005; Hansen and Østerhus, 2000). Knipovich ridge and Mohn ridge, which are part of the mid-Atlantic ridge, separate the Greenland Sea from the Norwegian Sea in the east and south-east (Blindheim and Østerhus, 2005). The southern border between Greenland Sea and Iceland Sea is formed by the Jan Mayen Fracture Zone (Blindheim and Østerhus, 2005).

The flow field in the Greenland Sea is cyclonic. In the east the warm West Spitsbergen Current (WSC) carrying Atlantic origin waters flows to northward and on the western side East Greenland Current (EGC) transports water and ice from the Arctic Ocean and Recirculating Atlantic Water (RAW) originating from WSC towards south (Rudels et al., 2002). The Greenland Sea gyre is created between these two currents. The surface circulation as well as the mid-depth circulation is thus cyclonic and controlled by the bottom topography and wind forcing (Voet et al., 2010; Jakobsen et al., 2011). Circulation together with bottom topography make Greenland Sea an isolated area and the main exchanges between the other basins are due to mesoscale and submesoscale processes (eddies) (Voet et al., 2010).

1.1.1 Water mass transformations

Greenland sea was chosen as study area since the water mass formed by convection contributes to the North-Atlantic Deep Water (NADW), which is an important component in the Atlantic Meridional Overturning Circulation (AMOC) (Hansen and Østerhus, 2000) and for the current climate (Ferrari and Ferreira, 2011). NADW is the densest water mass in the North-Atlantic and it is formed as the dense water from

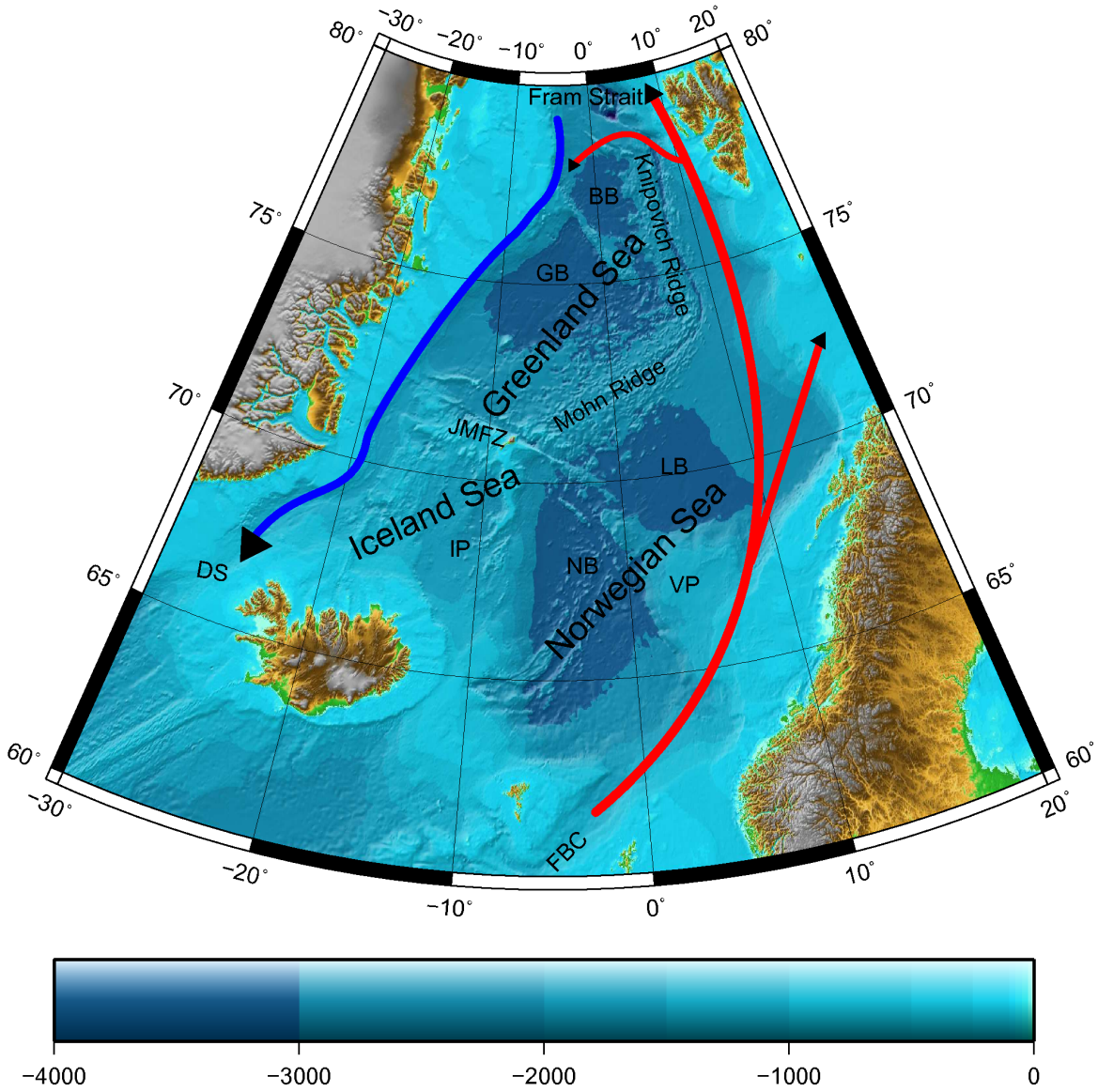

Figure 1.1: Map of the Nordic Seas. The main surface currents are sketched with arrows. Blue arrows represent East Greenland Current (EGC) and red arrows represent North-Atlantic Current (NAC) and West Spitsbergen Current (WBC). Other acronyms are as follows: Boreas Basin (BB), Denmark Strait (DS), Faroe Bank Channel (FBC), Greenland Basin (GB), Iceland Plateau (IP), Jan Mayen Fracture Zone (JMFZ), Lofoten Basin (LB), Norwegian Basin (NB) and Vøring Plateau (VP). This image was created with Generic Mapping Tools (GMT), available from `gmt.soest.hawaii.edu`.

the Arctic Mediterranean (Arctic Ocean and Nordic Seas) flows over the Greenland-Scotland ridge and entrains ambient water masses (Hansen and Østerhus, 2000). The overflow is concentrated to two channels, Denmark Strait west of Iceland and Faroe Bank channel south of Faroe Islands (Hansen and Østerhus, 2000). The waters flowing trough the Denmark Strait form the densest component of the NADW, since initially denser Faroe Bank channel overflow water experiences stronger entrainment. These overflows continue southwards as a deep western boundary current along Greenland continental slope. Further south also Labrador Sea Water contributes to the NADW. Although dense water masses are produced in the Greenland Sea they have been shown to be of minor importance for the overflow waters (Våge et al., 2011; Eldevik et al., 2009; Jeansson et al., 2008; Latarius and Quadfasel, 2010; Segtnan et al., 2011). It should be noted that although Eldevik et al. (2009) reported that Greenland Sea Water (GSW) contributes 61 % to the Faroe Bank channel overflow and 31 % to the Denmark Strait overflow in their study GSW referred to all the waters formed locally in the Nordic Seas. Although most of the water mass transformations seems to take place in the eastern Nordic Seas and Arctic Ocean (Segtnan et al., 2011; Latarius and Quadfasel, 2010; Mauritzen, 1996), the eddy exchange across the Arctic front (between Norwegian Sea and Greenland/Iceland Seas) accounts for 30 % of the heat loss and 40 % of freshwater gain in the Norwegian Sea according to Segtnan et al. (2011). Also Latarius and Quadfasel (2010) and Budeus and Ronski (2009) noted the importance of this cross frontal exchange.

Observations from the beginning of the 20th century showed that the density structure at Greenland Sea exhibited an upward doming of the isopycnals in the central gyre. This structure is favorable for deep reaching convection induced by winter time cooling. However, nowadays a clear two layer structure is found: upper layer is separated from the lower by salinity and density step at mid-depths (Karstensen et al., 2005; Ronski and Budeus, 2005; Budeus and Ronski, 2009). The intermediate temperature maximum (Budeus and Ronski, 2009), which was present in 1990's and early 2000 is not seen anymore. According to Budeus and Ronski (2009) the density structure was formed after 1989 and 1990 when a strong freshwater input to the Greenland Sea restricted the winter convection to few hundred meters for several years allowing the density gradient to develop to mid-depth. Since then the interface has been gradually deepening although the deepening is not directly related to winter convection (Budeus and Ronski, 2009). Budeus and Ronski (2009) related the changes in the deeper layer to lateral advection of waters from Arctic Ocean (salinity increase) and deepening of the interface (increasing temperature). Despite the fact that there has been no evi-

dence of bottom reaching convection since 1980's, intermediate convection still exists (Budeus and Ronski, 2009; Ronski and Budeus, 2005; Gascard et al., 2002). Marshall and Schott (1999) and Visbeck et al. (1995) discussed the importance of ice formation on the preconditioning of convection in the Greenland Sea, but more recent work by Ronski and Budeus (2005) suggests that the ice formation is of lesser importance at least for the intermediate convection. Recently deeper reaching convection due to sub-mesoscale coherent vortices has been described by Gascard et al. (2002), Budeus et al. (2004) and Ronski and Budeus (2006). However, despite the deep reaching convection, the density inside these anti-cyclonic vortices correspond to that of surrounding waters at intermediate layers, which implies that they don't affect the deep water properties, but are rather a form of intermediate convection. In fact Budeus and Ronski (2009) noted that the salinity/density interface between the upper and lower layer is displaced downwards in the center of these vortices and the waters don't penetrate trough the interface. Also Marshall and Schott (1999) concluded that the convective plumes are nonpenetrative, meaning that sinking plumes stop at the level of neutral buoyancy.

1.1.2 Forcing mechanisms behind the convection

The main driving force for the convection in the Greenland Sea is the buoyancy loss induced by the winter time cooling (Marshall and Schott, 1999). However, also a number of other features has been shown to affect the mixing and convection in the Greenland Sea. Since the density of seawater is a complicated nonlinear function of temperature, salinity and pressure the stratification itself can form instabilities in the ocean (Marshall and Schott, 1999; IAPWS, 2008). The main forms of the instabilities arising from the nonlinearities of the equations of state of seawater are thermobaric instability and cabelling instability.

Thermobaric instability is due to the highly temperature and pressure dependent thermal expanse coefficient, i.e. warm water is less compressible than cold water. Instability can be generated, when a cold fresh layer (Arctic surface water) lies above warmer and more saline water (RAW layer) as often happens in Greenland Sea. In this situation a downward displaced particle (cold and fresh) experiences additional acceleration, as the particle becomes denser than the environment (warm and saline) due to its lower temperature and thus higher compressibility. However, Marshall and Schott (1999) showed that in typical Greenland Sea conditions the displacement

needed for thermobaric acceleration is in order of 800 meters, suggesting that themobaricity can only be a secondary driving factor in convection events. Recently Ronski and Budeus (2005) identified two possible forms of convection in the Greenland Sea, plume convection and mixed layer deepening. These findings have been explained to be due to the thermobaric effect (Akitomo, 2011, 1999). Akitomo (2011) showed that when arctic, cold and fresh, water is present at the surface thermobaric plume convection events occur whereas if the surface layer is occupied by warm and saline Atlantic water the mixed layer deepens and entrains with the deeper layers. In both cases surface cooling is the main driving factor, but in the first case thermobaric effect causes abrupt plume convection, while in the latter case plumes are absent and thermobaricity can practically be neglected (Akitomo, 2011).

Cabbeling instability is due to density dependence on the square of potential temperature and arises when mixing (horizontal or vertical) takes place with water masses of similar densities but different temperatures (Kasajima and Johannessen, 2009; Akitomo, 2011; Harcourt, 2005). The resulting water mass will be denser than either of the initial water masses and can trigger convective plumes (Akitomo, 2011; Harcourt, 2005). The study by Kasajima and Johannessen (2009) showed that cabbeling could be important water mass transformation process in the Greenland Sea. Their study was based on summer data, but they suggested that the cabbeling could be even more important during the winter than in summer.

Furthermore double-diffusion follows from differences in molecular diffusivity of heat and salt. Thermal conductivity is about 100 times the diffusivity of salt and thus water parcel can lose heat while salinity remains almost constant. Density changes accordingly and static instability can be generated if the underlaying stratification is suitable (i.e when warm and salty water lays on cold and less salty water mass). Clarke et al. (1990) suggested this phenomenon to be important for the deepest layers of the Greenland Sea, but more recent studies imply that the lateral advection of the Arctic Ocean Deep Water from the East Greenland Current or other forms of diapycnal mixing (e.g internal wave induced mixing) are more important processes in the deep layer (Karstensen et al., 2005; Visbeck and Rhein, 2000; Naveira Garabato et al., 2004).

1.2 Turbulence parameterizations

This section provides a short introduction to different turbulence parameterizations. More detailed description is given in section 2.1. Statistical closures started to be developed in the 1970s but were introduced to oceanography in large scale mainly after 1980's. This was probably because the focus on oceanographic problems was mainly on large scale circulation and all the available computer resources were rather allocated to increased resolution, as the traditional empirical formulations provided reasonable results (Burchard, 2002). The parameterizations used today can be separated into two different main branches: statistical turbulence closures and empirical closures (Burchard, 2002; Large et al., 1994). The need for closures follows when Reynolds's decomposition is applied to Navier-Stokes equations (see 2.1). This method leads to additional terms (see equation 1.1 below) which are correlations between two flow properties in the same location and the Navier-Stokes equations are no longer closed. Equations for these correlations terms can be further derived (see Burchard (2002) page 18), but they will include higher order correlation terms. In fact equations for higher correlations can be also derived, but they will always depend on even higher order correlations, this problem leads to so called Friedmann-Keller series (Burchard, 2002). In geophysical research usually only the second order correlations are considered and tracer cross-correlations (e.g. correlations between salinity and temperature) are neglected (Burchard, 2002). The remaining correlations between velocity components and velocity components and tracers, turbulent fluxes, are closed by assuming the correlations to be proportional to vertical gradients of the parameters (Burchard, 2002). Formally the relation can be written as

$$\left\langle \tilde{w}\tilde{\phi} \right\rangle = -\nu_t \frac{\partial \phi}{\partial z} \tag{1.1}$$

where $\tilde{w}$ is the turbulent fluctuation of the velocity, $\tilde{\phi}$ is the turbulent fluctuation of some quantity ϕ and ν_t is the eddy viscosity (see section 2.1.1). This so called eddy viscosity approximation is, however, known to underestimate the third-order fluxes (Burchard, 2002) and for example (Large et al., 1994) uses an additional term to compensate for these effects. The main difference between the different closures is then the way the eddy viscosity is obtained. In statistical 2. order models it depends on the turbulent kinetic energy, its dissipation (or related quantities, see section 2.1), and square of shear and Brunt-Vaisala frequencies. A simpler approach is to take ν_t to depend only on some empirical parameters and Richardson number (Large et al., 1994). In addition to these closures mixed layer has been modelled

by simply mixing the water column based on instabilities in the density structure. Convective adjustment is an example of this approach (see section 2.1.2).

It is important to realize that although the turbulence parameterizations could lead to better description of some oceanic phenomenon they cannot provide any further understanding of turbulence. For better understanding of turbulence one needs to use methods such as Direct Numerical Simulations (DNS) and Large Eddy Simulations (LES). These methods solve full (DNS) or filtered (LES) Navier-Stokes equations, but since the intent is to solve huge range of scales time step and spatial grid size are restricted to very small scale and this is why these methods at the moment can be used only in small tests. Important validation data for turbulence parameterizations can be produced, however. In addition to these numerical methods one would expect to have validation data from field measurements. In recent years ocean observations have developed and it is possible to obtain for example high resolution turbulence dissipation observations (Burchard, 2002). However, these measurements are restricted by similar if not a greater amount of assumptions as are the numerical models and the effect of turbulence alone is hard to identify (Burchard, 2002). This is why the main validation of the parameterizations should be done against theory, higher order numerical simulations and laboratory experiments (Burchard, 2002).

1.3 Outline

The main goal of this study is to model the oceanic state in the Greenland Sea over the winter 2010–2011 with the 1-D GOTM model (Umlauf et al., cited july 2011; Burchard, 2002) and compare the results with observations from three Argo buoys. The intention is to model ocean state following the path of the specific Argo float, something which has not been done before. With this approach the study seeks to describe the evolution of the convective boundary layer and to find which of the parameterization in GOTM performs the best when convection is present.

A second purpose of this study is to examine the winter convection during the winter 2010-11 in the Greenland Sea and to determine which convection scenario of those introduced by Ronski and Budeus (2005) and discussed by Akitomo (2011) and Budeus and Ronski (2009), plume convection or mixed layer deepening, it fits (if any).

The third aim of the study is to show whether modelling the ocean state along the float's path gives any added value compared to using one location like Ronski and Budeus (2005) did. In this sense quality of atmospheric forcing as well as its resolution sets one limit to the model performance. Marshall and Schott (1999) noted that more than the differences in the vertical mixing schemes the quality of the atmospheric forcing and the knowledge of the initial conditions define the success of the model run. In this study the initial conditions are well known so the crucial point is the atmospheric forcing. Thus, a last question arises, is the atmospheric forcing used in this study suitable for the modelling of this kind?

As seen from these aims the purpose of the study is to examine the convection itself and the suitability of existing parameterizations to model it. The significance of the convection in the Greenland Sea is discussed on the basis of past studies, but the intention of this work is not to study it further. Also the sub-mesoscale coherent vortices (Gascard et al., 2002) are out of the scope of this study.

This study is structured as follows: Chapter 2 provides a description of the observations and the model on which this study is based. Sections 2.1 and 2.2 explain the theoretical basis of the modern turbulence closures and show how the theory is implemented in the GOTM model. The section 2.3 gives a description of the observations and atmospheric forcing data used. Chapter 3 describes the main results from the analysis of model and Argo data. The chapter 3.3 is for comparing the results of this study to the previous work done in the area as well as for discussion of the model restrictions and effect of the atmospheric forcing. Conclusive summary and future outlook are given in chapter 4

Chapter 2

Materials and Methods

General Ocean Turbulence Model (GOTM) (Burchard, 2002) has been used in this work to model the ocean state in the Greenland Sea. GOTM is published under the GNU public license and is freely available for anyone from the following web page: `www.gotm.net`. The model itself has a large and relatively comprehensive documentation so the aim of this chapter is not to reproduce it but to describe briefly the main turbulence theory behind GOTM and to give a more detailed description of the set up used in this study. First the reader is introduced to the hydrostatic primitive equations and then the basics of turbulence modelling are reviewed.

2.1 Theory

In this section it is shown how one treats the 3-D Navier-Stokes and tracer equations to gain the 1-D primitive equation set including the closure assumptions for the turbulent fluxes. In the section 2.2 these equations are then further simplified on the basis of the assumptions made in this study to obtain the model equations. For simplicity the notation in this section and through the whole thesis follows Burchard (2002). Bold letters will be used for vectors, overbar for mean fields, tilde for fluctuation fields and capital letters for scalar fields. In addition chevrons (angle brackets) are used to denote (time) average.

Assuming incompressibility i.e. assuming vertical density variations from the mean

value to be small (Boussinesq approximation, see e.g. Shchepetkin and McWilliams (2011) for a discussion about the errors and problems related to this approximation) the Navier-Stokes equation (2.1) and the continuity equation (2.2), can be written in vector form as

$$\frac{\partial \mathbf{v}}{\partial t} + \mathbf{v} \cdot \nabla \mathbf{v} - \nu \nabla^2 \mathbf{v} + 2\boldsymbol{\Omega} \times \mathbf{v} = -\frac{\nabla p}{\rho_0} - \frac{\rho}{\rho_0}\mathbf{g} \tag{2.1}$$

$$\nabla \cdot \mathbf{v} = 0 \tag{2.2}$$

Where $\mathbf{v}$ is the three dimensional velocity vector, p is the pressure and ρ is the density field. Other variables are the gravitation $\mathbf{g} = (0, 0, g)$ where $g = 9.81$ m s^{-2} is the gravitational acceleration, earths rotation $\boldsymbol{\Omega} = (0, \Omega\cos(\phi), \Omega\sin(\phi))$ where $\Omega = 7.289 \cdot 10^{-5}$ s^{-1} is the angular velocity of the Earth and ϕ is the latitude. Symbol ν denotes the kinematic viscosity which is strongly temperature dependent. ρ_0 is a given constant reference density.

To be able to calculate the density ρ in the ocean we write the equations for the (active) tracers, potential temperature Θ and salinity S. In vector from they become

$$\frac{\partial \Theta}{\partial t} + \mathbf{v} \cdot \nabla \Theta - \nu^{\Theta} \nabla^2 \Theta = \frac{1}{c_p' \rho_0} \frac{\partial I}{\partial z} \tag{2.3}$$

where I is local solar radiation, c_p' is the specific heat capacity of sea water and $\nu^{\Theta} = 1.38 \cdot 10^{-7}$ m^2 s^{-1} is the molecular diffusivity of heat. Similarly for salinity we get

$$\frac{\partial S}{\partial t} + \mathbf{v} \cdot \nabla S - \nu^{S} \nabla^2 S = 0 \tag{2.4}$$

Where $\nu^S = 1.1 \cdot 10^{-9}$ m^2 s^{-1} is the molecular diffusivity of salt. The potential density is determined using the equation of state by Jackett et al. (2006) (see also discussion in appendix A).

The next step is to apply ensemble averaging (see Burchard (2002) page 15) to the Navier-Stokes equations to gain Reynold's-averaged Navier Stokes equations. First we consider Reynolds decomposition which states that any prognostic variable s can be written as a sum of mean field $\bar{s} = \langle s \rangle$ and fluctuating field $\tilde{s}$, formally

$$s = \bar{s} + \tilde{s} \tag{2.5}$$

where by definition the mean of fluctuation part vanishes:

$$\langle \tilde{s} \rangle = 0 \tag{2.6}$$

Then we apply the Reynolds decomposition and ensemble averaging to the equations (2.2) - (2.4) and by scale analysis using boundary-layer approximation (vertical scale is 10^{-4} times smaller than horizontal scale) we can leave out the small terms such as horizontal derivatives of Reynolds stresses, horizontal diffusivities and vertical Coriolis acceleration (Burchard, 2002). By doing so we gain the following equations (not written for vertical momentum as it will not appear in the final 1-D set of equations) now written in Cartesian coordinates

$$\frac{\partial \bar{u}}{\partial t} + \frac{\partial}{\partial x}(\bar{u}^2) + \frac{\partial}{\partial y}(\bar{u}\bar{v}) + \frac{\partial}{\partial z}(\bar{u}\bar{w}) - \nu\frac{\partial^2 \bar{u}}{\partial z^2} + \frac{\partial}{\partial z}\left\langle \tilde{u}\tilde{w}\right\rangle - 2\Omega\sin(\phi)\bar{v} = -g\frac{\bar{p}(\zeta)}{\rho_0}\frac{\partial \zeta}{\partial x} + \int_z^\zeta \frac{\partial b}{\partial x}dz' \tag{2.7}$$

$$\frac{\partial \bar{v}}{\partial t} + \frac{\partial}{\partial x}(\bar{u}\bar{v}) + \frac{\partial}{\partial y}(\bar{v}^2) + \frac{\partial}{\partial z}(\bar{v}\bar{w}) - \nu\frac{\partial^2 \bar{v}}{\partial z^2} + \frac{\partial}{\partial z}\left\langle \tilde{v}\tilde{w}\right\rangle + 2\Omega\sin(\phi)\bar{u} = -g\frac{\bar{p}(\zeta)}{\rho_0}\frac{\partial \zeta}{\partial y} + \int_z^\zeta \frac{\partial b}{\partial y}dz' \tag{2.8}$$

$$\frac{\partial \bar{u}}{\partial x} + \frac{\partial \bar{v}}{\partial y} + \frac{\partial \bar{w}}{\partial z} = 0 \tag{2.9}$$

$$\frac{\partial \bar{\Theta}}{\partial t} + \frac{\partial}{\partial x}(\bar{u}\bar{\Theta}) + \frac{\partial}{\partial y}(\bar{v}\bar{\Theta}) + \frac{\partial}{\partial z}(\bar{w}\bar{\Theta}) - \nu^\Theta\frac{\partial^2 \bar{\Theta}}{\partial z^2} + \frac{\partial}{\partial z}\left\langle \tilde{w}\tilde{\Theta}\right\rangle = \frac{1}{c'_p\rho_0}\frac{\partial I}{\partial z} \tag{2.10}$$

$$\frac{\partial \bar{S}}{\partial t} + \frac{\partial}{\partial x}(\bar{u}\bar{S}) + \frac{\partial}{\partial y}(\bar{v}\bar{S}) + \frac{\partial}{\partial z}(\bar{w}\bar{S}) - \nu^S\frac{\partial^2 \bar{S}}{\partial z^2} + \frac{\partial}{\partial z}\left\langle \tilde{w}\tilde{S}\right\rangle = 0 \tag{2.11}$$

$$\bar{\rho} = \rho\left(\bar{\Theta}, \bar{S}, p_0\right) \tag{2.12}$$

In the above equations ζ is the surface elevation and b is the buoyancy

$$b = -g \cdot \frac{\bar{\rho} - \rho_0}{\rho_0} \tag{2.13}$$

2.1.1 Traditional turbulence closures

The hydrostatic primitive equations (2.7)-(2.12) now only contain four turbulent transport terms $\langle\tilde{u}\tilde{w}\rangle$, $\langle\tilde{v}\tilde{w}\rangle$, $\left\langle\tilde{w}\tilde{T}\right\rangle$, $\left\langle\tilde{w}\tilde{S}\right\rangle$. For these terms one has to make closure assumptions. Different closure assumptions are presented and widely discussed in Burchard (2002) and only the general result is presented here. First we define the turbulent kinetic energy, k, and the dissipation rate of turbulent kinetic energy, ϵ, in

Cartesian coordinate form as

$$k = \frac{1}{2}\left(\left\langle \tilde{u}^2 \right\rangle + \left\langle \tilde{v}^2 \right\rangle + \left\langle \tilde{w}^2 \right\rangle\right) = \frac{1}{2}q^2 \tag{2.14}$$

$$\epsilon = \nu\left(\left\langle (\nabla\tilde{u})^2 \right\rangle + \left\langle (\nabla\tilde{v})^2 \right\rangle + \left\langle (\nabla\tilde{w})^2 \right\rangle\right) \tag{2.15}$$

Despite the different approaches to close the second order turbulent transport terms the common forms can be written using k and ϵ as

$$\langle \tilde{u}\tilde{w} \rangle = -\nu_t \frac{\partial \bar{u}}{\partial z} = -c_\mu \frac{k^2}{\epsilon}\frac{\partial \bar{u}}{\partial z} \tag{2.16}$$

$$\langle \tilde{v}\tilde{w} \rangle = -\nu_t \frac{\partial \bar{v}}{\partial z} = -c_\mu \frac{k^2}{\epsilon}\frac{\partial \bar{v}}{\partial z} \tag{2.17}$$

$$\left\langle \tilde{w}\tilde{\Theta} \right\rangle = -\nu'_t \frac{\partial \bar{\Theta}}{\partial z} = -c'_\mu \frac{k^2}{\epsilon}\frac{\partial \bar{\Theta}}{\partial z} \tag{2.18}$$

$$\left\langle \tilde{w}\tilde{S} \right\rangle = -\nu'_t \frac{\partial \bar{S}}{\partial z} = -c'_\mu \frac{k^2}{\epsilon}\frac{\partial \bar{S}}{\partial z} \tag{2.19}$$

Similarly for vertical density flux we can write

$$\langle \tilde{w}\tilde{\rho} \rangle = -\nu'_t \frac{\partial \bar{\rho}}{\partial z} = -c'_\mu \frac{k^2}{\epsilon}\frac{\partial \bar{\rho}}{\partial z} \tag{2.20}$$

Where ν_t and ν'_t are the eddy viscosities for momentum and active tracers (heat and salt), respectively. Similarly c_μ and c'_μ are the non-dimensional stability functions for momentum and active tracers, respectively. There are again number of different forms of these stability functions. In the simplest case these stability functions are treated as empirical constants (standard k-ϵ model, see the end of this chapter). Often they are treated as a functions of non-dimensional numbers. Although these kind of functions differ, they all are based on shear number, α_M, and buoyancy number, α_N, given as follows

$$\alpha_M = \frac{k^2}{\epsilon^2}M^2, \alpha_N = \frac{k^2}{\epsilon^2}N^2 \tag{2.21}$$

With the shear frequency squared, $M^2 = (\frac{\partial \bar{u}}{\partial z})^2 + (\frac{\partial \bar{u}}{\partial z})^2$ and the buoyancy frequency squared $N^2 = \frac{\partial \bar{b}}{\partial z}$

There are number of ways to solve k and ϵ as discussed in the end of this section. One of the more complex methods is to derive exact transport equations for both k and ϵ (see e.g (Burchard, 2002)). This method is shortly reviewed here. Assuming horizontal homogeneity the transport equation for turbulent kinetic energy, k, can be

written as

$$\frac{\partial k}{\partial t} + \frac{\partial}{\partial z}\left(\langle \tilde{w}k \rangle - \nu \frac{\partial k}{\partial z}\right) = P + B - \epsilon \tag{2.22}$$

Where P is the shear production, B is the buoyancy production and ϵ is the dissipation rate of turbulent kinetic energy. With the same assumptions we get the following equation for dissipation of turbulent kinetic energy, ϵ,

$$\frac{\partial \epsilon}{\partial t} + \frac{\partial}{\partial z}\left(\langle \tilde{w}\epsilon \rangle - \nu \frac{\partial \epsilon}{\partial z}\right) = P_\epsilon + B_\epsilon - \epsilon_\epsilon \tag{2.23}$$

Where the terms on the right hand side are defined similarly to those of the equation for k, they are shear production of dissipation, P_ϵ, buoyancy production of dissipation, B_ϵ, and dissipation of dissipation, ϵ_ϵ (includes all gradients of ϵ). The final form of the equations (2.22) and (2.23) depends on the model in question (discussed below). Usually down gradient approximation, similar to equations (2.16)–(2.20), is used to close the terms $\langle \tilde{w}k \rangle$ and $\langle \tilde{w}\epsilon \rangle$. Often the right hand side of the (2.23) is written by multiplying the right hand side of the (2.22) with suitable empirical constants. Quantities k and ϵ are linked to each other by the following relation defining the macro length scale L:

$$L = c_L \frac{k^{\frac{3}{2}}}{\epsilon} \tag{2.24}$$

where c_L is the neutral stability function, which is the value of c_μ when $B = 0$ and $P = \epsilon$.

In the system of equations presented above the turbulent kinetic energy, k and its dissipation rate occur as unknowns. One of the following three main methods are usually used to solve them:

1. The simplest way is to calculate both k and ϵ from algebraic relations. Value for k is achieved by setting the right hand side of the equation (2.22) to zero (local equilibrium condition). By calculating value for length scale L by some algebraic relation, or even taking a value from prescribed vertical distribution, one can determine the ϵ using the relation (2.24).

2. A bit more complex form of closure is to compute k from differential transport equation based on the equation (2.22), while L is still determined from an empirical or theoretical relation and converted to ϵ with (2.24).

3. The most complex model in this sense is then a model in which both k and ϵ (or some quantity from which ϵ can be derived e.g. kL or ω) are calculated from

differential transport equations. This kind of models are called two-equation models. The most well known special cases in this class of models are $k-\epsilon$ model, $k-\omega$ ($\omega = \epsilon/k$) model and $k-k$L model (Mellor-Yamada model). The main difference between the models is the way ϵ is calculated: in the $k-\epsilon$ model the transport equation for ϵ is used while in the others use transport equation for related quantity. Burchard (2002) has discussed generic two equation model, which explains differences between some of the aforementioned models. The idea is that if the equation (2.24) is applicable then the right hand side of equation (2.23) can be modelled with any quantity $k^n\epsilon^m$ ($m \neq 0$). The request $m > 0$ follows from the definition of turbulent Schmidt number (turbulent diffusion divided by molecular diffusion) which should be positive and whose sign in this case is determined by the m. Most notably this approach leads to the conclusion that all models with $m < 0$, such as $k-k$L(Mellor-Yamada model) model with $m = -1$, do not fit this concept and require additional term to capture length scale L near walls (for more details see Umlauf (2011) and Burchard (2002)).

2.1.2 Other approaches

In addition to the methods described above two quite common, but different, approaches to treat mixing exist.

The first one is the so called convective adjustment. The idea is to compare each model layer with the layer below for static instability. This is done by calculating Brunt-Vaisala frequency squared, $N^2 = \frac{\partial b}{\partial z}$ (buoyancy b is defined in (2.13)), and mixing the two layers if $N^2 < 0$. This check is done from the surface to the first layer where $N^2 \geq 0$ or until the bottom. This parameterization lacks several features, but works in simple convective cases.

The second method, K-Profile Parameterization (hereafter KPP), was first introduced for ocean by Large et al. (1994). The method is somewhat similar to the equations (2.16)-(2.20) but there is an additional term $\tilde{\Gamma}_{\bar{\varphi}}$. This term accounts for non-local vertical fluxes, which mimic the effect of large eddies that advect water across large vertical distances before smaller eddies mix the parcels with the environment (Stull, 1993). Formally the parameterization can be written as

$$\langle \tilde{w}\tilde{\varphi} \rangle = -\nu_t^{\varphi} \frac{\partial \bar{\varphi}}{\partial z} + \tilde{\Gamma}_{\bar{\varphi}} \tag{2.25}$$

where φ is the desired variable. The non-local flux term is defined as

$$\tilde{\Gamma}_{\bar{\varphi}} = \nu_t^{\varphi} \gamma_{\varphi} \tag{2.26}$$

where γ_{φ} is the actual non-local flux term and ν_t^{φ} is the eddy viscosity which in this case is defined as

$$\nu_t^{\varphi} = h w_{\varphi}(\sigma) G(\sigma) \tag{2.27}$$

where $G(\sigma)$ is a cubic shape function (polynomial with 4 empirical coefficients, see also O'Brien (1970)), h is the depth of the mixed layer, w is the velocity scale and $\sigma = d/h$ is the non-dimensional vertical coordinate, defined so that at the bottom of mixed layer $d = h$ and $\sigma = 1$, h is defined to be depth where bulk Richardson number reaches the critical value $Ri_c = 0.3$. For further definitions see Large et al. (1994) and Umlauf et al. (cited july 2011). Non-local flux term γ_{φ} is non zero for scalars in unstable conditions, for momentum it is set to zero since such a term cannot be determined for the momentum as it can be for heat and salt (Large et al., 1994). The strength of the KPP parameterization is that the non-local flux term can account for counter-gradient transport, which can be important in convective mixing. The other parameterizations used in this study cannot account for such fluxes.

2.2 GOTM model

GOTM is a one dimensional model which implies that horizontal gradients have to be neglected (horizontal homogeneity) or prescribed. Horizontally homogeneous situation is assumed in this work, despite the barotropic pressure gradient which is given as an average velocity. This assumption is considered to be well justified as the purpose is to model ocean state along a path of semi-Lagrangian float. Furthermore according to Voet et al. (2010) advection from other basins is small, which further justifies the horizontal homogeneity. However, this assumption might be questionable near the edge currents. As noted in the Section 1.1 some authors (Segtnan et al., 2011; Latarius and Quadfasel, 2010) have found evidence of significant fluxes over the arctic front at eastern rim of the Greenland Sea and strong horizontal gradients are present also at the western rim near East Greenland Current. The governing equations of the model are reviewed in this section following mainly the model description by Umlauf et al. (cited july 2011) and Burchard (2002).

2.2.1 Momentum equations

Momentum equations (2.7) and (2.8) have been derived in the previous chapter. They have been implemented in GOTM in the following form

$$\begin{aligned}\frac{D\bar{u}}{Dt} = &\overbrace{\frac{\partial}{\partial z}\left((\nu_t+\nu)\frac{\partial \bar{u}}{\partial z} - \tilde{\Gamma}_{\bar{u}}\right)}^{1} - \overbrace{g\frac{\partial \zeta}{\partial x}}^{2} + \overbrace{\int_z^\zeta \frac{\partial b}{\partial x}dz'}^{3} \\ &\underbrace{-\frac{1}{\tau_R^{\bar{u}}}(\bar{u}-\bar{u}_{obs})}_{4} - \underbrace{C_f\bar{u}\sqrt{\bar{u}^2+\bar{v}^2}}_{5} + \underbrace{2\Omega\bar{v}\sin(\phi)}_{6}\end{aligned} \tag{2.28}$$

Where advection has been neglected and $\rho(\zeta)/\rho_0 = 1$ is assumed (i.e. ρ_0 is the surface density). The terms on the right hand side are as follows:

1. Vertical mixing, different methods to calculate this term are discussed in the previous section
2. External pressure gradient
3. Internal pressure gradient
4. Relaxation term. Used in case of assimilation of the observations (not in this study), $\tau_R^{\bar{u}}$ is then the relaxation time scale and $\bar{u}_{obs}$ is the observed eastward velocity field
5. Bottom friction, C_f is the friction coefficient
6. Coriolis acceleration

Since there is no bottom friction in this study (free bottom), no assimilation of the observations and no internal pressure gradients the equation (2.28) can be simplified to

$$\frac{D\bar{u}}{Dt} = \frac{\partial}{\partial z}\left((\nu_t+\nu)\frac{\partial \bar{u}}{\partial z} - \tilde{\Gamma}_{\bar{u}}\right) - g\frac{\partial \zeta}{\partial x} + 2\Omega\bar{v}\sin(\phi) \tag{2.29}$$

and similarly for the northward velocity component $\bar{v}$ we have

$$\begin{aligned}\frac{D\bar{v}}{Dt} = &\frac{\partial}{\partial z}\left((\nu_t+\nu)\frac{\partial \bar{v}}{\partial z} - \tilde{\Gamma}_{\bar{v}}\right) - g\frac{\partial \zeta}{\partial y} + \int_z^\zeta \frac{\partial b}{\partial y}dz' \\ &-\frac{1}{\tau_R^{\bar{v}}}(\bar{v}-\bar{v}_{obs}) - C_f\bar{v}\sqrt{\bar{u}^2+\bar{v}^2} - 2\Omega\bar{u}\sin(\phi)\end{aligned} \tag{2.30}$$

and the simplifications of this study giving

$$\frac{D\bar{v}}{Dt} = \frac{\partial}{\partial z}\left((\nu_t + \nu)\frac{\partial \bar{v}}{\partial z} - \tilde{\Gamma}_{\bar{v}}\right) - g\frac{\partial \zeta}{\partial y} - 2\Omega\bar{u}\sin(\phi) \tag{2.31}$$

The external pressure gradient term is given by the float velocity which is calculated from the surfacing positions. The float velocity is assumed to describe the average velocity of the water column. The pressure gradient terms become

$$-g\frac{\partial \zeta}{\partial x} = -2\Omega v_{float}\sin(\phi) \tag{2.32}$$

and

$$-g\frac{\partial \zeta}{\partial y} = 2\Omega u_{float}\sin(\phi) \tag{2.33}$$

Where u_{float} and v_{float} are the known float velocity components, f is Coriolis acceleration, g is the gravitational acceleration and ζ is the sea surface height. So the float velocities are simply added to the velocity component in Coriolis acceleration (last term in equations 2.29 and 2.31)

2.2.2 Tracer equations

The heat balance equation (2.10) was introduced in the previous chapter, one dimensional form of same equations is implemented in GOTM as follows

$$\frac{D\bar{\Theta}}{Dt} = \frac{\partial}{\partial z}\left((\nu_t^{\bar{\Theta}} + \nu^{\bar{\Theta}})\frac{\partial \bar{\Theta}}{\partial z} - \tilde{\Gamma}_{\bar{\Theta}}\right) - \frac{1}{\tau_R^{\bar{\Theta}}}(\bar{\Theta} - \bar{\Theta}_{obs}) + \frac{1}{c_p'\rho_0}\frac{\partial I(z)}{\partial z} \tag{2.34}$$

The terms on the right hand side are similar to those in the equation (2.28), Expect the last term on the right hand side which in this case is the solar radiation term. c_p' is the heat capacity of sea water (constant $c_p' = 3985$ J kg^{-1} is assumed), ρ_0 is the density of the sea water and $I(z)$ is the actual solar radiation at the depth z. It is calculated according to the following exponential equation.

$$I(z) = I_0\left(Ae^{z/\nu_1} + (1-A)e^{z/\nu_2}\right) \tag{2.35}$$

Where I_0 is the radiation at the surface. ν_1 and ν_2 are the extinction scales which depend on the Jerlov water type (Jerlov, 1968) and A is the fraction of longer wavelengths in total radiance, which also depends on the Jerlov water type. In this study they were prescribed by choosing class I (see also Umlauf et al. (cited july 2011)),

which gives the coefficients the following values:

- $A = 0.58$
- $\nu_1 = 0.35$ m
- $\nu_2 = 23.00$ m

This then means that 58 % of the incoming radiation has extinction scale of 0.35 m and 42 % of the radiation has extinction scale of 23.00 m. Physically the part of the radiation with short extiction scale refers to longer wavelengths and the part with longer extinction scale refers to shorter wavelengths (note that $I(z)$ denotes short wave radiation and terms longer and shorter both refer to the radiation inside shortwave radiation band).

With the simplifications of this study the heat equation (2.34) (no relaxation to observations) can be written as

$$\frac{D\bar{\Theta}}{Dt} = \frac{\partial}{\partial z}\left((\nu_t^{\bar{\Theta}} + \nu^{\bar{\Theta}})\frac{\partial\bar{\Theta}}{\partial z} - \tilde{\Gamma}_{\bar{\Theta}}\right) + \frac{1}{c_p\rho_0}\frac{\partial I(z)}{\partial z} \tag{2.36}$$

The one dimensional salinity equation resembles the heat equation and can be written as

$$\frac{D\bar{S}}{Dt} = \frac{\partial}{\partial z}\left((\nu_t^{\bar{S}} + \nu^{\bar{S}})\frac{\partial\bar{S}}{\partial z} - \tilde{\Gamma}_{\bar{S}}\right) \tag{2.37}$$

Again terms on the right hand side are similar to those in the equation (2.28).

2.2.3 Boundary conditions

All the equations presented above have to be closed at least at the surface. This is done by setting boundary conditions for all the prognostic variables. In general these conditions determine directly the value of the variables at the boundary (Dirichlet type) or the value of the variables' vertical gradient (flux) at the boundary (Neumann type).

The surface boundary (at $z = \zeta$) conditions for momentum can be written as follows

$$\frac{\partial \bar{u}}{\partial z} = \frac{\tau_s^x}{\nu_t \rho}, \quad \frac{\partial \bar{v}}{\partial z} = \frac{\tau_s^y}{\nu_t \rho} \tag{2.38}$$

where τ_s^x and τ_s^y are the surface stress components for y and x directions, respectively.

The surface freshwater flux is given as precipitation-evaporation in the units of velocity (m/s). The Neumann type surface ($z = \zeta$) boundary condition for salinity is then

$$\frac{\partial}{\partial z}\left((\nu_t^{\bar{S}} + \nu^{\bar{S}})\frac{\partial \bar{S}}{\partial z} - \tilde{\Gamma}_{\bar{S}}\right) = P - E \tag{2.39}$$

where P is precipitation and E is evaporation.

The Neumann type boundary condition for temperature takes the following form

$$\frac{\partial}{\partial z}\left((\nu_t^{\bar{\Theta}} + \nu^{\bar{\Theta}})\frac{\partial \bar{\Theta}}{\partial z} - \tilde{\Gamma}_{\bar{\Theta}}\right) = \frac{Q_s + Q_l + Q_b}{\nu_t c_p' \rho_0} \tag{2.40}$$

Where Q_s is the sensible heat flux, Q_l is the latent heat flux and Q_b is the long wave back radiation.

In addition to boundary equations for momentum, salt and heat one needs boundary conditions for the turbulent kinetic energy k and its dissipation, ϵ. GOTM offers options for logarithmic boundary layer and shear-free boundary-layers with injection of turbulent kinetick energy. In both cases Dirichlet (prescribed) or Neumann (flux) condition can be chosen and in addition the exact form k-equation depends on the chosen turbulence model. All the possible options are described in Umlauf et al. (cited july 2011) and only the flux boundary conditions (used in this study) for k ($k - \epsilon$ style) and ϵ-equations are presented here, they can be written as follows

$$\frac{\partial k}{\partial z} = 0 \tag{2.41}$$

and

$$\frac{\partial \epsilon}{\partial z} = \frac{\left(c_\mu^0\right)^4 k^2}{\nu_t (z + z_0)} \tag{2.42}$$

Where c_μ^0 is the constant stability parameter of the model and z_0 is the roughness

Table 2.1: Some parameters from the three Argo floats used in the study.

WMO number	Type	Deployment date	Deployment Position (lat, lon)
6900801	APEX	23 Jun 2010	$75.850°N$, $2.216°W$
6900802	APEX	24 Jun 2010	$74.885°N$, $0.958°W$
6900811	NEMO	25 Jun 2010	$74.716°N$, $3.939°W$

length, which is calculated according to the following relation (Burchard, 2002):

$$z_0 = 1400\frac{u_*^2}{g} \tag{2.43}$$

where g is gravitational acceleration and the friction velocity is $u_*^2 = \sqrt{((\tau_s^x)^2 + (\tau_s^y)^2)}$. τ_s^x and τ_s^y are the surface stress components which are given by the surface forcing data. This equation is often called Charnock relation.

2.3 Argo float data

Data[1] from three Argo floats were used in this work to study the winter convection in the Greenland Sea. These floats were chosen because they operated in the Greenland Sea trough the whole study period from summer 2010 to summer 2011. Figure 2.1 shows the surface positions of the floats during the study period. There were also other floats in the area, but because their time series were not long enough, their data were not used. Table 2.1 summarizes the most important parameters from the floats used. All the floats had parking pressure of 1000 db, deep profile pressure of 2000 db and cycle length of 240 hours which equals 10 days. This means that the float drifts at the pressure of 1000 db for approximately 9 days, descends to 2000 db pressure level and makes a profile up to the surface and sends the data over a satellite to the ground station. The time the float drifts at 1000 db pressure level is less than 10 days since the cycle length refers to the time it takes from the float to complete the whole cycle, including the ascend and descend as well as the data transmission. The velocity of the float between two surfacings was calculated by comparing the last position and first position of the consecutive cycles. This was done in order to avoid the effect of

[1]These data where collected and made freely available by the International Argo Project and the national initiatives that contribute to it (`http://www.argo.net`). Argo is a pilot programme of the Global Ocean Observing System.

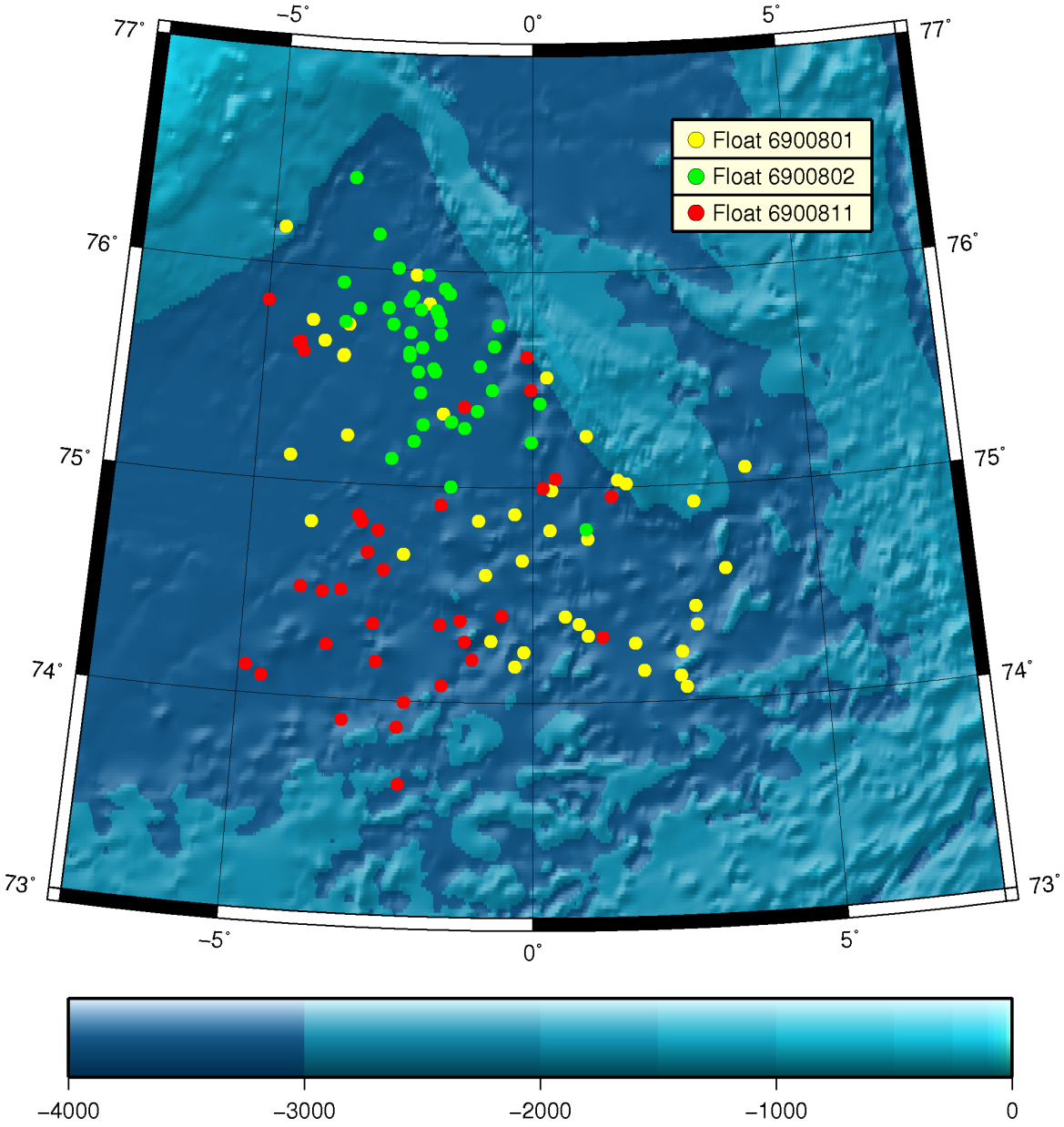

Figure 2.1: Map of the Greenland Sea with the Argo floats' surfacing positions indicated with dots (yellow for float 6900801, green for float 6900802 and red for float 6900811). This image was created with Generic Mapping Tools (GMT), available from `gmt.soest.hawaii.edu`.

surface drift on the average velocity during the $6 - 12$ hours the float spent at the surface sending the data.

All the floats were equipped with a standard SBE 41 CTD. This instrument uses MicroCAT temperature, conductivity, and pressure sensors. In this 41 version the pump provides 40 ml/sec flow for 2.5 sec/measurement, the start of the measurement is triggered by the float.

According to the manufacturer (Sea–Bird Electronics, Inc., 2011) SBE 41 CTD sensors have an accuracy of ± 0.002°C in temperature, ± 0.002 PSU in salinity (conductivity sensor) and ± 2 db in pressure. In addition to the accuracy, sensor might suffer from a drift, which is ± 0.0001°C/year for temperature, ± 0.001 PSU/year for salinity and ± 0.2 db/year for pressure. Since all of the floats were deployed during summer 2010 and had at most 1 year operating time behind them at the end of this study it's expected that the accuracy of the data at the end of the measuring period (including drift) was at least ± 0.003 PSU for salinity and ± 0.0021°C for temperature and ± 2.2 db for pressure.

2.4 Model setup

GOTM model has been used in vast range of ocean and limnologic applications (Burchard, 2002). The model version used in this study was GOTM-4.0. The model consist of the main physical core which has several extra modules e.g bio-module for biological applications. In this study only the main physical part was used. GOTM itself is more like an ocean engine than just one model as it has so many user specific options. These range from the number of different vertical mixing schemes to parameters such as bottom roughness. Since only observations from the Argo floats were used in this work most of the parameters were chosen based on literature. The most important choise in this kind of application is of course the turbulence parameterization. The available parameterizations were discussed in the previous section. Three parameterizations, $k - \epsilon$, $k - k$L (Mellor and Yamada model, hereafter MY) and KPP parameterizations were used in this study. The total number of runs was 24, since the model was run along the all three float trajectories using three different turbulent closure schemes, two forcings (ECMWF ERA-Interim, NCEP/NCAR) and making couple additional runs without non-local effects and with forcing picked up

Table 2.2: Vertical grid used in this study.

Depth [m]	grid size [m]
0–6	1
6–20	2
20–60	5
60–2000	10

from the median location (Eulerian approach).

Each run was done with the same vertical grid which had 216 levels, the resulting vertical grid resolution is given in Table 2.2. The time stepping was done according to the Crank-Nicolson scheme with 60 s time step. The time step was chosen to be only 60 s just for convenience, but it could be considerably larger and still numerically stable. Since the GOTM model is designed for modelling in one stationary position it can take only one latitude for the calculation of Coriolis parameter. The given latitude was the float's median position for both Lagrangian and Eulerian cases. The error arising from the use of constant Coriolis parameter is considerer to be negligible (theoretically it would affect the Ekman depth).

2.4.1 Surface boundary conditions

Since GOTM is an ocean model the surface boundary conditions, surface fluxes of heat, freshwater (salt) and momentum, have to be prescribed. These conditions can be given directly as prescribed quantities (nudging) or fluxes or as flux related variables such as surface air temperature and wind, in which case the model uses bulk formula to obtain the surface fluxes. Theoretical implementation used in this study is shown in section 2.2.3. Furthermore, whether the fluxes are given or calculated from other variables, the given values can be either modelled (reanalyzes) or observed. In this study two different atmospheric forcing data, from NCEP/NCAR reanalysis[2] (Kalnay et al., 1996) and ECMWF ERA-Interim reanalysis[3] (Dee et al., 2011), were used. Reanalyzes were used since, obviously, no atmospheric observations were available from the area. All the variables were available from the websites, but NCEP/NCAR

[2]NCEP/NCAR reanalysis data was provided by the NOAA/OAR/ESRL PSD, Boulder, Colorado, USA, from their Web site at `http://www.esrl.noaa.gov/psd/`

[3]ECMWF data was accessed trough their website at `http://data-portal.ecmwf.int/data/d/interim_daily/`

data did not include evaporation, E, which was calculated from latent heat flux, Q_L, with the following relation

$$E = \frac{1}{\rho_{fw}} \cdot \frac{Q_L}{L} \tag{2.44}$$

where ρ_{fw} is the density of freshwater (1000 kg m^3 was assumed), L is latent heat of vaporization (L is a function of salinity and temperature, median value calculated from near surface Argo observations was used).

NCEP/NCAR uses global T62 Gaussian grid with 192 longitude points with 1.875° (on average approximately 55 km in the study area) intervals and 94 latitude points with approximately 1.9° (211 km) spacing in the study area (latitude grid is not equally spaced). ERA-Interim has regular $1.5° \times 1.5°$ (on average approximately 44 km $\times$ 167 km on the study area) global grid. The Lagrangian forcings were picked up along the floats path by interpolating the forcing field to the halfway point between consecutive surfacings for the time period the float remained below the surface. This was taken to be as Lagrangian approach as it was possible to achieve with the data available. One could also calculate the float velocity and by assuming straight path and constant velocity it would be possible to have an individual point for each individual time step. It was assumed that this kind of a procedure would not increase the accuracy as the float's path is certainly not a straight line between the two surfacing points and as the distance between the surfacing points was so small that the atmospheric variability was assumed to be negligible. Eulerian forcings were calculated by interpolating the forcing fields to the float's median position.

Naturally neither of the atmospheric models is perfect and it is shown in Renfrew et al. (2002) that especially in NCEP/NCAR sensible and latent heat fluxes are overestimated. Also a more recent study (Latarius and Quadfasel, 2010) found large differences between forcings and after applying corrections to NCEP/NCAR (see Renfrew et al. (2002)) the agreement between data sets was much stronger. In this study, however, this correction was not used as the correction did not improve all the results. Furthermore, Renfrew et al. (2002) suggested the corrections in the beginning of 2002 and after that the NCEP/NCAR model version has changed and it is unclear how well the correction would be presently work. Also nudging to the surface salinities was tested, but it often lead to strong convection and too strong salinity increase at mid-depths, which was not seen in the observations. This was probably due to high near surface salinities in the data, which were introduced by dynamically controlled eddies. Nudging to surface salinities then lead to basically artificial input of salt, which easily enhanced the convection.

Chapter 3

Results and Discussion

The first part of this section focuses on the Argo data and relates observations from the three individual floats to earlier observations. After the observed conditions in the Greenland Sea are reviewed the analysis of the model results is presented. This analysis focuses on the effect of the atmospheric forcing data set and on the differences between Eulerian and Lagrangian approaches. In addition the performance of the different mixing parameterizations is analyzed. It will be shown that the convection during winter 2010-11 qualifies as mixed layer deepening according to the criteria of Ronski and Budeus (2005). Another main result is that the atmospheric forcing affects much more on the results quantitatively, than actual mixing scheme which has been chosen, although some scheme might be theoretically better justified.

Part of the statistical analysis, i.e. detecting changes in salinity, are done with the Student's t-test. The output of the test is probability (p-value) for the null hypothesis holding true. The null hypothesis (in this study) is that the means of two sample distributions come from same distribution. The main assumption which is required to hold before the test can be done is that the underlying distribution should follow normal distribution. This normality assumption was in turn tested with Shapiro-Wilk test (Shapiro and Wilk, 1965) which showed that it can be considered to hold true in the layers where this test was used.

This study includes observations from three floats and model runs with three mixing scenarios and two forcing data set which add to quite large number of results. That is why often only examples, usually from float 6900801, are shown. However, similar

figures for the other two floats can be found from the appendix B in case they are not shown in this chapter.

3.1 Observations

Background for the observations used in this study are reviewed in section 2.3. In this section the winter convection is discussed based on the data from three Argo floats (see Table 2.1), which operated in the Greenland Sea during the winter 2010-2011. Figure 2.1 shows the surface positions of these floats. As seen from the map, central Greenland Sea (Greenland Basin) is covered fairly well, but occasionally floats have been drifting also near Greenland shelf where the East Greenland Current (EGC) brings freshwater and ice from the Arctic towards south. At this region also the recirculating branch of Atlantic Water (RAW) flows southward as a part of EGC. Both water masses can be identified from their properties, such as temperature and salinity anomalies. RAW is relatively warm and saline while the arctic origin water in the EGC area is relatively fresh. In addition relatively fresh surface water is found all over the Greenland Sea during the summer.

Absolute Salinity–Conservative Temperature diagrams (IOC et al., 2010) below 500 db for all of the floats are shown in Figure 3.1 and different profiles together with the surface positions from the float 6900801 are shown in Figure 3.2 (see Figures B.1 and B.1 for profiles from the two other floats). As seen from the Figure 3.2e the float 6900801 drifted from northwestern corner of the Greenland Basin towards southeast during the fall and returned then back to northeast during the winter. The properties in the upper water column were quite similar until the start of the convection, but in the southeast the waters below 1500 db were more saline, cooler and consequently denser than in the area from where the float originated. The profiles from float 6900802 show evidence of cold advection below 1000 db before start of the convection phase and profiles from the float 6900811 show effect of advection of the Atlantic Water (in the upper water column) during the same time. Finally during the spring and summer the float 6900801 drifted towards the center of the Greenland Basin, while the two other floats ended up to the northwestern part of the Greenland Basin.

Previously Ronski and Budeus (2005) presented criteria for determining the convection type in the Greenland Sea. Table 3.1 is reproduced from their paper (see Table

2 in Ronski and Budeus (2005)) with the changes between summers 2010-2011. The salinity, potential temperature and potential density changes at mid-depths are relatively clear. Salinity and potential density increased while potential temperature was unchanged or decreased until the base of the winter mixed layer. This evolution can be seen as a rightward movement of the profiles in the Absolute Salinity–Conservative Temperature space (Figure 3.1). Movement is maybe the clearest with the float 6900801. It should be noted that floats 6900801 and 6900802 measured some profiles where the convection has reached more than 2000 db. These profiles might, however, be measured in the core of sub-mesoscale coherent vortices (Gascard et al., 2002) and thus not be a good indicator of true convection depth (see also discussion in section 1.1.1). Furthermore, Budeus and Ronski (2009) showed that the depth of the interface between upper and lower layer changes troughout the year and there is no strong increase during the winter. In this study the depth of the interface was 1600-1950 db before the winter convection and remained between these depths also after the winter (except individual profiles showing homogeneous conditions up to 2000 db). The depth of the interface seems to be largely dependent on the location as there are large differences between the consequent profiles. Interface lays at deepest depth from the central to the northwestern Greenland Basin while in the south and east the interface is found at clearly shallower depths.

Stability was analyzed based on buoyancy frequency. With the float 6900802 there is no change, but with the two other floats a clear decrease below 1500 db can be seen. This could indicate that during the previous winter(s) convection had been of the mixed layer deepening -type and thus stability had been small and rather homogeneous (except the deepest layer) before winter 2010-2011. The decrease in stability seen in the deepest part of the measurements indicates the deepening of the interface which is probably due to the change in location rather than due to convection. Small fluctuations were analyzed based on standard deviation of the different profiles at mid-depths (not shown). Significant change, indicating decrease in fluctuations, was found only in part of the profiles.

The results shown in Table 3.1 and Figure 3.2 clearly indicate that the winter 2010-11 was a winter with mixed layer deepening as presented in the Ronski and Budeus (2005) criteria. This in turn means that one would expect the turbulence parameterizations to work well as the counter gradient fluxes (main weakness of the 1-D parameterizations) are known to be small in this convection type (Akitomo, 2011).

Table 3.1: Criteria for the two ventilation schemes for Greenland Sea. Reproduced from Ronski and Budeus (2005) with additional information on the differences between the profiles before and after winter 2010-2011.

Modified Parameter	Winter With Mixed Layer Deepening	Winter With Plume Convection	Winter 2010-2011
Small-scale **fluctuations**, e.g., in the temperature profile	decrease	**increase**	no signal
Density	**increase**	decrease	**increase**
Stability	**decrease**	increase	decrease in deepest layer
Temperature and **Salinity**	increase or **decrease**	**decrease**	**increase** in salinity and slight **decrease** in temperature
Ice formation as possible forcing component	no	yes	no

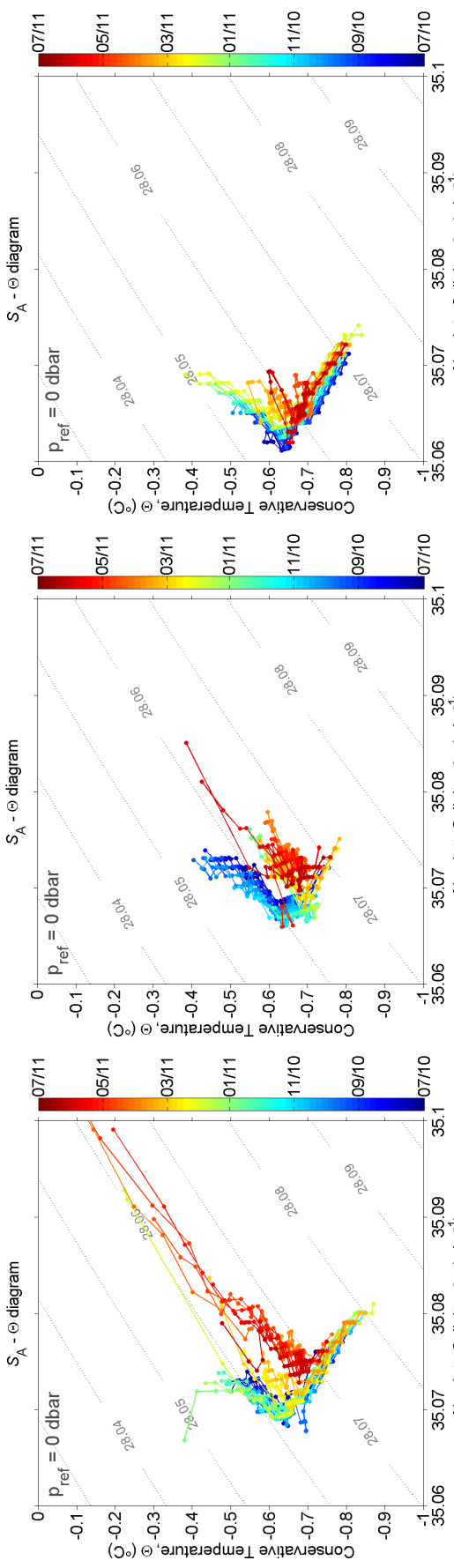

(a) float 6900801 (b) float 6900802 (c) float 6900811

Figure 3.1: Absolute Salinity–Conservative Temperature diagrams for observations below 500 db. Potential density (referenced to surface) contours are overlaid with gray lines. Color scale denotes the time, colorbar labels are given in [mm/yy] format.

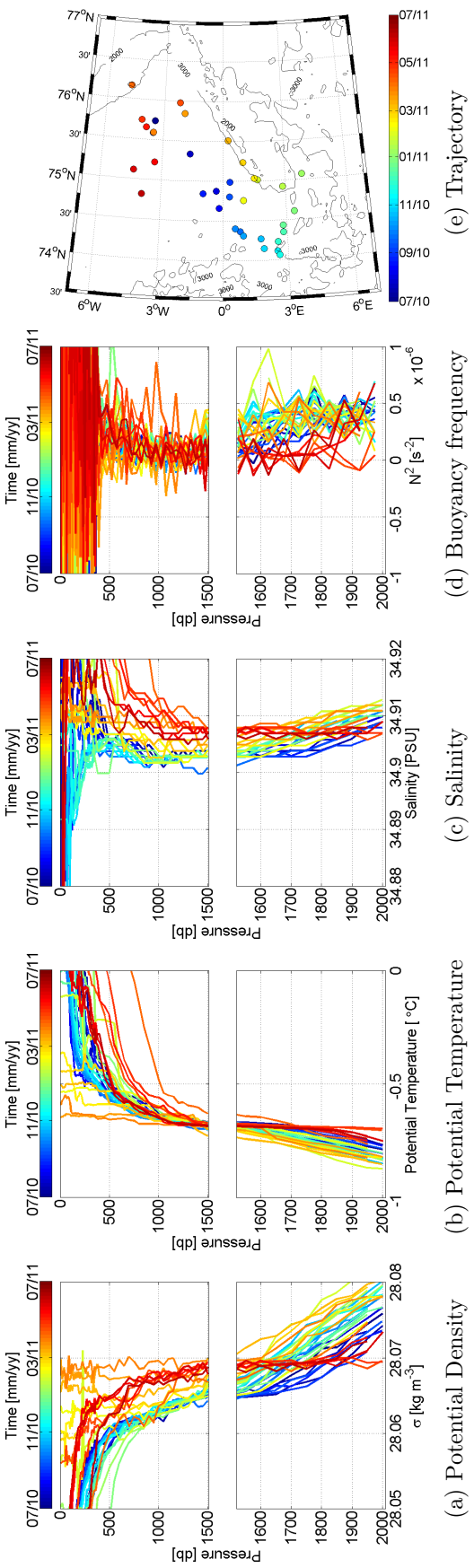

(a) Potential Density (b) Potential Temperature (c) Salinity (d) Buoyancy frequency (e) Trajectory

Figure 3.2: Different profiles measured by float 6900801 between July 2010–July 2011. The upper panel shows the properties between 0–1500 db while the lower panel is zoomed in the depths between 1500–2000 db. Figure 3.2e shows the floats surface positions.

3.2 Model results

In this section model results are compared with observations. Important tool in this kind of an analysis are Taylor diagrams (Taylor, 2001), which combine all the important statistical information between the model and observation. These statistics are correlation, root mean square difference (RMSD) and standard deviation. Correlation coefficient indicates whether the model is able to catch the observed patterns in time or space. The RMSD describes how well the model can predict the observed values quantitatively. The standard deviation indicates the variation in the timeseries. By comparing the modelled and observed standard deviations one can see if the model catches the observed deviation. It should be noted that RMSD contours in Taylor diagrams are not labeled as standard deviation contours have the same spacing and range (first standard deviation contour corresponds to the first RMSD value). Cumulative fluxes of heat and freshwater are used instead of actual fluxes in this section because cumulative values can be calculated from the observations.

3.2.1 Atmospheric forcing

Since the Argo floats are not stationary, but semi-Lagrangian by their nature, it would be reasonable to pick the atmospheric forcing along the path of the float. However, it is questionable if this procedure increases the accuracy of the results, especially since the grid size of the atmospheric data and the size of atmospheric phenomena are relatively large compared to the float trajectories. NCEP/NCAR grid cells are on average approximately 55 km $\times$ 211 km wide in the study area while ERA-Interim grid cells are on average approximately 44 km $\times$ 167 km wide on the study area.

Figure 3.3 shows the floats' surface positions on the NCEP/NCAR and ERA-Interim grids. It can be clearly seen that the float 6900802 (green) has the most confined trajectory as over 90% of the surface positions are inside two grid cells in NCEP/NCAR and three cells in ERA-Interim grid. On the other hand floats 6900801 (yellow) and 698011 (red) have covered much larger area and the surface positions are rather equally spaced over 7 NCEP/NCAR and 10 ERA-Interim grid cells. Since the forcings are picked up by interpolating the fields to the surface positions the variability can not be straight interpreted from the number of grid cells as also neighbouring cells affect the result. However, if we assume that the atmospheric variability between the grid cells

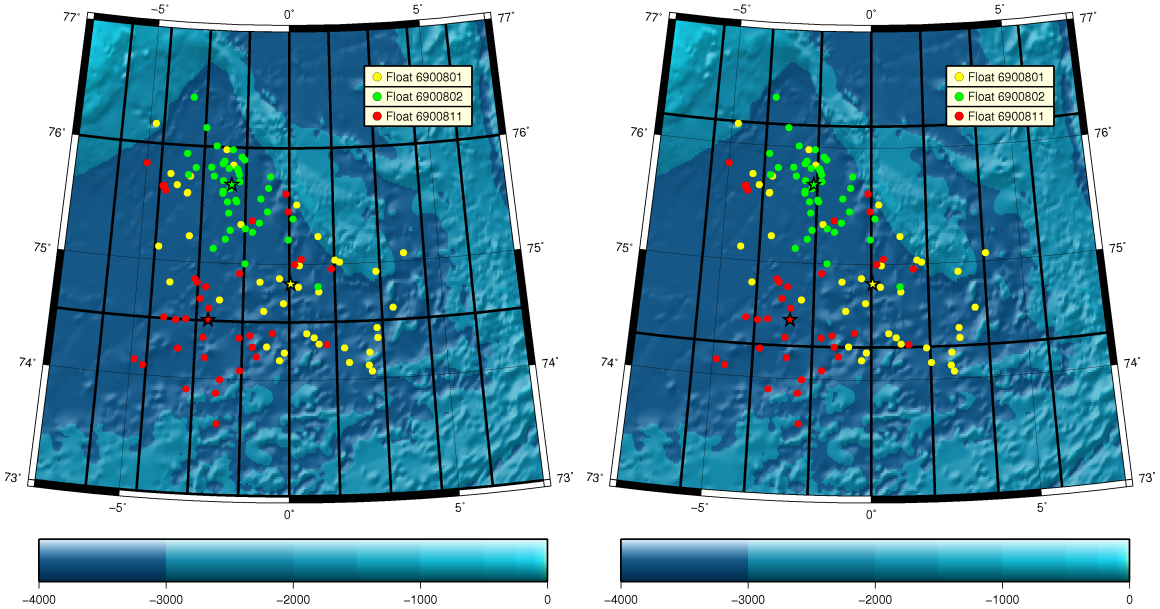

(a) ERA-Interim grid (b) NCEP/NCAR grid

Figure 3.3: Floats' surface positions on ERA-Interim and NCEP/NCAR grids. Black lines denote the grid cell borders. Stars indicate the median position of the float (colors are the same as in the legend). These images were created with Generic Mapping Tools (GMT), available from `gmt.soest.hawaii.edu`.

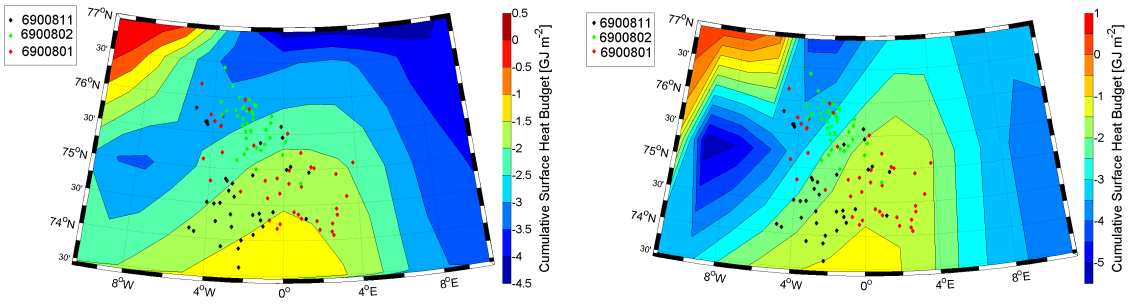

(a) ERA-Interim heat budget (b) NCEP/NCAR heat budget

Figure 3.4: Map of cumulative atmospheric heat fluxes from the beginning of July 2010 to the end of June 2011, with both ERA-Interim and NCEP/NCAR forcings

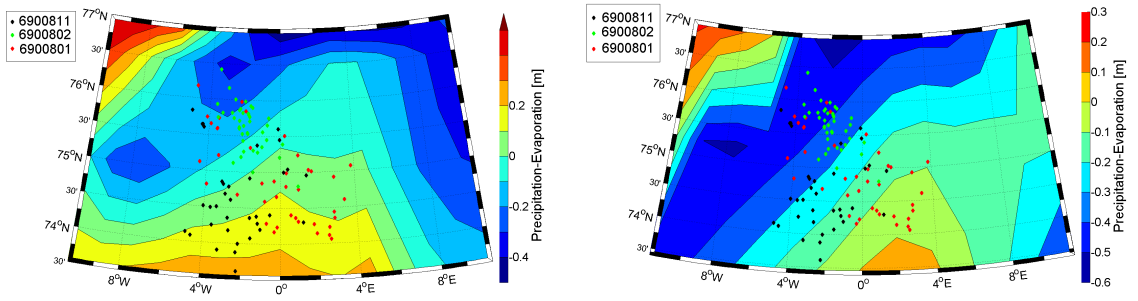

(a) ERA-Interim freshwater budget (b) NCEP/NCAR freshwater budget

Figure 3.5: Map of cumulative atmospheric freshwater fluxes from the beginning of July 2010 to the end of June 2011, with both ERA-Interim and NCEP/NCAR forcings

is equal over the whole study area, we can expect to have smaller variability between the forcings picked up along the float's trajectory and median position with the float 6900802 than the other two floats. Since the size of weather patterns is usually in order of 1000 km it is again likely that the difference between atmospheric fluxes in median and actual positions will be relatively small. Maps of the cumulative fluxes are shown in Figures 3.4 and 3.5. Some patterns in atmospheric heat and freswater flux (precipitation-evaporation) are present in both data sets. Evaporation exceeds the precipitation in the western part of the Greenland Sea, over the EGC, most likely in the area where RAW is present. Closer to the Greenland coast (in ice covered region) precipitation is larger than evaporation. Cumulative heat flux has a similar pattern, being the most negative over the EGC. There are also clear differences between the data sets. Both heat and freshwater fluxes in NCEP/NCAR data are more negative than in ERA-Interim forcing and also the area of freshwater loss in the western part of the Greenland Sea extends further south in NCEP/NCAR than in ERA-Interim data. This is a consequence of the NCEP/NCAR grid size.

Figures 3.6–3.8 show cumulative fluxes of heat and freshwater with Taylor diagrams for individual floats with the Eulerian and Lagrangian approaches. Corresponding surface momentum fluxes are shown in Figure 3.9. The heat content of the measured water column (0–2000 db) was calculated from the data with the following equation:

$$H(t) = \int_Z^0 \rho^0(z,t) \cdot h^0(z,t) dz \tag{3.1}$$

where h^0 is the potential enthalpy and ρ^0 is the potential density. Potential enthalpy is scaled Conservative Temperature (IOC et al., 2010; IAPWS, 2008) and it is defined as $h^0 = c_p^0 \cdot \Theta_C$, where Θ_C is Conservative Temperature and c_p^0 is an arbitrary scaling

factor designed to be close to the average heat capacity of surface seawater so that the difference between Conservative Temperature and potential temperature will be small (by definition $c_p^0 = 3991.86795711963$ J kg^{-1} K^{-1}) (IOC et al., 2010; IAPWS, 2008). Cumulative heat flux from the beginning of the measurement period is then the change in heat content, $\Delta H(t) = H(t) - H(1)$. Freshwater content in meters was calculated from Absolute Salinity [kg kg^{-1}], S_A, seawater density, ρ and freshwater density ρ_{fw}

$$F(t) = \int_Z^0 \frac{\rho(z,t)}{\rho_{fw}(z,t)} \cdot [1 - S_A] dz \tag{3.2}$$

The integral is taken over the measured water column (0–2000 db). The change in freshwater content relative to the beginning of the period, $\Delta F = F(t) - F(1)$, can then be taken as cumulative net precipitation and compared to the precipitation-evaporation from reanalyzes.

It can be clearly seen that the differences between the Lagrangian and Eulerian approach in freshwater fluxes are one order of magnitude smaller than the differences between NCEP/NCAR and ERA-Interim forcings. Figure 3.8 shows that the correlation between the freshwater flux calculated from observations and given by reanalyzes was very poor. The ERA-Interim, however, catches the absolute values much better than the NCEP/NCAR forcing in each case. In addition Eulerian and Lagrangian values clearly differ and Lagrangian seems to be closer to the observations. The differences between observations and reanalyzes can be mostly explained with the advection.

The forcing data set induces the largest differences also in heat fluxes. By analyzing the Taylor diagrams in the Figure 3.7 one can see that the heat flux correlation is solely determined by the forcing data set. The choose between Eulerian and Lagrangian approach has a negligible effect to the correlation, which indicates that the changes in the cumulative heat fluxes are similar in both cases. This is reasonable as the solar radiation, which is an integral part of the heat flux, has strong seasonal variability. The differences in heat fluxes are then caused by the weather patterns which affect also the precipitation-evaporation. Although the effects of the different approaches were negligible for correlation there are clear differences in RMSD and standard deviation. In the case of floats 6900802 and 6900811 the Lagrangian approach produces smaller RMSD and also standard deviation is closer to the observed one. In the case of float 6900801 the July 2010–June 2011 period (Figure 3.7a) shows poor correlation and Eulerian approach seems to produce smaller RMSD and standard deviation closer to

the observed values compared to the Lagrangian one. The end of this period is, however, affected by the advection and by removing the advective period and comparing the July 2010–April 2011 period (Figure 3.7b) one can see that the difference between the two approaches is very small. This could be explained by the large area which the float 6900801 covered during this period. The cumulative flux over this path was close to the cumulative flux in the median location as the float did not spend more time in one place than in another. Although float 6900811 also covered a large area the trajectory was more confined in the southern part of the Greenland Sea close to sharp gradient and thus even small changes in the location had a large effect to the results. What is interesting is the clear difference between the approaches in the case of float 6900802, which had the most confined trajectory of all the floats. This can be explained by examining the map in the Figure 3.4. The float 6900802 spent most of the time close to the sharp gradient similarly to the float 6900811 and that is likely to be the reason why the difference is clear despite the confined trajectory.

In general the differences between the Lagrangian and Eulerian approaches are larger in NCEP/NCAR data than in ERA-Interim data. One possible explanation is the larger grid size of the NCEP/NCAR data. The larger grid produces sharper gradients and thus larger differences. On average the differences are smaller during the summer than in winter, which is due to larger storm activity during winter. The effect of just one storm is, however, relatively large. This is especially evident in the case of the float 6900801. By comparing the cumulative heat fluxes in Figures 3.6a and 3.6b one can see that at the beginning of April the Lagrangian forcing experiences still cooling while Eulerian forcing shows no such signal. In the end this leads to approximately 10 % difference in the heat budget. By comparing the wind stresses in Figures 3.9a and 3.9b a similar pattern can be seen. In Lagrangian case there is a strong storm at the beginning of the April while in the Eulerian case the same storm is almost invisible.

3.2.2 Effect of the atmospheric forcing

Although there are differences between the ERA-Interim and NCEP/NCAR forcings and with the Eulerian and Lagrangian approaches, it is unclear whether these differences are significant for the ocean. This significance was tested by running the GOTM model with $k - \epsilon$ mixing scenario with Eulerian and Lagrangian forcings. Also a test without freshwater forcing was carried out in order to quantify its importance.

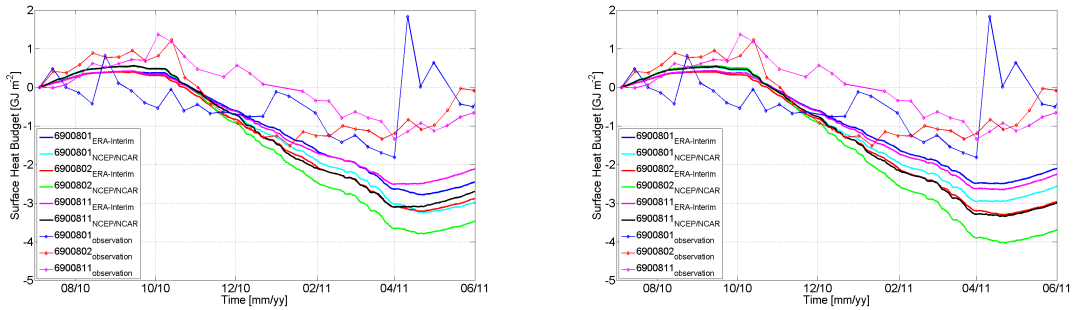

(a) Surface heat budget along float's path (b) Surface heat budget at float's median position

Figure 3.6: Cumulative surface heat budgets for all the floats using both Lagrangian and Eulerian approach. Integrated heat contents derived from the float data are shown with dotted curve.

Temperature and salinity timeseries for float 6900801 are shown in Figure 3.10 and corresponding Taylor diagrams are shown in Figures 3.11. In general modelled temperature correlates well with the observations near the surface, but the correlation decreases in deeper layers. Especially in the case of floats 6900801 and 6900802 there is virtually no correlation deeper down. 6900811 is an exception in the sense that the modelled temperature has some correlation (over 0.7) also in 500 db and 1500 db layers. The standard deviation of the model results is larger than the observed one in all cases, which indicates that also the forcing has large standard deviation. It should also be noted that difference between the approaches is not statistically significant at the surface layer (Student's T-test with 5 % confidence level). In contrast to temperature, salinity correlates better in the deeper layers than at the surface. Near the surface the modelled standard deviation is too small but in the deepers layers it is close to the observations. Differences in salinities between the two approaches are statistically significant in all layers except at 10 db with NCEP/NCAR forcing. This interesting difference between the temperature and salinity results is discussed in section 3.2.2.1.

In general the model results at the surface are too warm during summer and too cold during winter. NCEP/NCAR forcings produces the extremes. This could be explained with too shallow mixed layer, resulting from too small vertical mixing, in the model or with the effect of advection in the observations. Modelled vertical mixing in the surface layer is known to be too small since the wave mixing was not taken account in this study. This effect was neglected as it has little effect for the convection. The temperature difference in summer is most likely due to both effects. The shallow mixed layer could warm too much, but it is likely that also advection affects, as the

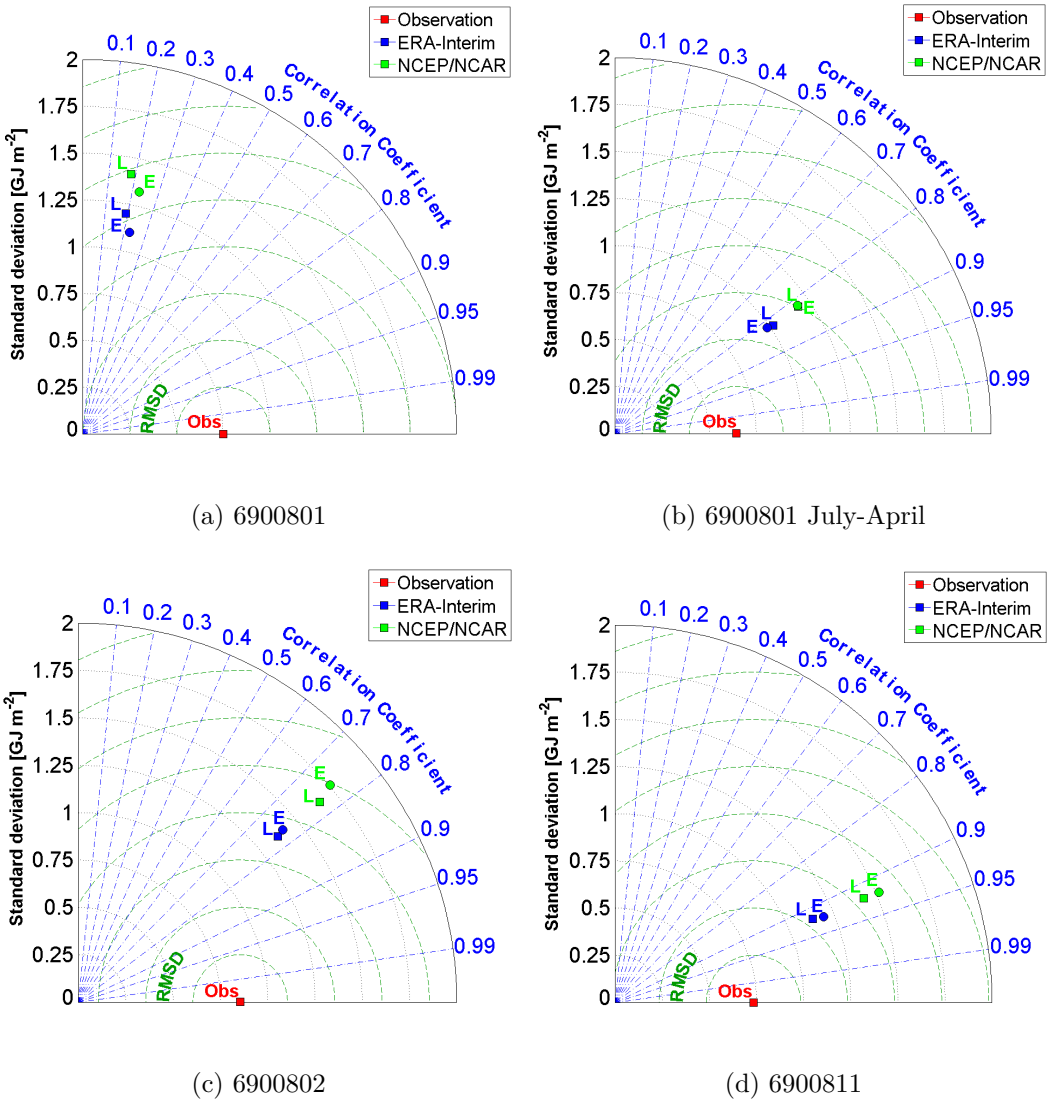

(a) 6900801

(b) 6900801 July-April

(c) 6900802

(d) 6900811

Figure 3.7: Taylor diagrams for cumulative surface heat budgets for all the floats using both Lagrangian (L) and Eulerian (E) approach for the period between July 2010–June 2011. Since the float 6900801 experiences a clear effect of advection after April 2011 (see Figure 3.6) also the period between July 2010–April 2011 is shown. Observations refers to the integrated heat contents derived from the float data. Colors refer to the forcing data set, red is NCEP/NCAR and magenta is ERA-Interim reanalysis. Symbols refer to the approach, box is for Lagrangian and circle is for Eulerian approach.

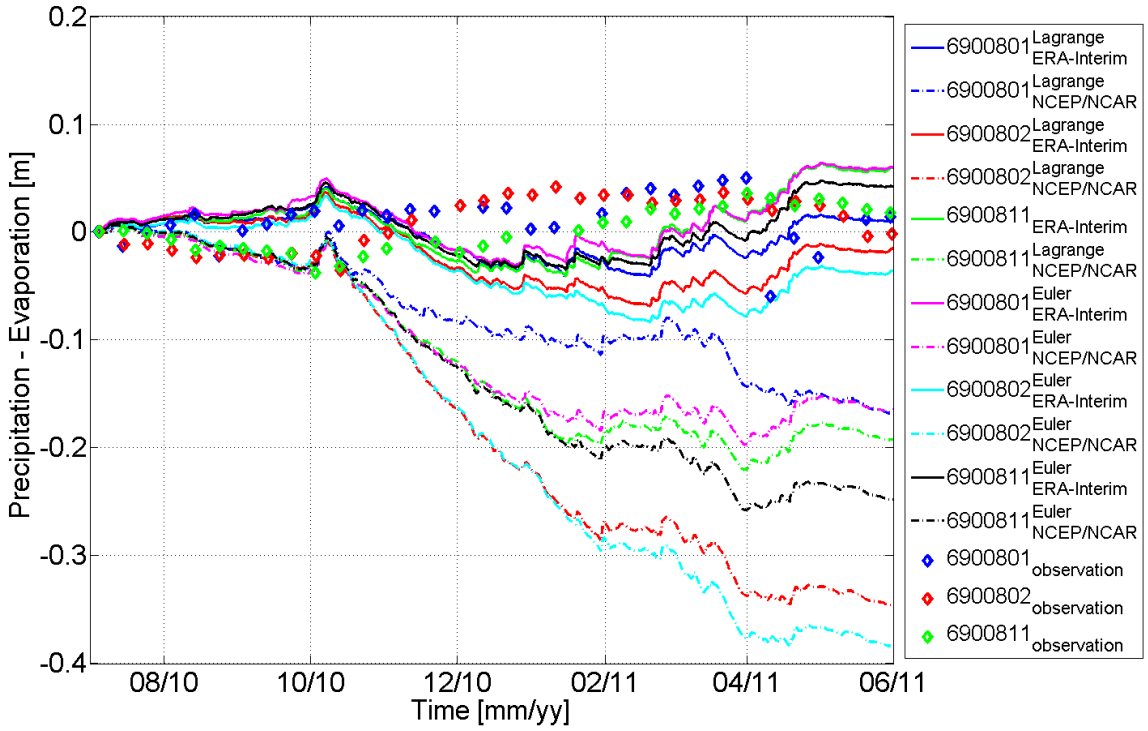

(a) Cumulative freshwater flux

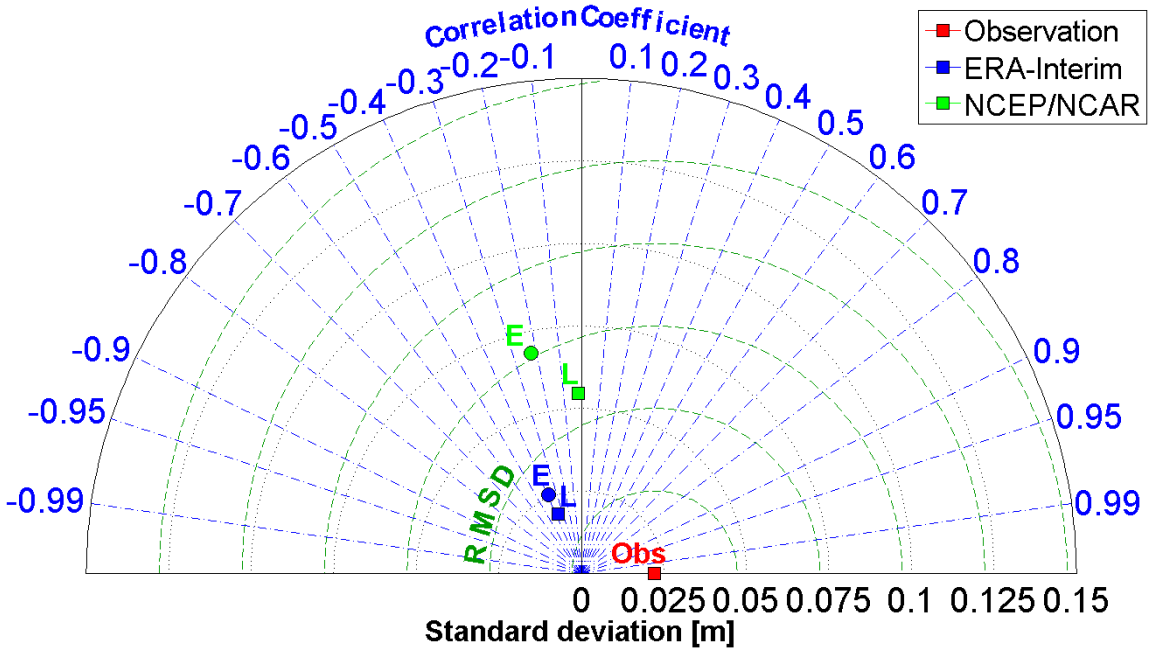

(b) Taylor diagram 6900801

Figure 3.8: Cumulative freshwater flux (precipitation-evaporation) for all the floats (a) and Taylor diagram for float 6900801 (b). ERA-Interim fluxes are marked with continuous line and NCEP/NCAR fluxes with dashed line. Freshwater forcing derived from observations is shown with diamonds. It can be clearly seen that the difference between Eulerian and Lagrangian approaches is basically one order of magnitude smaller than the difference between data sets.

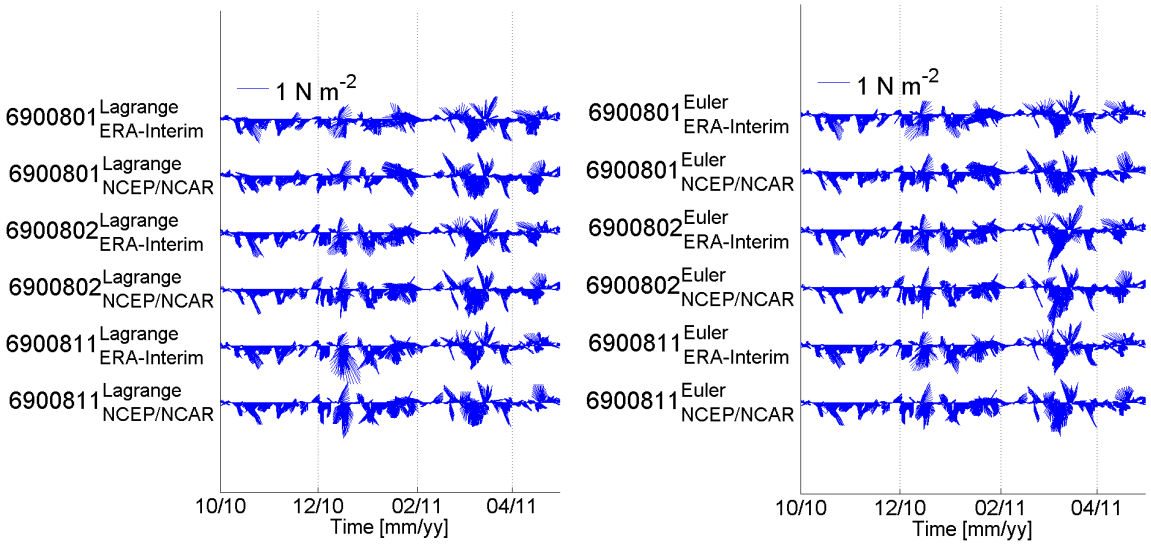

(a) Wind stresses along floats' path (b) Wind stresses at floats' median position

Figure 3.9: Surface wind stresses for all the floats using both Lagrangian and Eulerian approach. Time period is between 1st of October and 1st of May (7 months). During this period over 60 % of the winds were between $-180°$ and $0°$.

modelled salinity at the surface layer is higher than observed one during summer. This is a signal of cold low salinity water advection from the Arctic. Observations also show occasional warming events during the winter (e.g in January) which are most likely due to advection of the warm Recirculating Atlantic Water from recirculating branch of West Spitsbergen Current. The cold bias in model during the winter is, however, likely to be due to too cold forcing data sets.

3.2.2.1 Temperature and salinity evolution

As noted in the previous section there is a clear difference between temperature and salinity response. Modelled temperature matches better with the observations near the surface while modelled salinity is closer to the observations at the deeper layers. Salinity time-series, averaged over 1200-1700 db layer, and corresponding Taylor diagrams are shown in Figure 3.12. At this layer salinity increased by $0.001 - 0.005$ g kg^{-1} PSU and increase decreased towards the bottom depending also of the float (i.e. location) in question. The salinity increase is abrupt and linked to the convection which mixes the more saline waters from above to this layer. Two-sample Student's T-test test was applied to the data in order to check whether or not the mean salinity after and before the sudden increase comes from the same distribution. The null

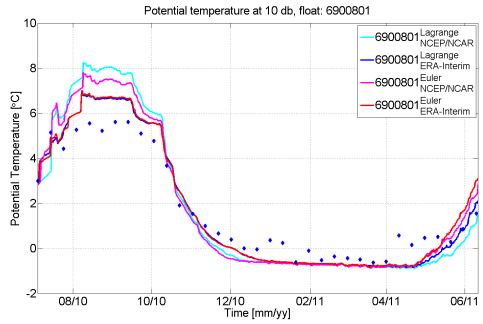

(a) Potential temperature at 10 db

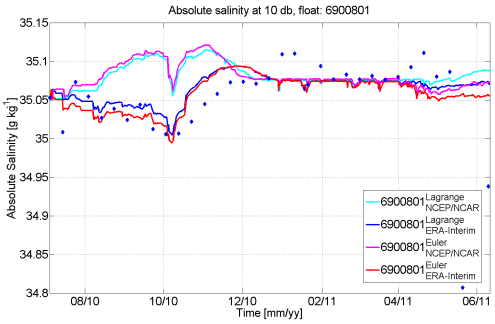

(b) Absolute Salinity at 10 db

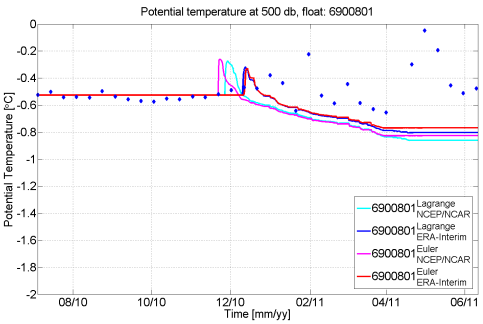

(c) Potential temperature at 500 db

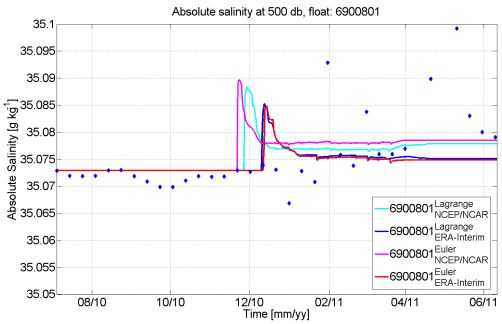

(d) Absolute Salinity at 500 db

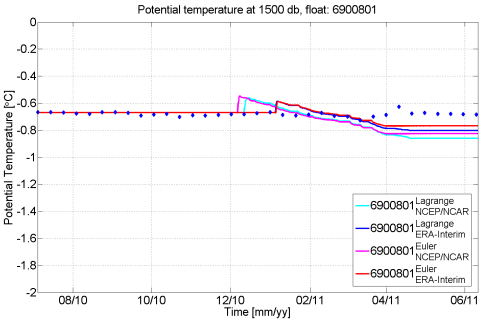

(e) Potential temperature at 1500 db

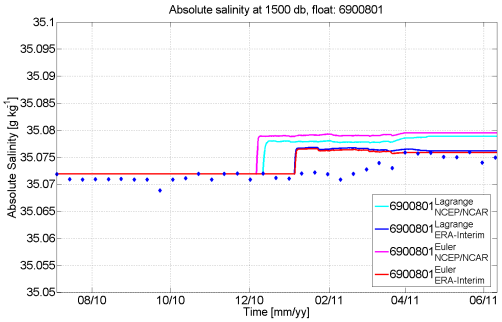

(f) Absolute Salinity at 1500 db

Figure 3.10: Potential temperature and Absolute Salinity timeseries at different pressure levels for float 6900801.

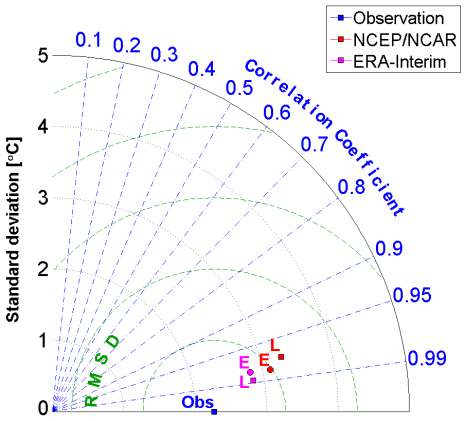

(a) Potential temperature at 10 db

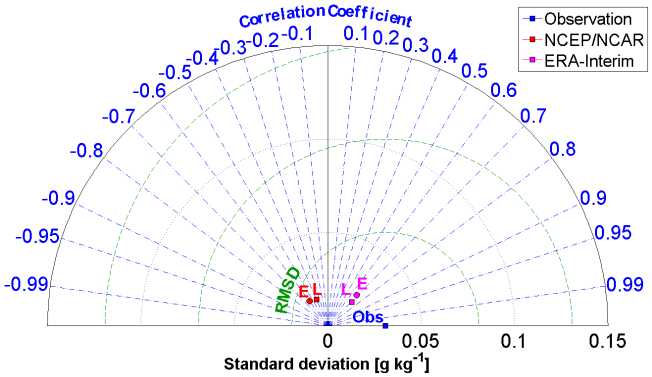

(b) Absolute Salinity at 10 db

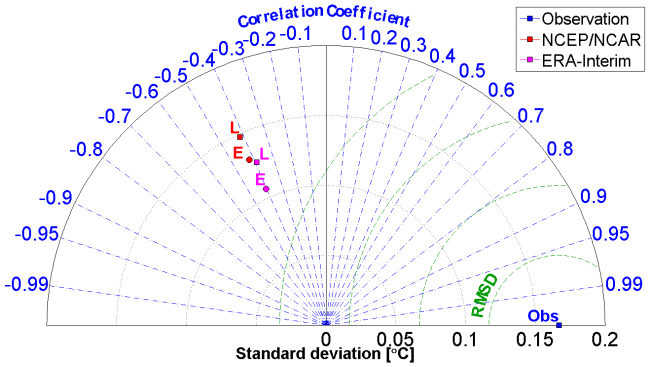

(c) Potential temperature at 500 db

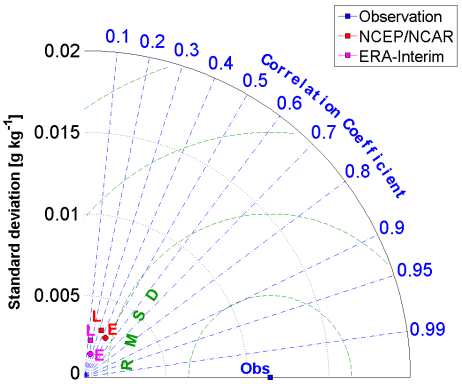

(d) Absolute Salinity at 500 db

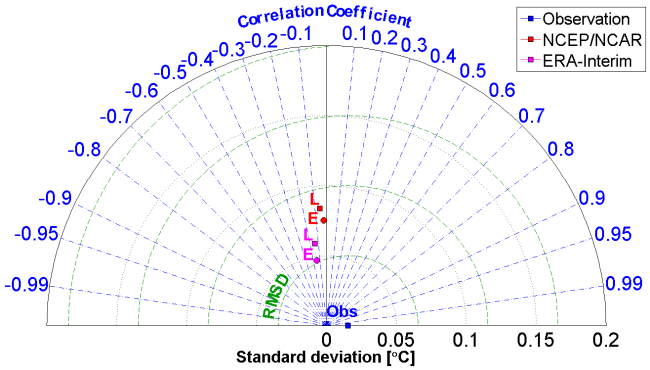

(e) Potential temperature at 1500 db

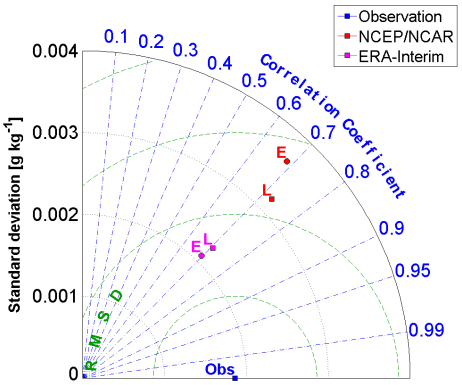

(f) Absolute Salinity at 1500 db

Figure 3.11: The Taylor diagrams corresponding to the potential temperature and Absolute Salinity timeseries shown in Figure 3.10 for float 6900801.

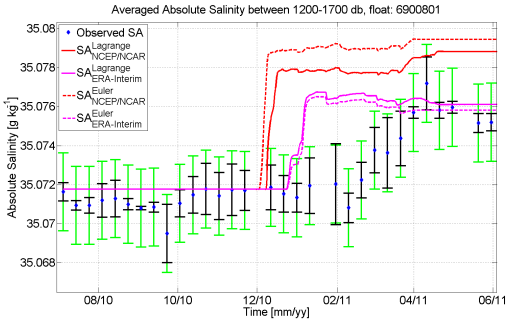

(a) 6900801

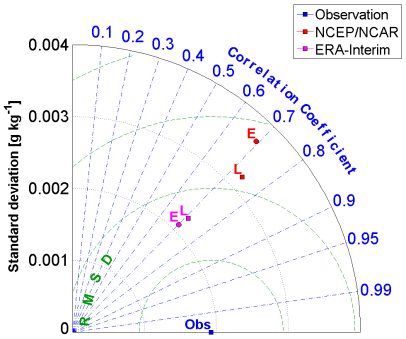

(b) Taylor diagram

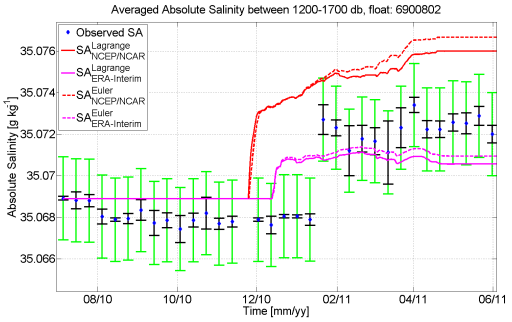

(c) 6900802

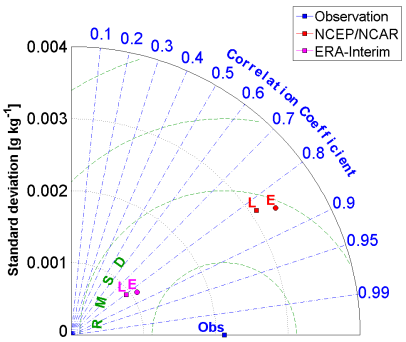

(d) Taylor diagram

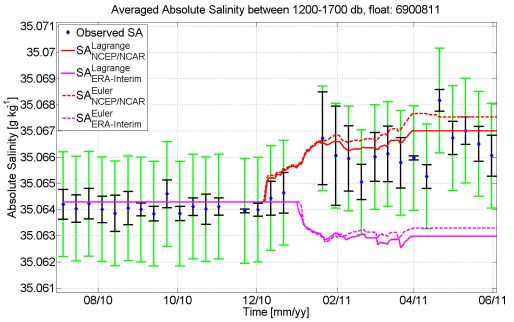

(e) 6900811

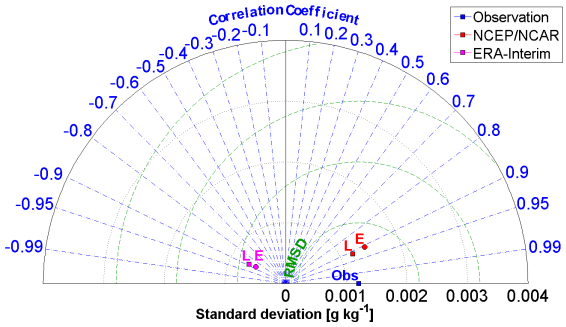

(f) Taylor diagram

Figure 3.12: Observed and modelled salinity (given in Absolute Salinity (g/kg)) averaged over 1200-1700 db and the corresponding Taylor diagrams. In timeseries plots black bars give the standard deviation and green bars give the measurement error (±0.002 g/kg).

hypothesis for the test was that the samples are from the same distribution. The test resulted to p values below 0.001 and the null hypothesis can be rejected at 0.1 % confidence level, so the change is significant.

The observed salinity increase could be of course due to horizontal advection in this layer and not due to convective mixing. However, since also the model results show increasing salinity at mid-depths, although there is no advection in the model, vertical mixing has to be main the mechanism behind the salinity increase. The observed and modelled (with ERA-Interim surface forcing) profiles of potential temperature and salinity during the active convection are shown in Figure 3.13. It can be seen how the relatively high salinity RAW layer below the surface mixes to the surrounding layer as the convection moves on. First the temperature rises in the waters below the RAW layer, but soon the surface cooling takes over and at the end the water column is colder than initially. Convection decreases the salinity in the RAW layer and increases it in deeper layers. In the end the salinity of the water column is close to the average of the RAW and surrounding layers.

As such this observed and modelled salinity increase seems to be largely independent of the surface freshwater forcing. The significance of the surface forcing compared to the importance of the RAW layer was tested by running the model with and without surface freshwater forcing (using $k - \epsilon$ mixing parameterization). Figure 3.14 shows the ratio between the results for floats 6900801 and 6900802 at 1500 db layer. This ratio shows basically how much of the modelled salinity increase can be explained with the RAW layer an how much is explained by the surface freshwater forcing. The RAW layer has the strongest effect with ERA-Interim forcing in all cases, whereas the results with NCEP/NCAR forcing indicate that RAW is the more important component only in the case of the float 6900801. Since ERA-Interim results are closer to the observations they can be taken to indicate the real situation. The differences between the two floats are still quite large. This can be explained by the much larger area the float 6900801 covered compared to the float 6900802. It might be that the difference indicates the real variability which exists in the importance of surface freshwater flux for the mid-depth salinity increase. The maps of cumulative freshwater fluxes shown in Figure 3.5 indicate that this could be actually the case as the variability is quite large over the Greenland Sea. Since further estimates are difficult to make the final conclusion remains that the effect of surface freshwater flux is roughly between 0–40 %. If the RAW layer is renewed by advection it is likely to have larger effect than if it is not renewed.

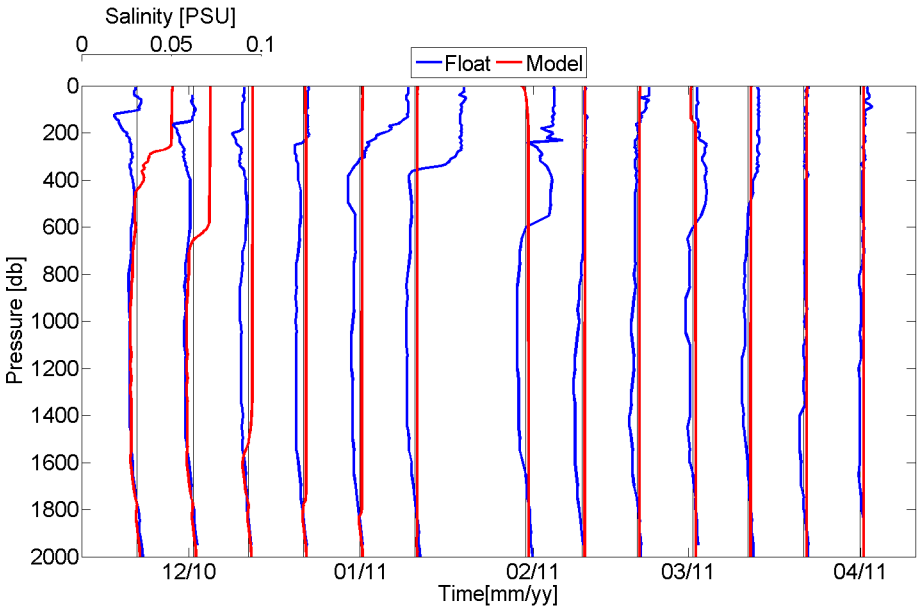

(a) Salinity

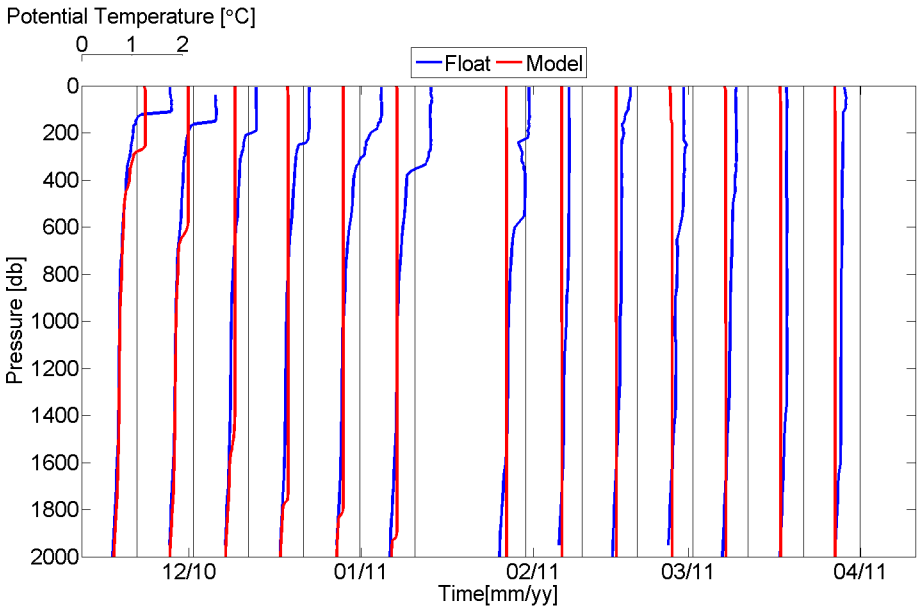

(b) Potential temperature

Figure 3.13: Salinity and potential temperature profiles during active convection for float 6900801. Temperature and salinity scales are given in the upper left corner of the plots. The profiles are relative to the mean temperature (−0.189) and mean salinity (34.908) of the initial profile, which are plotted to the figure with black line. It can be seen how the warmer and more saline RAW layer mixes down. First the temperature rise in the waters below, but soon the surface cooling takes over and at the end the water column is cooler than initially. Convection decreases the salinity in the RAW layer and increases it in deeper layers. In the end the salinity of the water column is close to the average of the RAW and surrounding layers.

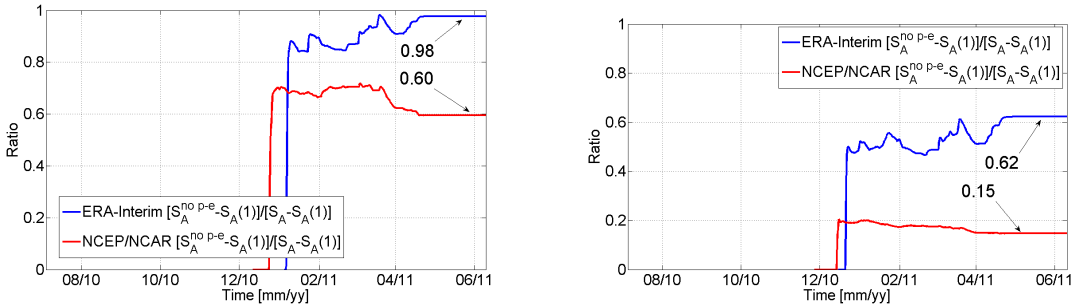

(a) 6900801 (b) 6900802

Figure 3.14: Importance of the surface freshwater flux for salinity increase at 1500 db. The ratio indicates how much of the salinity increase at 1500 db can be explained by the RAW layer. 1-ratio must then be the contribution by the surface freshwater flux.

The float 6900811 is an exception to the two other floats. There is a very small signal of RAW present in the initial salinity profile and it is not enough to increase the salinity in the model runs. The NCEP/NCAR results show increasing salinity only because the evaporation increases the salinity at the surface. Although there is no effect of initial condition in the RAW the float 6900811 however drifts in the area where RAW changes the conditions during the start of the convection phase. Then a lid of higher salinity water forms at roughly 300-500 db layer and the convection mixes this lid with the deeper layer and increases the salinity, although the float drifts away from this area. This explanation is also backed up with the modelled temperature. These results correlate best with the observed conditions in case of the float 6900811. This is reasonable as the advection has only a small affect to the observed conditions and the surface cooling is transfered to the deeper layers. In the case of the other two floats the correlation is poor and the observed temperature increases or shows no clear signal at mid-depths although surface temperature is well captured by the model. The modelled temperature show also increase at the mid-depths when the convection begins as the warmer RAW mixes down. However, the surface cooling starts to dominate quite soon and at the end the model temperatures cool too much. This is partly due to absence of the RAW advection, but partly due to too cold forcings.

The conclusion from the results is that the increase of the mid-depth salinity and the poor correlation of salinity results at 500 db can be explained by the RAW influence. Similarly the poor correlation of temperatures below surface can be explained by the absence of RAW advection, which would provide compensating heat flux. Previously Budeus and Ronski (2009) as well as Latarius and Quadfasel (2010) suggested that

the salinity increase in mid-depths is due to Atlantic Water (AW) influence. The results shown in this section indicate that the RAW layer indeed has a strong role in determining the salinity and temperature evolution in the whole convective layer. However, in some occasions the atmospheric freshwater flux can also have significant impact. Especially NCEP/NCAR forcing produces unrealistic freshwater fluxes which in turn accelerate the convection process and convection reaches mid-depths some 10-20 days in advance compared to situation with no freshwater flux.

It is clear that forcing fields differ depending on whether one is using Eulerian or Lagrangian approach. The surface forcing suggests that the Lagrangian approach is indeed closer to the observed conditions. However, because of the strong effect of the forcing data set and RAW layer the model results are somewhat ambiguous. Consequently, it is hard to conclude whether the theoretically and intuitively more solid Lagrangian approach actually produces better results or whether some of the results happen to be better just by chance. If the grid size of the forcing data sets would be smaller and if forcing fields would be of better quality a more definitive answer could be given. ERA-Interim forcing, however, is clearly better than the NCEP/NCAR forcing. Both forcings, are too cold during the winter. This could be explained with the incorrect ice edge information in both models. The coarse resolution sets of course a limit to ice edge information. This can be rather crucial as the air temperature over ice-covered and ice-free ocean can easily differ by tens of degrees. However, as noted above, part of the low temperature bias in the model results can be explained by the RAW advection in the upper layer, which is not present in the model.

3.2.3 Effect of mixing schemes

The mixing schemes used in this study were $k - \epsilon$, Mellor-Yamada (MY) and KPP scenarios. As it was seen in the previous section the surface forcing has a strong effect in the results. The forcing data set affected most, but also the Eulerian and Lagrangian approaches produced clearly different outcomes. The model used in this study is driven only by surface forcing, which means that the integrated heat and freshwater content depends only on the surface forcing, while the distribution of heat and salt depends on parameterization. Because of this the mixing scheme is expected to effect mainly the timing of the mixed layer deepening and restratification. In this sense the mixing parameterizations affects the results qualitatively more than quantitatively.

Figure 3.15 shows Taylor diagrams of potential temperature and salinity timeseries for different depths. In general the differences appear to be smaller compared to the differences between Eulerian and Lagrangian approaches. Tables 3.2 and 3.3 show the results from two-sided Student's T-test for salinity and potential temperature. The null hypothesis was that the means come from same distribution and cases when it can be rejected at 5 % confidence level are written with bold font. It can be seen that most of the significant differences between the temperature results occur at 2000 db level. This is clearly related to the convection depth and the timing of convection. Salinity results show differences mainly at 500 db level, which results from the treatment of the RAW layer. Despite the small number of significantly differing cases the KPP parameterization seems to differ from the other two parameterizations most often. This is expected as the theory behind $k-\epsilon$ and MY parameterizations is rather similar, whereas KPP is based on different theory. However, in some cases MY and KPP seem to be close each other.

Although the differences in the whole time-series are rather similar in most cases the start of the convection differs quite remarkably. At every layer below the summer MLD the KPP parameterization produces convection earlier than the $k-\epsilon$ or MY parameterizations. For example with ERA-Interim forcing convection reaches 1500 db some 20 days earlier with KPP parameterization than with $k-\epsilon$ or MY parameterizations. With NCEP/NCAR forcing the difference is 7 days. The reason why the difference is much smaller with NCEP/NCAR could be the strong cooling which is driving the convection. In the NCEP/NCAR the cooling is so strong that the convection just cannot happen much faster, but with the lesser cooling in ERA-Interim forcing the KPP parameterization is capable of advancing the convection quite remarkably.

Effect of non-local flux The non-local flux term in KPP parameterization is capable of stabilizing the unstable boundary layer (Losch et al., 2006). It is expected that removing the term would enhance the convection if the non-local flux produces counter gradient transport. In this case the down gradient part and the non-local part would act against each other and the turbulent transport would be smaller. This non-local flux term depends on surface forcing and the depth of the mixed layer. The effect of the non-local fluxes was examined by turning the term off in the KPP parameterization. In both cases Lagrangian forcing was used. It is expected that if the counter gradient transport is important there would be again differences at the time the convection reaches the deeper layers. Figure 3.16 shows Taylor diagrams for the potential temperature timeseries at the depth of 2000 db for float 6900801. It can be

Table 3.2: Percentages from the two-sided Student's T-test for salinity. The null-hypothesis was that the means come from same distribution, the cases when null-hypothesis can be rejected (at 5 % confidence level) are marked with bold.

		6900801		6900802		6900811	
		N/N	ERA-Int.	N/N	ERA-Int.	N/N	ERA-Int.
10 db	$k-\epsilon$ - MY	0.962	0.949	**0.063**	0.612	**0.031**	0.821
	$k-\epsilon$ - KPP	**0**	0.360	0.314	0.840	**0.055**	**0.030**
	MY - KPP	**0**	0.398	**0.005**	0.775	0.969	**0.018**
500 db	$k-\epsilon$ - MY	0.937	0.897	0.9332	0.757	0.851	**0**
	$k-\epsilon$ - KPP	**0.092**	**0**	**0**	**0**	**0.022**	**0**
	MY - KPP	0.108	**0**	**0**	**0**	**0.012**	**0**
1000 db	$k-\epsilon$ - MY	0.990	0.939	0.978	0.9545	0.895	0.264
	$k-\epsilon$ - KPP	0.299	0.516	0.770	0.3874	**0.009**	0.912
	MY - KPP	0.304	0.568	0.748	0.4193	**0.006**	0.311
1500 db	$k-\epsilon$ - MY	0.892	0.857	0.938	0.948	0.894	0.261
	$k-\epsilon$ - KPP	0.430	**0.002**	0.467	0.255	0.945	0.327
	MY - KPP	0.514	**0.003**	0.515	0.227	**0.012**	0.865
2000 db	$k-\epsilon$ - MY	0.987	**0.030**	0.845	0.222	0.135	0.213
	$k-\epsilon$ - KPP	0.704	**0.001**	0.481	0.412	**0.001**	**0**
	MY - KPP	0.693	0.217	0.611	0.629	**0.087**	**0**

Table 3.3: Percentages from the two-sided Student's T-test for potential temperature. The null-hypothesis was that the means come from same distribution, the cases when null-hypothesis can be rejected (at 5 % confidence level) are marked with bold.

		6900801		6900802		6900811	
		N/N	ERA-Int.	N/N	ERA-Int.	N/N	ERA-Int.
10 db	$k-\epsilon$ - MY	0.664	0.516	0.924	0.591	0.236	0.844
	$k-\epsilon$ - KPP	**0.002**	0.959	0.258	0.470	0.292	0.452
	MY - KPP	**0.009**	0.490	0.224	0.845	0.027	0.574
500 db	$k-\epsilon$ - MY	0.956	0.918	0.993	0.969	0.989	0.977
	$k-\epsilon$ - KPP	0.679	0.320	0.871	0.810	0.793	0.812
	MY - KPP	0.719	0.373	0.864	0.841	0.804	0.833
1000 db	$k-\epsilon$ - MY	0.901	0.878	0.958	0.906	0.945	0.949
	$k-\epsilon$ - KPP	0.674	0.995	0.935	0.726	0.948	0.830
	MY - KPP	0.587	0.885	0.977	0.816	0.997	0.880
1500 db	$k-\epsilon$ - MY	0.923	0.884	0.937	0.872	0.910	0.917
	$k-\epsilon$ - KPP	0.807	0.164	0.983	0.774	0.670	0.760
	MY - KPP	0.883	0.127	0.954	0.899	0.755	0.840
2000 db	$k-\epsilon$ - MY	0.282	**0**	0.994	0.891	0.956	0.336
	$k-\epsilon$ - KPP	**0**	**0**	**0.031**	**0.002**	0.129	0.912
	MY - KPP	**0**	**0**	**0.032**	**0.041**	0.145	0.273

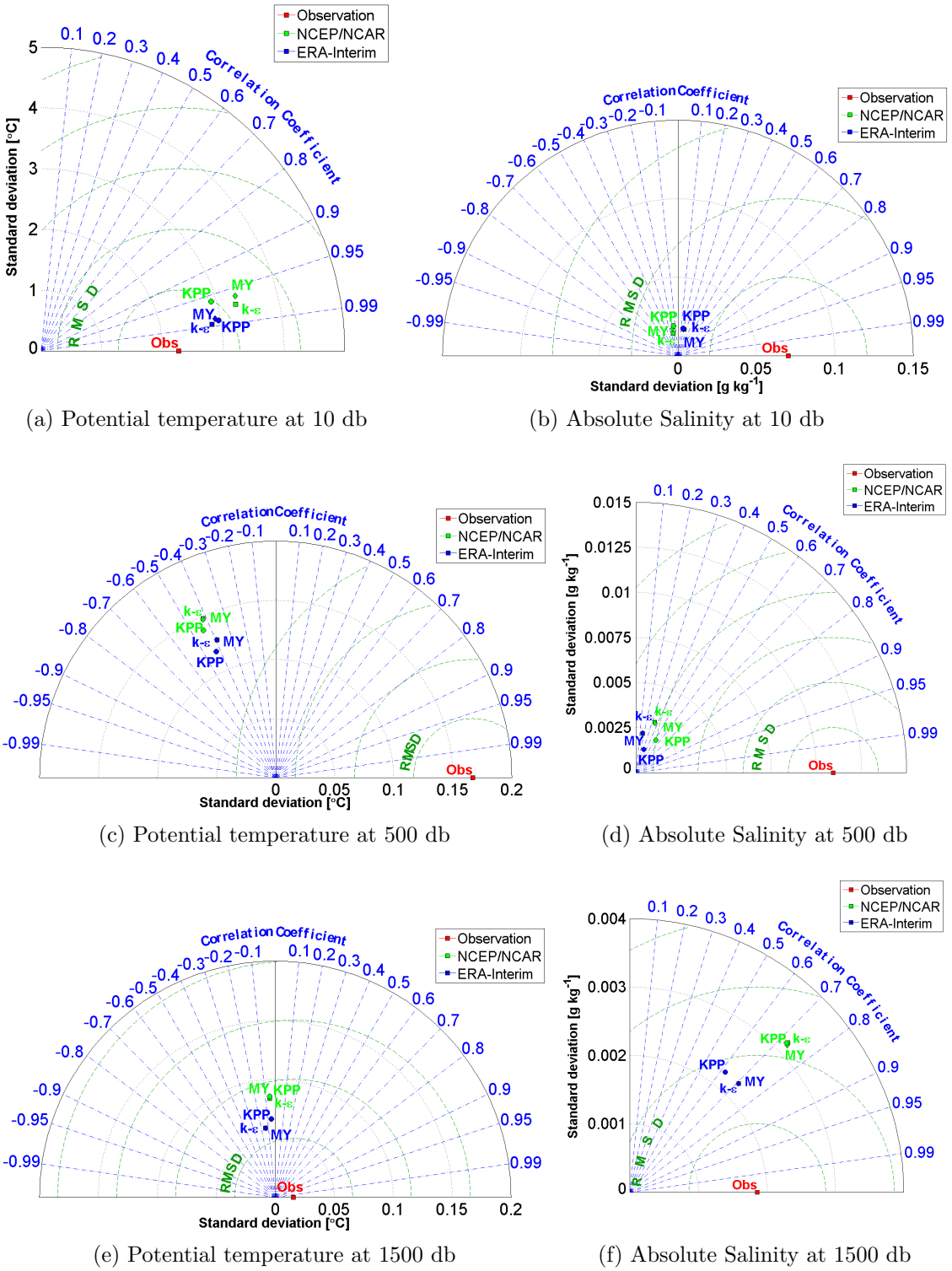

(a) Potential temperature at 10 db

(b) Absolute Salinity at 10 db

(c) Potential temperature at 500 db

(d) Absolute Salinity at 500 db

(e) Potential temperature at 1500 db

(f) Absolute Salinity at 1500 db

Figure 3.15: Taylor diagrams at different depths for potential temperature and Absolute Salinity, float 6900801. Different colors denote different forcings and different symbols denote different parameterizations.

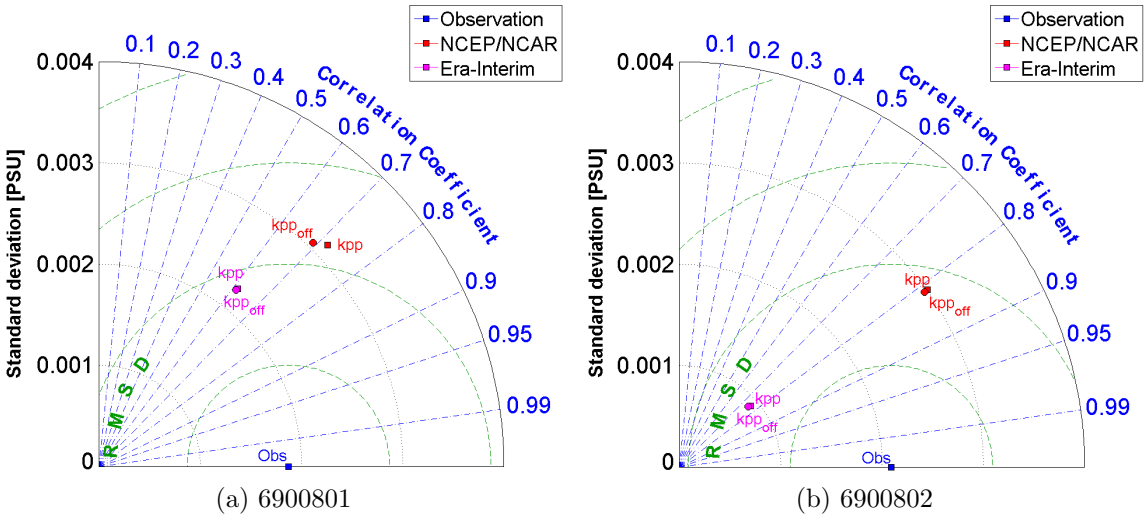

(a) 6900801 (b) 6900802

Figure 3.16: Taylor diagrams for salinity at 1500 db using KPP mixing scenario with non-local flux both on and off. Shown for floats 6900801 and 6900802

seen that the differences are small, but still clear, between the two cases. Removing the non-local effect enhances the convection below 1500 db which indicates that the counter-gradient fluxes are important only at the deepest layer. The small differences in general were expected as the convection was of mixed layer deepening type and Akitomo (2011) has shown that counter gradient transport arising from non-local fluxes is unimportant in this kind of convection.

3.3 Remarks on the reliability of the results

Since the time period of the runs was rather short (less than 1 year) and the model had not been used in similar case before it is obvious that choose of some parameters might have been somewhat improper for the use in this study. By fine tuning the model better results could be probably achieved. However, since the focus in this study was to examine the differences arising from different forcings and mixing scenarios, the fact that model parameters were similar in each case is considered to be far more important than the quantitative agreement between observations and model results. Especially since qualitatively the model results agree with the observations. In addition the exclusion of surface waves must effect the mixing near the surface. The wave induced mixing would probably deepen the surface layer during summer which could have an effect on the start of convection. This effect is however considered to be small as the convection appears to be so extensively controlled by the atmospheric heat loss.

Chapter 4

Conclusions

The purpose of this study was to model the ocean state in the Greenland Sea during winter 2010-2011 with 1-D turbulence model GOTM and to compare the results with Argo float observations. Three floats and three different mixing parameterizations together with two different forcing data sets, ERA-Interim and NCEP/NCAR reanalyzes, were used in the model runs. Furthermore, the Lagrangian (atmospheric forcing picked up along the float's path) and Eulerian (atmospheric forcing picked up from float's median location) approaches were tested and compared.

The convection during the winter 2010-2011 was found to happen by gradual mixed layer deepening rather than abrupt plume convection. Convection caused salinity decrease in the Recirculating Atlantic Water (RAW) layer just below the surface while in the deeper layers increase in salinity and density was clearly visible. The temperature decreased throughout the water column, except the deepest layer below the previous convection depth, where the temperatures rose in general. The convection homogenized the water column, which could favor convection in coming years with suitable forcing.

In all cases GOTM was able to produce qualitatively relatively good results. The differences caused by the two data sets were, however, clear. Both forcing data sets produced too low temperatures, results with NCEP/NCAR forcing being somewhat colder than the results with ERA-Interim forcing. The salinities were in general much better captured than the temperatures and again NCEP/NCAR forcing lead to too large salinity increase. ERA-Interim forcing tended to produce a bit too small salinity

increase.

The main results can be summarized to the following points

- Convection in the Greenland Sea during winter 2010-2011 qualifies as a mixed layer deepening type convection (as defined in Ronski and Budeus (2005))
- The convection homogenized the water column, which can be expected to favor deep reaching convection in coming winters given the suitable forcing
- Observed salinity increase below 1000 db was mainly due to RAW influence at 100–600 db layer, but also the atmospheric freshwater flux had a clear effect on the end result
- The differences between ERA-Interim and NCEP/NCAR forcings introduced the greatest differences in the model results
- The differences in temperature and salinity evolution arising from Eulerian and Lagrangian approaches are significant, but the results were ambiguous as neither of them was systematically closer to the observations.
- The mixing parameterizations produce differences in timing of convection

The most striking result was the strong role of the atmospheric freshwater flux in NCEP/NCAR forcing, which was able to compensate the absence of RAW layer in the case of float 6900811. This indicates that the NCEP/NCAR reanalysis data clearly needs a correction as was suggested by Renfrew et al. (2002). In general this study supports the conclusion from the previous studies which is that most of the observed increase in salinity can be explained by the RAW layer. However, the results of this study indicate that also atmospheric freshwater forcing can lead to clearly identifiable salinity increase.

The fact that Eulerian and Lagrangian approaches produce clearly different results implies that the mesoscale atmospheric variability affects the convection. The coarse resolution of the reanalyzes, however, leads to somewhat ambiguous results as neither of the approaches produces results which would be systematically closer to the observations. Comparing the Lagrangian and Eulerian approach using mesoscale atmospheric forcing could provide clearer results.

The importance of water mass transformations in the Greenland Sea for meridional overturning circulation have been speculated over the years. Numbers of studies have noted that most of the water mass transformations take place in the other parts of the Arctic Mediterranean, before the waters enter the Greenland Sea (Mauritzen, 1996; Segtnan et al., 2011). Furthermore evidence of deep reaching convection has not been found since 1970's. However, intermediate convection (to the depth of 2 km), which has been observed (e.g this study and Budeus and Ronski (2009)), produces waters dense enough to feed the overflows over the Greenland-Scotland ridge. Recently there has been studies suggesting heat and salt flux across Arctic front to the Greenland Sea (Segtnan et al., 2011). The results of this study also indicate that additional heat and salt flux is indeed needed to produce the observed profiles, but on the other hand the observations suggest that the RAW layer is the source for the additional fluxes. Most of the floats spent the whole winter close to the western part of the Greenland Sea which means that the results do not reflect the conditions close to the Arctic front. So the speculated flux across the front might exist, but results of this study cannot confirm such transports.

This study has shown that the even the standard Argo float observations are useful in monitoring such a phenomenon as convection. However, it could be feasible to use more advanced Argo floats which have two-way communication capability in this kind of studies. The two-way communication allows more control over floats as user can program the floats over satellite connection. With this system the floats could be altered to make profiles more frequently (e.g. once per day) and with higher vertical spacing during the active convection period. During summers the floats could then return back to normal 10 day cycle. An important improvement to the floats would be the extension of the profile depth to deeper than 2000 db. This would allow better monitoring of convection depth and possibly also observations of the mesoscale coherent vortices described e.g. by Gascard et al. (2002).

Acknowledgments

The research leading to these results has received funding from the European Union's Seventh Framework Programme (FP7/2007-2013) under grant agreement n°212643" (THOR). I would like to thank professor Bert Rudels not only for the possibility to work with this project but also for guiding me trough my master studies in general and providing opportunities to participate in international cruises. I would also like to thank all the people on board F/S Meteor during the cruise M82-1 and on board F/S Poseidon during the cruise P718-2. These cruises taught me a lot about measurements, data-analysis and scientific work in general. Furthermore, it has been great to work with the people in the 'Marine dynamics and modelling' -group at the Finnish Meteorological Institute and especially I would like to thank Dr. Jari Haapala for reviewing my thesis and Meri Korhonen for the helpful discussions. In addition I want to thank my fellow students for the relaxing discussions during coffee and lunch breaks. Finally I thank my family for constant inspiration and support trough my education.

Bibliography

Akitomo, K., 1999: Open-ocean deep convection due to thermobaricity 1. scaling argument. *Journal of Geophysical Research*, 104(C3):pp. 5225–5234. doi:10.1029/1998JC900058. URL `http://dx.doi.org/10.1029/1998JC900058`

Akitomo, K., 2011: Two types of thermobaric deep convection possible in the greenland sea. *Journal of Geophysical Research*, 116. doi:10.1029/2010JC006635. URL `http://dx.doi.org/10.1029/2010JC006635`

Bitz, C.M., Holland, M.M., Hunke, E.C. and Moritz, R.E., 2005: Maintenance of the sea-ice edge. *Journal of Climate*, 18(15):pp. 2903–2921. doi:10.1175/JCLI3428.1. URL `http://dx.doi.org/10.1175/JCLI3428.1`

Blindheim, J. and Østerhus, S., 2005: *The Nordic Seas, main oceanographic features, in The Nordic Seas: An Integrated Perspective*, volume 158 of *Geophys. Monogr. Ser.* AGU, Washington D. C.

Budeus, G., Cisewski, B., Ronski, S., Dietrich, D. and Weitere, M., 2004: Structure and effects of a long lived vortex in the greenland sea. *Geophysical Research Letters*, 31. doi:10.1029/2003GL017983. URL `http://dx.doi.org/10.1029/2003GL017983`

Budeus, G. and Ronski, S., 2009: An integral view of the hydrographic development in the greenland sea over a decade. *The Open Oceanography Journal*, 3:pp. 8–39. ISSN 1874-2521. doi:10.2174/1874252100903010008. URL `http://dx.doi.org/10.2174/1874252100903010008`

Burchard, H., 2002: *Applied Turbulence Modelling in Marine Waters*, volume 100 of *Lecture Notes in Earth Sciences*. Springer Berlin

Campin, J.M., Hill, C., Jones, H. and Marshall, J., 2011: Super-parameterization in ocean modeling: Application to deep convection. *Ocean Modelling*, 36:pp. 90–101. doi:0.1016/j.ocemod.2010.10.003. URL `http://dx.doi.org/0.1016/j.ocemod.2010.10.003`

Clarke, R.A., Swift, J.H., Reid, J.L. and Koltermann, K.P., 1990: The formation of greenland sea deep water: double diffusion or deep convection? *Deep Sea Research Part A. Oceanographic Research Papers*, 37(9):pp. 1385 – 1424. ISSN 0198-0149. doi:10.1016/0198-0149(90)90135-I. URL `http://dx.doi.org/10.1016/0198-0149(90)90135-I`

Dee, D.P., Uppala, S.M., Simmons, A.J., Berrisford, P., Poli, P., Kobayashi, S., Andrae, U., Balmaseda, M.A., Balsamo, G., Bauer, P., Bechtold, P., Beljaars, A.C.M., van de Berg, L., Bidlot, J., Bormann, N., Delsol, C., Dragani, R., Fuentes, M., Geer, A.J., Haimberger, L., Healy, S.B., Hersbach, H., Hï¿½lm, E.V., Isaksen, L., Kï¿½llberg, P., Kï¿½hler, M., Matricardi, M., McNally, A.P., Monge-Sanz, B.M., Morcrette, J.J., Park, B.K., Peubey, C., de Rosnay, P., Tavolato, C., Thï¿½paut, J.N. and Vitart, F., 2011: The era-interim reanalysis: configuration and performance of the data assimilation system. *Quarterly Journal of the Royal Meteorological Society*, 137(656):pp. 553–597. ISSN 1477-870X. doi:10.1002/qj.828. URL `http://dx.doi.org/10.1002/qj.828`

Eldevik, T., Nilsen, J.E., Iovino, D., Olsson, K.A., Sandø, A.B. and Drange, H., 2009: Observed sources and variability of nordic seas overflow. *Nature Geoscience*, 2:pp. 406–410. doi:10.1038/NGEO518. URL `http://dx.doi.org/10.1038/NGEO518`

Ferrari, R. and Ferreira, D., 2011: What processes drive the ocean heat transport? *Ocean Modelling*, 38:pp. 171–186. doi:10.1016/j.ocemod.2011.02.013. URL `http://dx.doi.org/10.1016/j.ocemod.2011.02.013`

Ferreira, D., Marshall, J. and Rose, B., 2010: Climate determinism revisited: Multiple equilibria in a complex climate model. *Journal of Climate*, 24:pp. 992–1012. ISSN 0894–8755. doi:10.1175/2010JCLI3580.1. URL `http://dx.doi.org/10.1175/2010JCLI3580.1`

Gascard, J.C., Watson, A.J., Messias, M.J., Olsson, K.A., Johannessen, T. and Simonsen, K., 2002: Long-lived vortices as a mode of deep ventilation in the greenland sea. *Nature*, 416:pp. 525–527. doi:10.1038/416525a. URL `http://dx.doi.org/10.1038/416525a`

Hansen, B. and Østerhus, S., 2000: North altantic – nordic seas exchanges. *Progress In Oceanography*, 45(2):pp. 109–208. doi:10.1016/S0079-6611(99)00052-X. URL `http://dx.doi.org/10.1016/S0079-6611(99)00052-X`

Harcourt, R.R., 2005: Thermobaric cabbeling over maud rise: Theory and large eddy simulation. *Progress in Oceanography*, 67:pp. 186–244. doi:10.1016/j.pocean.2004.12.001. URL `http://dx.doi.org/10.1016/j.pocean.2004.12.001`

Hoffman, P.F., Kaufman, A.J., Halverson, G.P. and Schrag, D.P., 1998: A neoproterozoic snowball earth. *Science*, 281(5381):pp. 1342–1346. doi:10.1126/science.281.5381.1342. URL `http://dx.doi.org/10.1126/science.281.5381.1342`

IAPWS, 2008: *Release on the IAPWS Formulation 2008 for the Thermodynamic Properties of Seawater*. The International Association for the Properties of Water and Steam, Berlin, Germany, September 2008. URL `http://teos-10.org/pubs/IAPWS-08.pdf`

IOC, SCOR and IAPSO, 2010: *The international thermodynamic equation of seawater ï¿½ 2010: Calculation and use of thermodynamic properties*. Number 56 in Intergovernmental Oceanographic Commission, Manuals and Guides. UNESCO (English). URL `http://teos-10.org/pubs/TEOS-10_Manual.pdf`

Jackett, D.R., McDougall, T.J., Feistel, R., Wright, D.G. and Griffies, S.M., 2006: Algorithms for density, potential temperature, conservative temperature, and the freezing temperature of seawater. *Journal of Physical Oceanography*, 23:pp. 1709–1728. doi:10.1175/JTECH1946.1. URL `http://dx.doi.org/10.1175/JTECH1946.1`

Jakobsen, P.K., Ribergaard, M.H., Quadfasel, D., T., S. and Hughes, C.W., 2011: Near-surface circulation in the northern north atlantic as inferred from lagrangian drifters: Variability from the mesoscale to interannual. *Journal of Geophysical Research*, 108(C8). doi:10.1029/2002JC001554. URL `http://dx.doi.org/10.1029/2002JC001554`

Jeansson, E., Jutterstrom, S., Rudels, B., Anderson, L., Olsson, K., Jonesd, E.P., Jr., W.M.S. and Swift, J.H., 2008: Sources to the east greenland current and its contribution to the denmark strait overflow. *Progress In Oceanography*, 78:pp. 12–18. doi:10.1016/j.pocean.2007.08.031. URL `http://dx.doi.org/10.1016/j.pocean.2007.08.031`

Jerlov, N.G., 1968: *Optical Oceanography*. Elsevier Publishing Company, Amsterdam

Kalnay, E., Kanamitsu, M., Kistler, R., Collins, W., Deaven, D., Gandin, L., Iredell, M., Saha, S., White, G., Woollen, J., Zhu, Y., Leetmaa, A., Reynolds, R., Chelliah, M., Ebisuzaki, W., Higgins, W., Janowiak, J., Mo, K.C., Ropelewski, C., Wang, J., Jenne, R. and Joseph, D., 1996: The ncep/ncar 40-year reanalysis project. *Bulletin of the American Meteorological Society*, 77:pp. 437–471. ISSN 0003-0007. doi:10.1175/1520-0477(1996)077<0437:TNYRP>2.0.CO;2. URL `http://dx.doi.org/10.1175/1520-0477(1996)077<0437:TNYRP>2.0.CO;2`

Karstensen, J., Schlosser, P., Wallace, D.W.R., Bullister, J.L. and Blindheim, J., 2005: Water mass transformation in the greenland seaduring the 1990s. *Journal of Geophysical Research*, 110. doi: 10.1029/2004JC002510. URL http://dx.doi.org/10.1029/2004JC002510

Kasajima, Y. and Johannessen, T., 2009: Role of cabbeling in water densification in the greenland basin. *Ocean Science*, 5(3):pp. 247–257. doi:10.5194/os-5-247-2009. URL http://dx.doi.org/10.5194/os-5-247-2009

Large, W., McWilliams, J. and Doney, S., 1994: Oceanic vertical mixing: a review and a model with a nonlocal boundary layer parameterization. *Reviews of Geophysics*, 32(4):pp. 363–403. doi:10.1029/94RG01872. URL http://dx.doi.org/10.1029/94RG01872

Latarius, K. and Quadfasel, D., 2010: Seasonal to inter-annual variability of temperature and salinity in the greenland sea gyre: heat and freshwater budgets. *Tellus A*, 62(4):pp. 497–515. ISSN 1600-0870. doi:10.1111/j.1600-0870.2010.00453.x. URL http://dx.doi.org/10.1111/j.1600-0870.2010.00453.x

Lenton, T.M., Held, H., Kriegler, E., Hall, J.W., Lucht, W., Rahmstorf, S. and Schellnhuber, H.J., 2008: Tipping elements in the earth's climate system. *Proceedings of the National Academy of Sciences*, 105(6):pp. 1786–1793. doi:10.1073/pnas.0705414105. URL http://dx.doi.org/10.1073/pnas.0705414105

Losch, M., Herlufsen, S. and Timmermann, R., 2006: Effects of heterogeneous surface boundary conditions on parameterized oceanic deep convection. *Ocean Modelling*, 13(2):pp. 156 – 165. ISSN 1463-5003. doi:10.1016/j.ocemod.2005.12.003. URL http://dx.doi.org/10.1016/j.ocemod.2005.12.003

Marshall, J. and Schott, F., 1999: Open-ocean convection: Observations, theory, and models. *Reviews of Geophysics*, 37(1). doi:10.1029/98RG02739. URL http://dx.doi.org/10.1029/98RG02739

Mauritzen, C., 1996: Production of dense overflow waters feeding the north atlantic across the greenland-scotland ridge. part 1: Evidence for a revised circulation scheme. *Deep Sea Research Part I: Oceanographic Research Papers*, 43(6):pp. 769–806. ISSN 0967–0637. doi: 10.1016/0967-0637(96)00037-4. URL http://www.sciencedirect.com/science/article/pii/0967063796000374

Naveira Garabato, A.C., Oliver, K.I.C., Watson, A.J. and Messias, M.J., 2004: Turbulent diapycnal mixing in the nordic seas. *Journal of Geophysical Research*, 109(C12010). doi: 10.1029/2004JC002411. URL http://dx.doi.org/10.1029/2004JC002411

O'Brien, J., 1970: A note on the vertical structure of the eddy exchange coefficient in the planetary boundary layer. *Journal of Atmospheric Sciences*, 27(8):pp. 1213 – 1215. doi: 10.1175/1520-0469(1970)027<1213:ANOTVS>2.0.CO;2. URL http://dx.doi.org/10.1175/1520-0469(1970)027<1213:ANOTVS>2.0.CO;2

Renfrew, I.A., Moore, G.W.K., Guest, P.S. and Bumke, K., 2002: A comparison of surface layer and surface turbulent flux observations over the labrador sea with ecmwf analyses and ncep reanalyses. *Journal of Physical Oceanography*, 32:pp. 383–400. doi:10.1175/1520-0485(2002)032<0383:ACOSLA>2.0.CO;2. URL http://dx.doi.org/10.1175/1520-0485(2002)032<0383:ACOSLA>2.0.CO;2

Ronski, S. and Budeus, G., 2005: How to identify winter convection in the greenland sea from hydrographic summer data. *Journal of Geophysical Research*, 110. doi:10.1029/2003JC002156. URL http://dx.doi.org/10.1029/2003JC002156

Ronski, S. and Budeus, G., 2006: Vertical structure reveals eddy lifetime in the greenland sea. *Geophysical Research Letters*, 33. doi:10.1029/2006GL026045. URL http://dx.doi.org/10.1029/2006GL026045

Rose, B.E.J. and Marshall, J., 2009: Ocean heat transport, sea ice, and multiple cilmate states: Insight from energy balance models. *Journal of Atmospheric Sciences*, 65:pp. 2828–2843. doi: 10.1175/2009JAS3039.1. URL http://dx.doi.org/10.1175/2009JAS3039.1

Rudels, B., Fahrbach, E., Meincke, J., Budèus, G. and Eriksson, P., 2002: The east greenland current and its contribution to the denmark strait overflow. *ICES Journal of Marine Science*, 59(15):pp. 1133–1154. doi:10.1006/jmsc.2002.1284. URL http://dx.doi.org/10.1006/jmsc.2002.1284

Sea–Bird Electronics, Inc., 2011: The argo ctd – sbe 41/41cp ctd module for autonomous profiling floats. http://www.seabird.com/alace.htm

Segtnan, O.H., Furevik, T. and Jenkins, A.D., 2011: Heat and freshwater budgets of the nordic seas computed. *Journal of Geophysical Research*, 116. doi:10.1029/2011JC006939. URL http://dx.doi.org/10.1029/2011JC006939

Shapiro, S.S. and Wilk, M.B., 1965: An analysis of variance test for normality (complete samples). *Biometrika*, 52(3/4):pp. pp. 591–611. ISSN 00063444. URL http://www.jstor.org/stable/2333709

Shchepetkin, A.F. and McWilliams, J.C., 2011: Accurate boussinesq oceanic modeling with a practical, stiffened equation of state. *Ocean Modelling*, 38(1–2):pp. 41–70. ISSN 1463–5003. doi: 10.1016/j.ocemod.2011.01.010. URL http://dx.doi.org/10.1016/j.ocemod.2011.01.010

Stull, R.B., 1993: Review of non-local mixing in turbulent atmospheres: Transilient turbulence theory. *Boundary-Layer Meteorology*, 62:pp. 21–96. ISSN 0006-8314. doi:10.1007/BF00705546. URL http://dx.doi.org/10.1007/BF00705546

Taylor, K., 2001: Summarizing multiple aspects of model performance in a single diagram. *Journal of Geophysical Research*, 106(D7):pp. 7183–7192. doi:10.1029/2000JD900719. URL http://dx.doi.org/10.1029/2000JD900719

Umlauf, L., 2011: *Turbulence parameterisation in hydrobiological models for natural waters*. Ph.D. thesis, TU Darmstadt,Germany. URL http://tuprints.ulb.tu-darmstadt.de/177/

Umlauf, L., Burchard, H. and Bolding, K., cited july 2011: *GOTM Sourcecode and test case documentation, version 4.0*. URL http://www.gotm.net/pages/documentation/manual/pdf/a4.pdf

Våge, K., Pickart, R.S., Spall, M.A., Valdimarsson, H., Jonsson, S., Torres, D.J., Østerhus, S. and Eldevik, T., 2011: Significant role of the north icelandic jet in the formation of denmark strait overflow water. *Nature Geoscience*, 4(10):pp. 723–727. doi:10.1038/ngeo1234. URL http://dx.doi.org/10.1038/ngeo1234

Visbeck, M., Fischer, J. and Schott, F., 1995: Preconditioning the greenland sea for deep convection: Ice formation and ice drift. *Journal of Geophysical Research*, 100(C9):pp. 18 489–18 502. doi: 10.1029/95JC01611. URL http://dx.doi.org/10.1029/95JC01611

Visbeck, M. and Rhein, M., 2000: Is bottom boundary layer mixing slowly ventilating greenland sea deep water*. *Journal of Physical Oceanography*, 30(1):pp. 215–224. doi: 10.1175/1520-0485(2000)030<0215:IBBLMS>2.0.CO;2. URL http://dx.doi.org/10.1175/1520-0485(2000)030<0215:IBBLMS>2.0.CO;2

Voet, G., Quadfasel, D., mork, K.A. and Søiland, H., 2010: The mid-depth circulation of the nordic seas derived from profiling float observations. *Tellus A*, 62(4):pp. 516–529. ISSN 1600-0870. doi:10.1111/j.1600-0870.2010.00444.x. URL http://dx.doi.org/10.1111/j.1600-0870.2010.00444.x

Zachos, J., Pagani, M., Sloan, L., Thomas, E. and Billups, K., 2001: Trends, rhythms, and aberrations in global climate 65 ma to present. *Science*, 292(5517):pp. 686–693. doi:10.1126/science.1059412. URL http://dx.doi.org/10.1126/science.1059412

Appendices

Appendix A

Equation of state

At the moment Jackett et al. (2006) density equation based on potential temperature, salinity and pressure ($\rho(\theta, S, p)$) is implemented in GOTM along with the traditional UNESCO equation of state from 1980. However, in 2010 the new international thermodynamic equation of seawater - 2010 (TEOS-10) was introduced and adopted by the Intergovernmental Oceanographic Commission (IOC), International Association for the Physical Sciences of the Oceans (IAPSO) and the Scientific Committee on Oceanic Research (SCOR). This new thermodynamical equation of state uses Conservative Temperature (CT) and Absolute Salinity (S_A) instead of the traditional variables potential temperature and salinity (expressed in practical salinity units). Jackett et al. (2006) discussed the errors which arise from the use of the old variables in the ocean models. When the modelling is done in relatively small area(e.g. Greenland Sea as in this study) and in salinities near 35 g kg^{-1} the use of practical salinity and potential temperature as model variables induce only small errors (Jackett et al., 2006). Since the new TEOS-10 algorithm was not available in GOTM, the equation of state from Jackett et al. (2006) was used in this study, which, however, is more accurate than the UNESCO equation of state from 1980 (Jackett et al., 2006). However, to get the most accurate initial potential temperature profiles they were calculated with TEOS-10 Gibss Seawater (GSW) Matlab toolbox (using funtion gsw_pt0_from_t). In general the results were analyzed using the traditional UNESCO units. TEOS-10 equations were, however, used when calculations included an assumption about salinity conservations (see section 3.1). The usage of TEOS-10 algorithms trough the thesis, both in model and in analysis of observations would have been more consistent approach, but as stated above the fact that model was limited to the old variables is considered to introduce only negligible errors.

Appendix B

Additional Figures

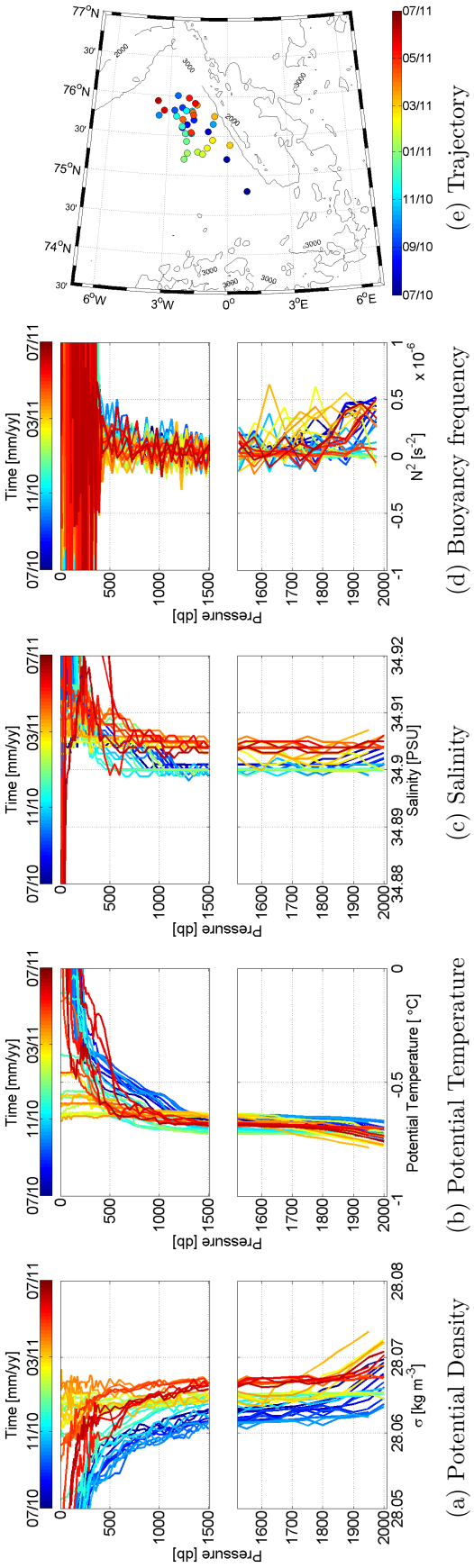

(a) Potential Density (b) Potential Temperature (c) Salinity (d) Buoyancy frequency (e) Trajectory

Figure B.1: Different profiles measured by float 6900802 between July 2010–July 2011. The upper panel shows the properties between 0–1500 db while the lower panel is zoomed in the depths between 1500–2000 db. Figure B.1e shows the floats surface positions.

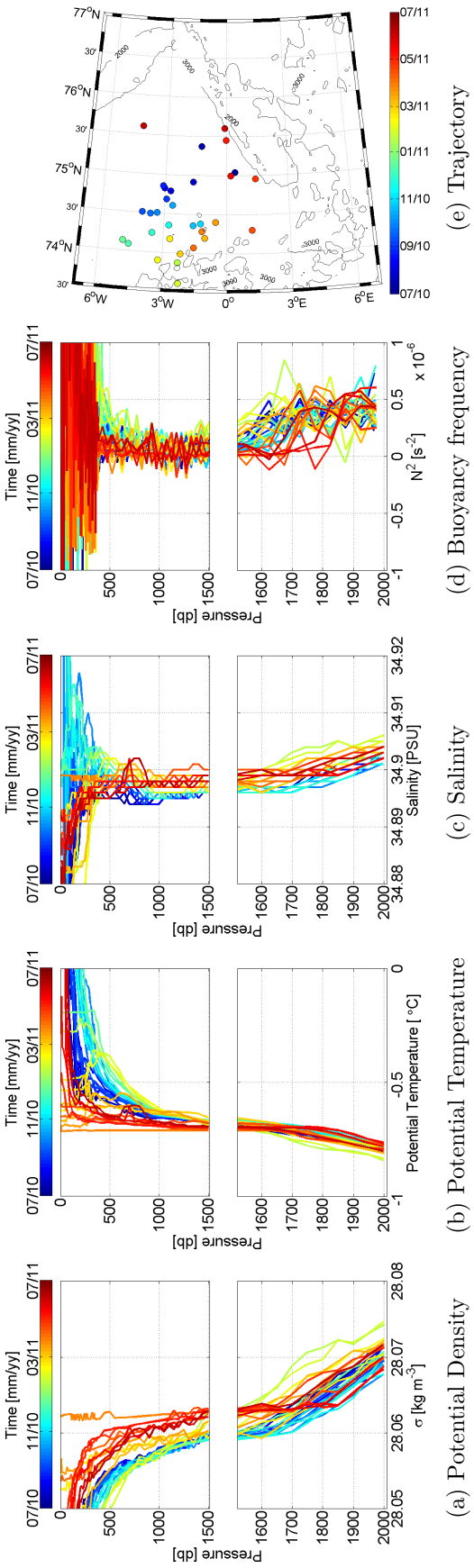

(a) Potential Density (b) Potential Temperature (c) Salinity (d) Buoyancy frequency (e) Trajectory

Figure B.2: Different profiles measured by float 6900811 between July 2010–July 2011. The upper panel shows the properties between 0–1500 db while the lower panel is zoomed in the depths between 1500–2000 db. Figure B.2e shows the floats surface positions.

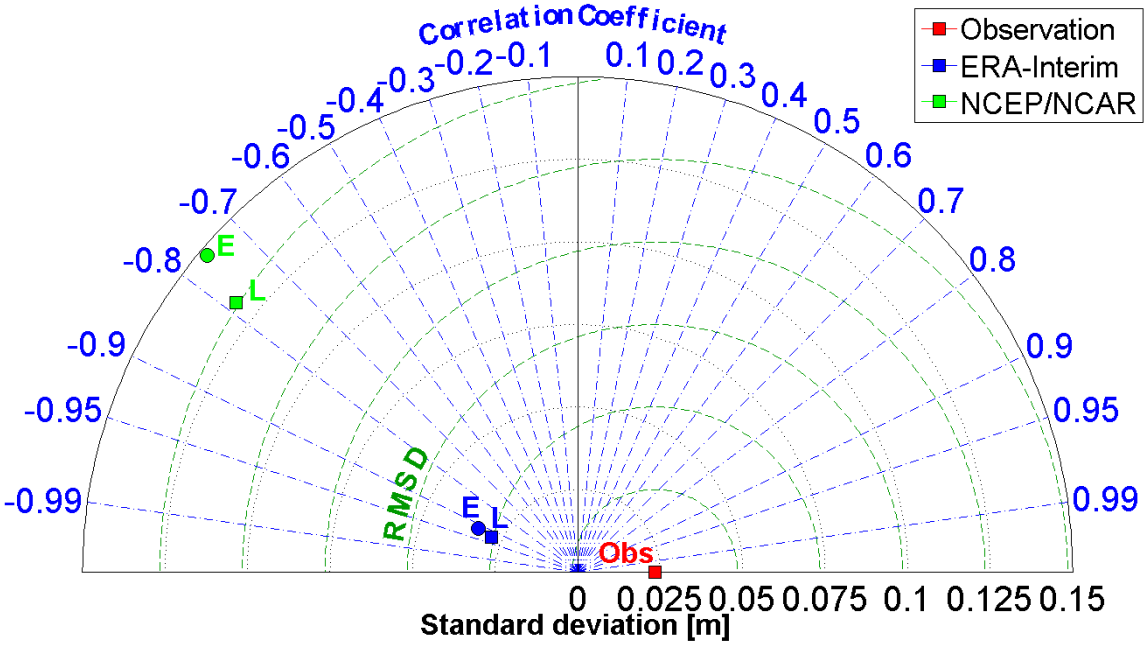

(a) 6900802

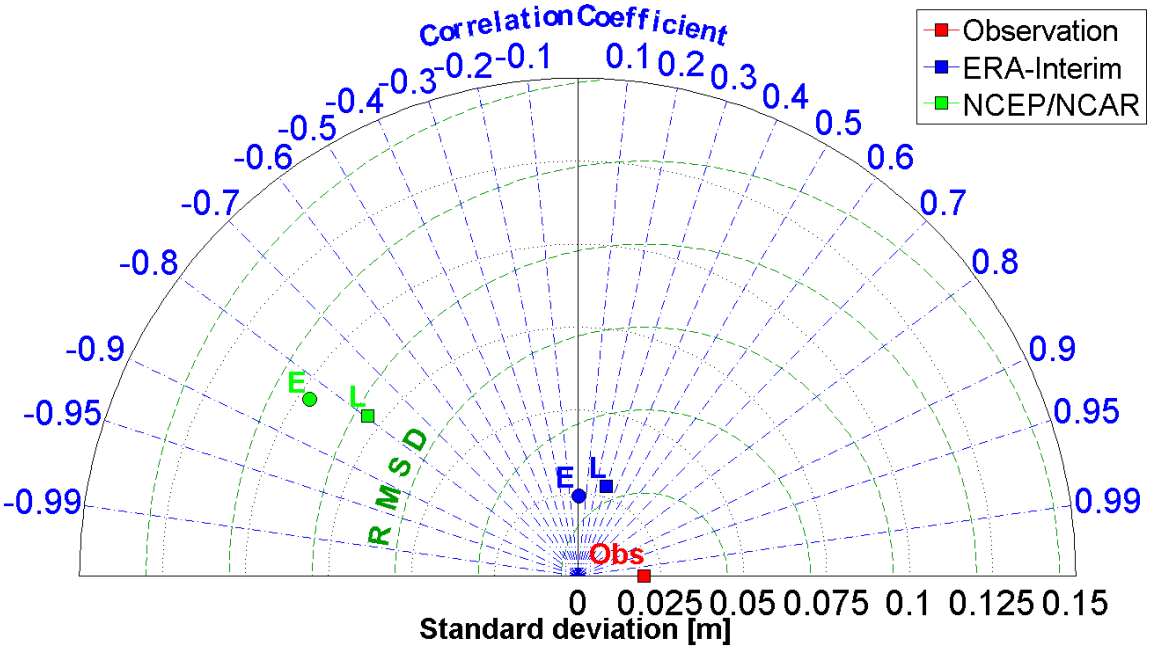

(b) 6900811

Figure B.3: Taylor diagrams for cumulative atmospheric freshwater flux (precipitation-evaporation) for the floats 6900802 and 6900811 using both Lagrangian (L) and Eulerian (E) approach for the period between July 2010–June 2011. Observations refers to changes in the freshwater content derived from the float data. Colors refer to the forcing data set, red is NCEP/NCAR and magenta is ERA-Interim reanalysis. Symbols refer to the approach, rectangular is for Lagrangian and circle is for Eulerian approach.

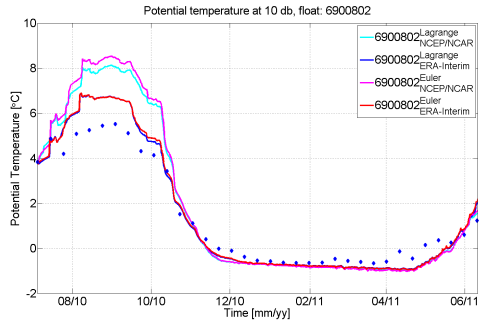

(a) Potential temperature at 10 db

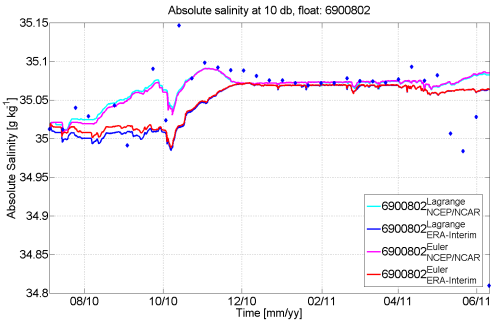

(b) Absolute Salinity at 10 db

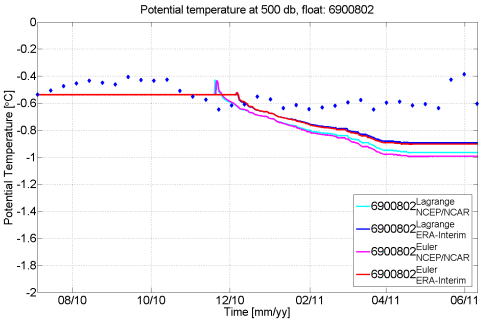

(c) Potential temperature at 500 db

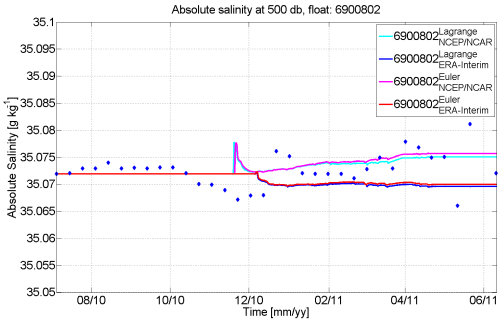

(d) Absolute Salinity at 500 db

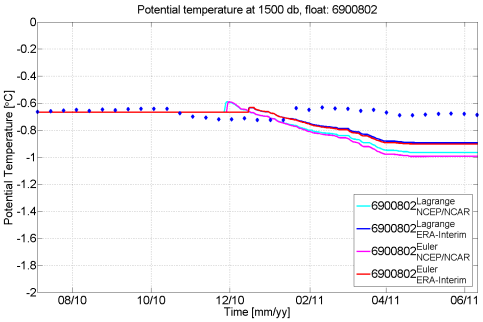

(e) Potential temperature at 1500 db

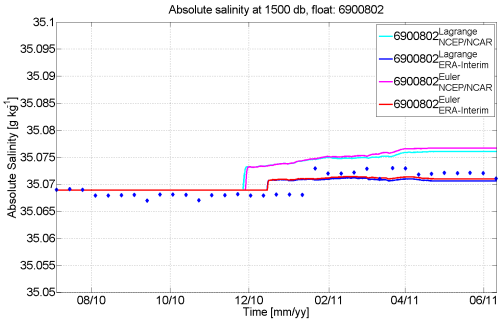

(f) Absolute Salinity at 1500 db

Figure B.4: Potential temperature and Absolute Salinity timeseries at different pressure levels for float 6900802.

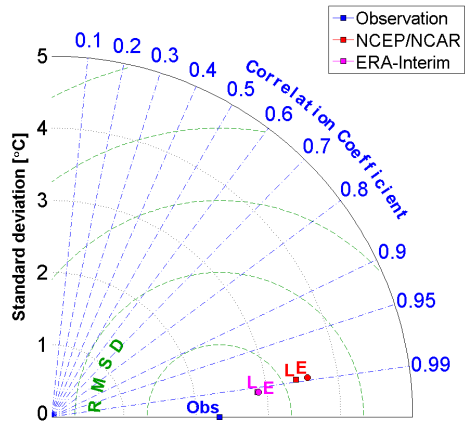

(a) Potential temperature at 10 db

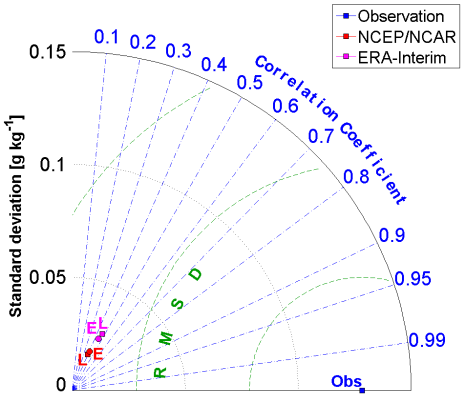

(b) Absolute Salinity at 10 db

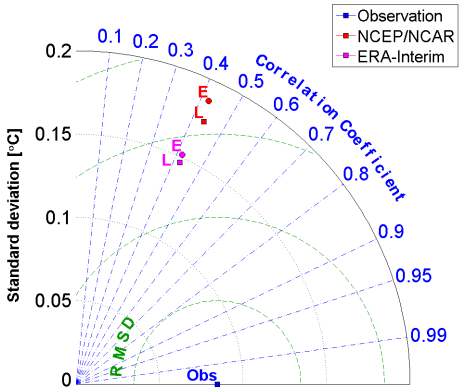

(c) Potential temperature at 500 db

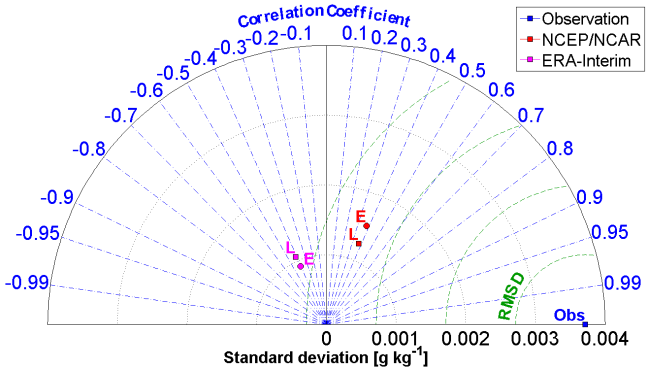

(d) Absolute Salinity at 500 db

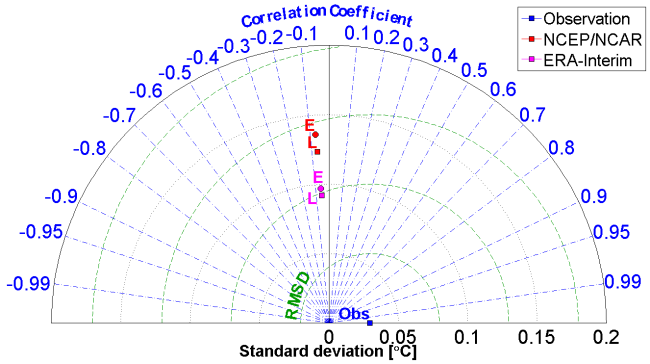

(e) Potential temperature at 1500 db

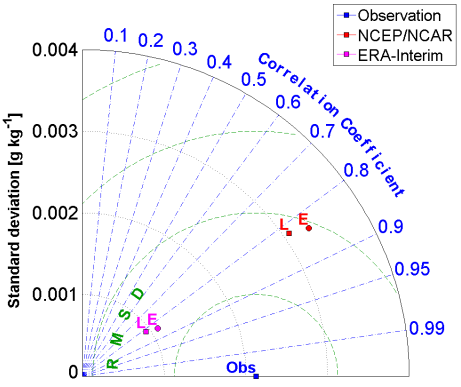

(f) Absolute Salinity at 1500 db

Figure B.5: The Taylor diagrams corresponding to the potential temperature and Absolute Salinity timeseries shown in Figure 3.10 for float 6900802.

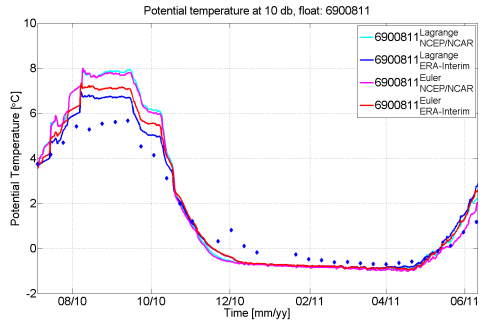

(a) Potential temperature at 10 db

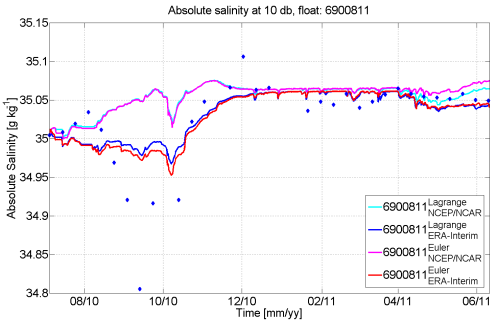

(b) Absolute Salinity at 10 db

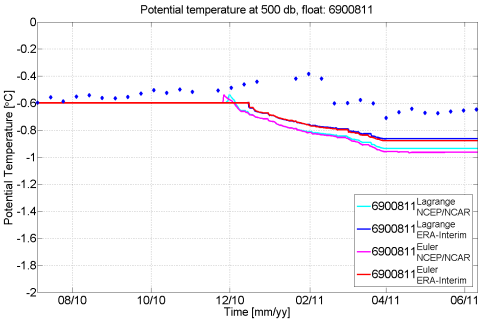

(c) Potential temperature at 500 db

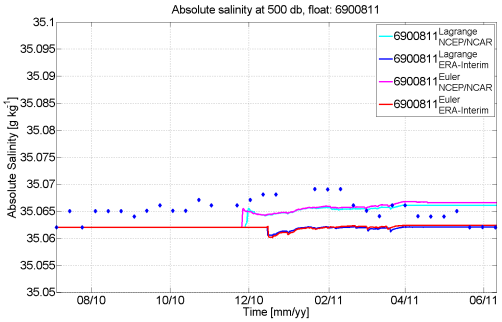

(d) Absolute Salinity at 500 db

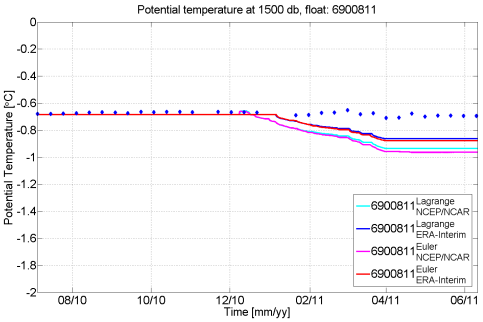

(e) Potential temperature at 1500 db

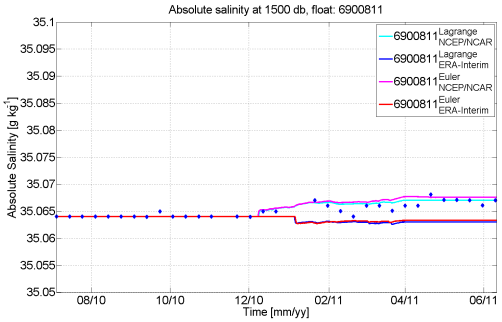

(f) Absolute Salinity at 1500 db

Figure B.6: Potential temperature and Absolute Salinity timeseries at different pressure levels for float 6900811.

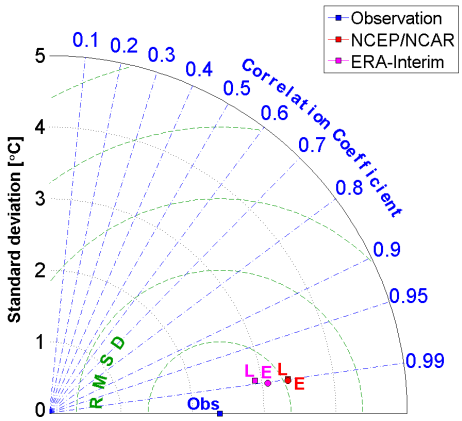

(a) Potential temperature at 10 db

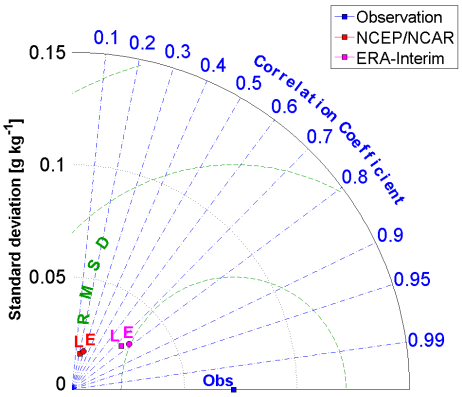

(b) Absolute Salinity at 10 db

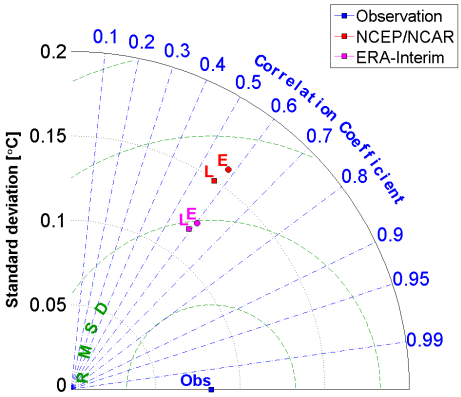

(c) Potential temperature at 500 db

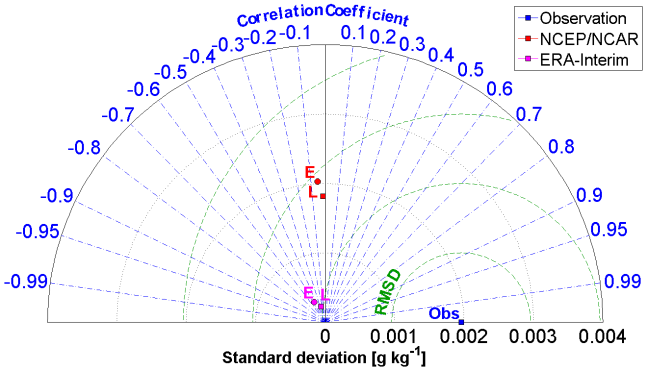

(d) Absolute Salinity at 500 db

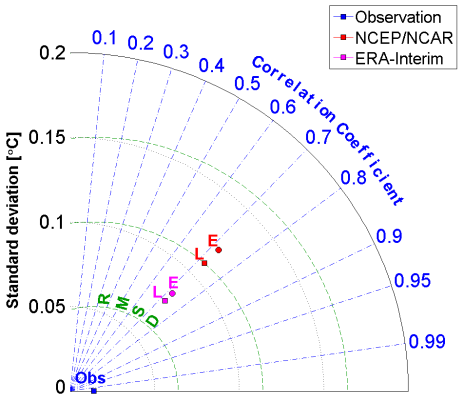

(e) Potential temperature at 1500 db

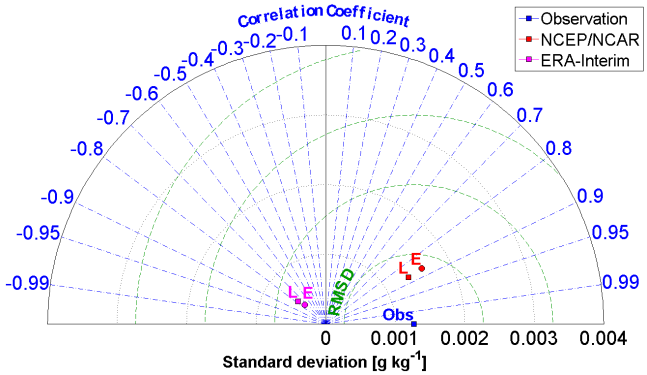

(f) Absolute Salinity at 1500 db

Figure B.7: The Taylor diagrams corresponding to the potential temperature and Absolute Salinity timeseries shown in Figure 3.10 for float 6900811.

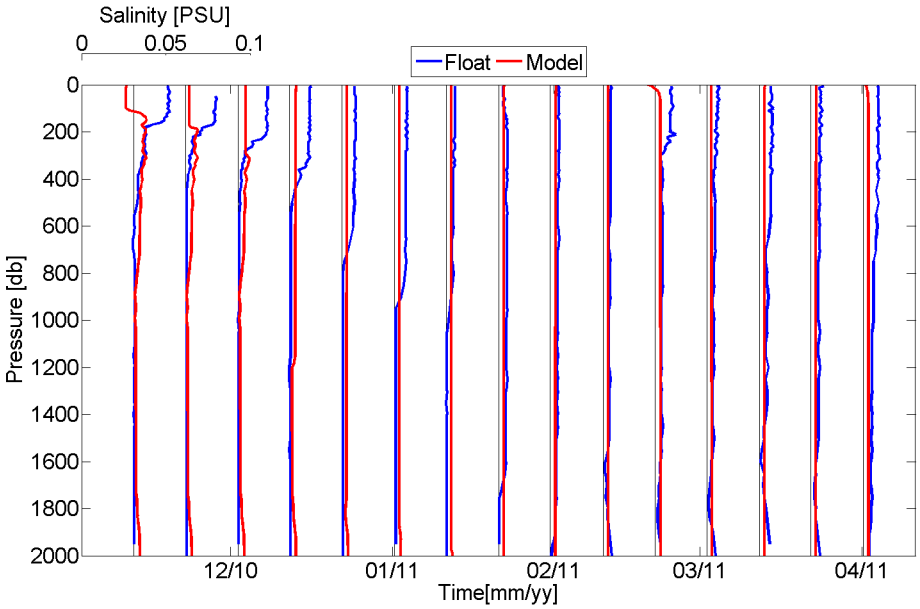

(a) Salinity

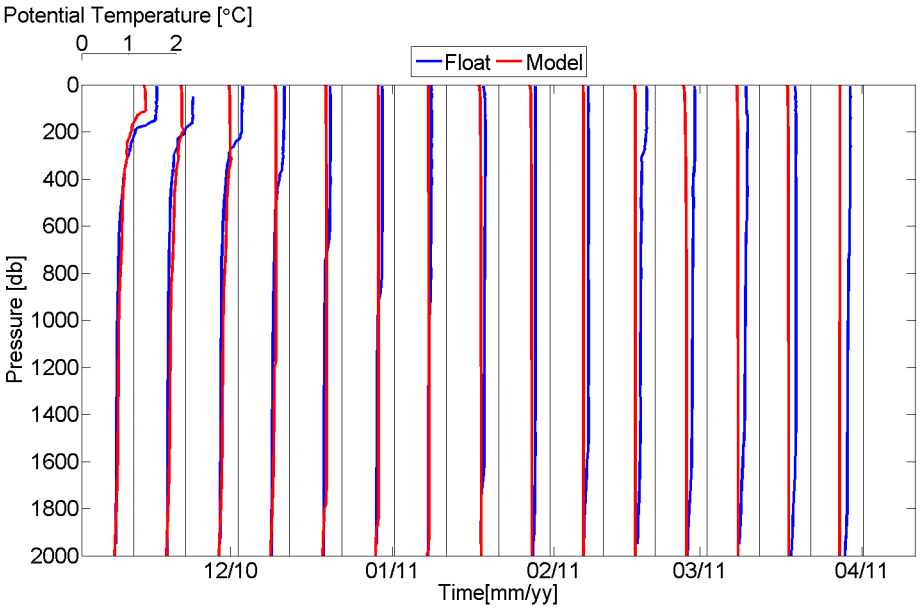

(b) Potential temperature

Figure B.8: Salinity and potential temperature profiles during active convection for float 6900802 with ERA-Interim forcing. Temperature and salinity scales are given in the upper left corner of the plots. The profiles are relative to the mean temperature (-0.230) and mean salinity (34.899) of the initial profile, they are plotted to the figure with black line. It can be seen how the warmer and more saline RAW layer mixes down. First the temperature rise in the waters below, but soon the surface cooling takes over and at the end the water column is cooler than initially. Convection decreases the salinity in the RAW layer and increases it in deeper layers. In the end the salinity of the water column is close to the average of the RAW and surrounding layers.

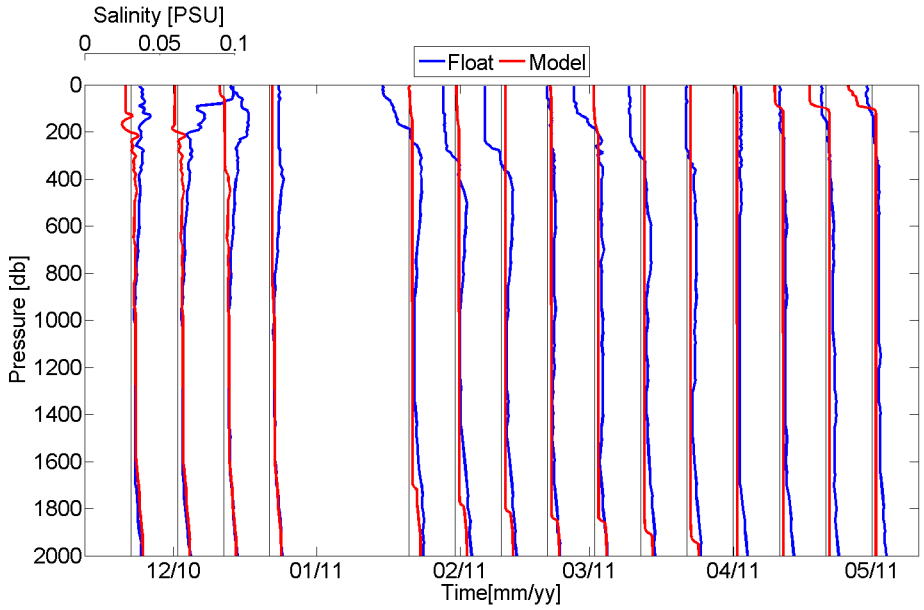

(a) Salinity

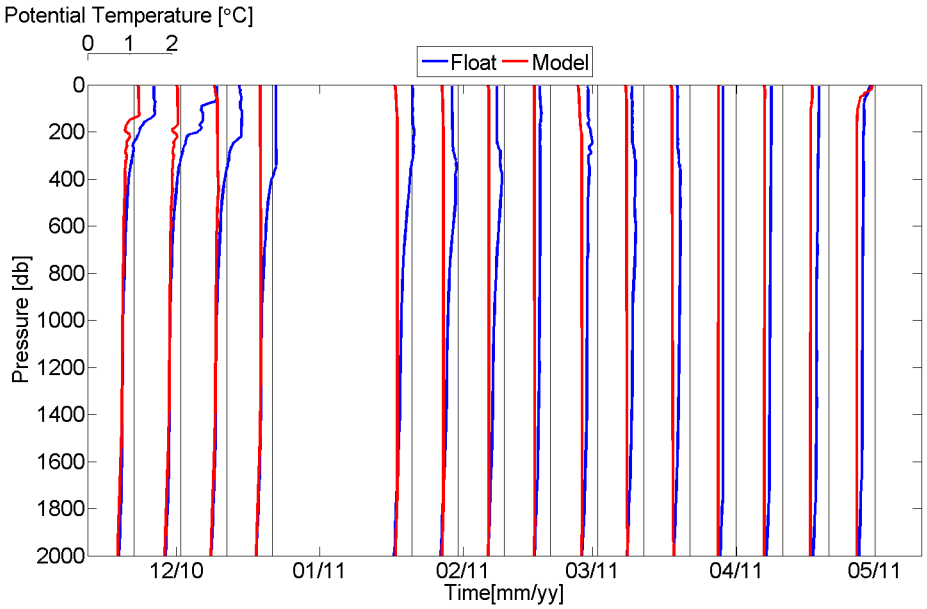

(b) Potential temperature

Figure B.9: Salinity and potential temperature profiles during active convection for float 6900811 with ERA-Interim forcing. Temperature and salinity scales are given in the upper left corner of the plots. The profiles are relative to the mean temperature (-0.295) and mean salinity (34.892) of the initial profile, they are plotted to the figure with black line. In contrary to the two other floats convection there is no RAW layer in the initial profile and consequently the model mixes cold but freshwater down diluting the salinity. The observations, however, show that the RAW layer appears before the convection starts and mixes down similarly to the other profiles.

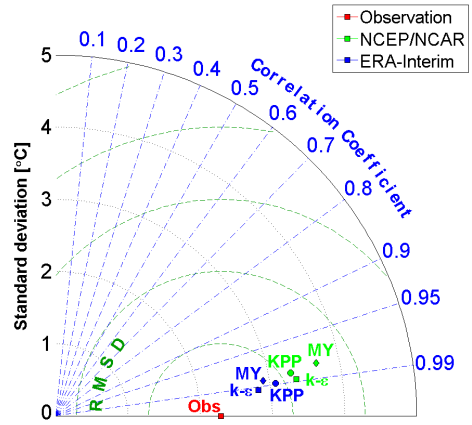

(a) Potential temperature at 10 db

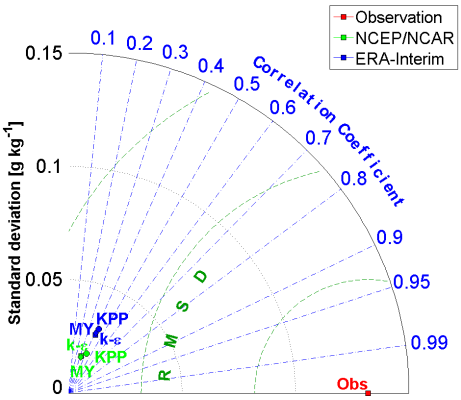

(b) Absolute Salinity at 10 db

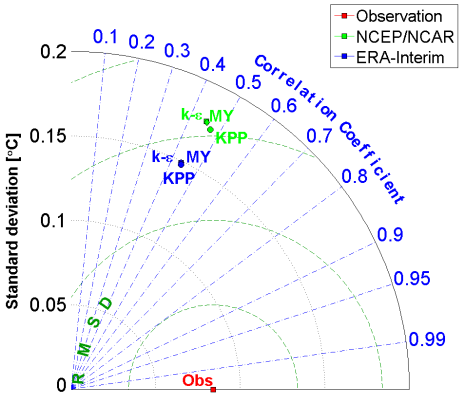

(c) Potential temperature at 500 db

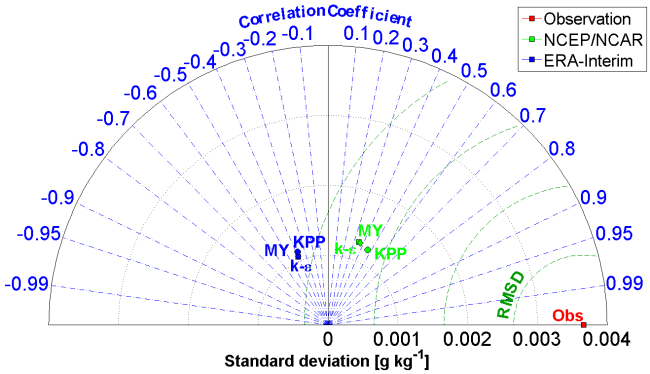

(d) Absolute Salinity at 500 db

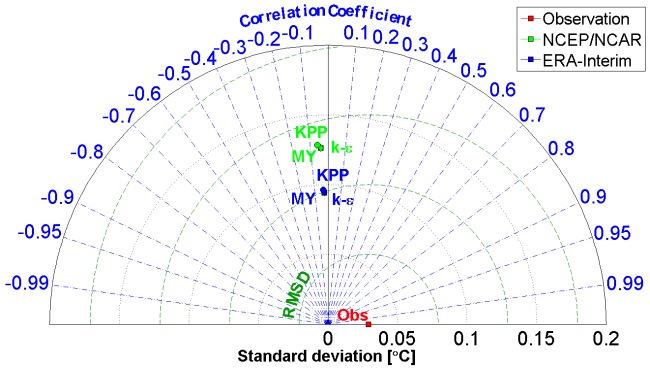

(e) Potential temperature at 1500 db

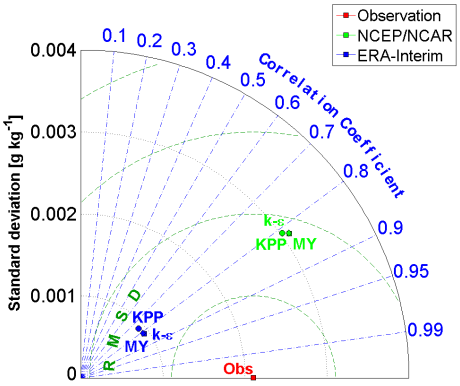

(f) Absolute Salinity at 1500 db

Figure B.10: Taylor diagrams at different depths for potential temperature and salinity, float 6900802.

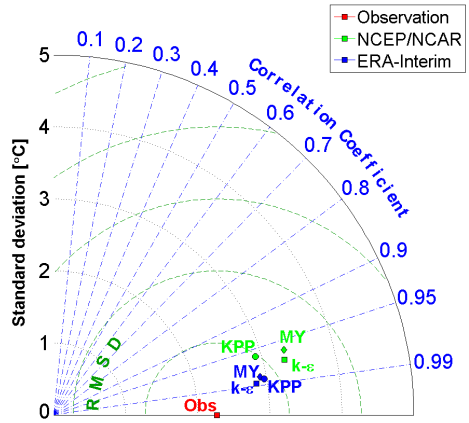

(a) Potential temperature at 10 db

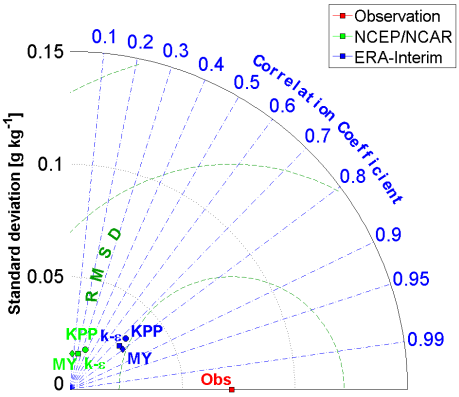

(b) Absolute Salinity at 10 db

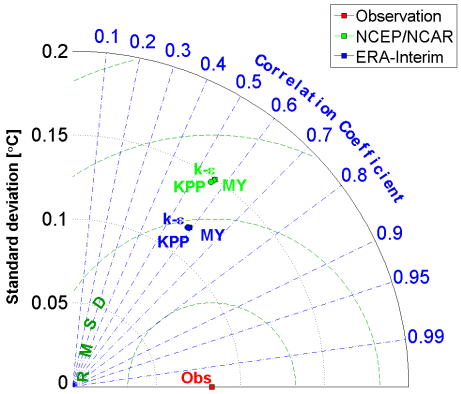

(c) Potential temperature at 500 db

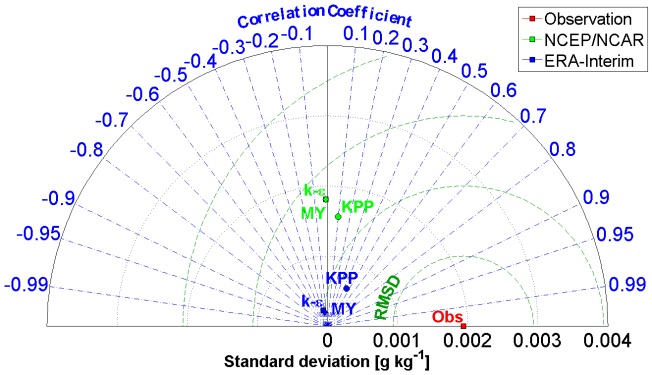

(d) Absolute Salinity at 500 db

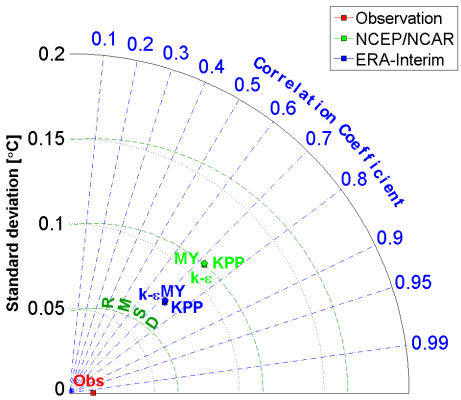

(e) Potential temperature at 1500 db

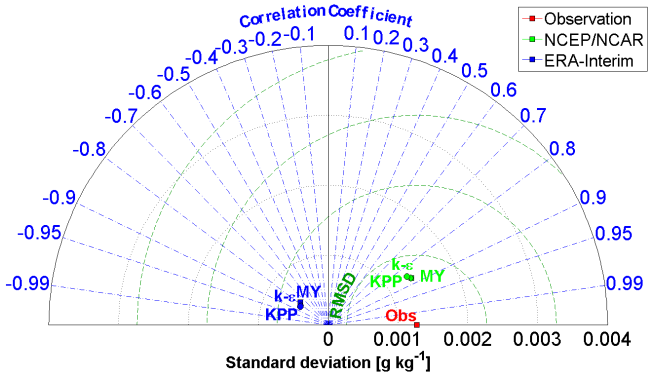

(f) Absolute Salinity at 1500 db

Figure B.11: Taylor diagrams at different depths for potential temperature and salinity, float 6900811.

Appendix C

List of Symbols

Table C.1: List of Symbols

Symbol	Explanation
α_M	Shear number
α_N	Buoyancy number
b	Buoyancy
B	Buoyancy production
B_ϵ	Buoyancy production of dissipation
c_p'	Specific heat capacity
c_μ	Non-dimensional stability function for momentum
c_μ'	Non-dimensional stability function for tracers
c_L	Neutral non-dimesional stability function for momentum
C_f	Bottom friction coefficient
d	Vertical coordinate in mixed layer (KPP parameterization)
ϵ	dissipation rate of turbulent kinetic energy
ϵ_ϵ	Dissipation of dissipation (gradients of ϵ)
F	Freshwater content
$\mathbf{g}$	3-D gravitational acceleration
g	Downward gravitational acceleration
G	Cubic shape function (polynomial)

Table C.1: List of Symbols

Symbol	Explanation
γ	Non-local transport
Γ	Non-local transport ($\Gamma = \nu_t \gamma$)
h	Mixed layer depth (KPP parameterization)
h^0	Potential enthalpy
H	Heat content
I	Local solar radiation
k	Turbulent kinetic energy
L	Macro length scale
M	Shear frequency
N	Brunt-Vaisala frequency
∇	3-Dimensional partial derivative operator
ν	Kinematic viscosity
ν_t	Turbulent kinematic viscosity
ν_t'	Turbulent scalar viscosity
ν^Θ	Molecular diffusivity of heat
ν^S	Molecular diffusivity of salt
$\mathbf{\Omega}$	Earth's 3-D angular velocity
Ω	Earth's angular velocity
ϕ	Latitude
φ	Placeholder for any variable
p	Pressure
P	Shear production
P_ϵ	Shear production of dissipation
q	3-D fluctuation velocity
Q_s	Sensible heat flux
Q_l	Latent heat flux
Q_b	Long wave back radiation
ρ	Density

Table C.1: List of Symbols

Symbol	Explanation
ρ_{fw}	Density of freshwater
S	Salinity
S_A	Absolute Salinity
σ	A non-dimensional vertical coordinate
τ_R	Relaxation time scale
τ_s	Surface wind stress
t	Time
Θ	Potential temperature
Θ_C	Conservative Temperature
u	Eastward velocity component
$\mathbf{v}$	3-D velocity
v	Northward velocity component
w	Upward velocity component
ζ	Sea surface height
z	Vertical coordinate
z_0	Roughness length (at surface)